MOMENTUM IMAGING STUDIES OF ELECTRON AND ION DYNAMICS IN A STRONG LASER FIELD

by

CHAKRA MAN MAHARJAN

M. Sc., Tribhuvan University, Nepal, 1992
B.Sc., Tribhuvan University, Nepal, 1989

AN ABSTRACT OF A DISSERTATION

submitted in partial fulfillment of the requirements for the degree

DOCTOR OF PHILOSOPHY

Department of Physics
College of Arts and Sciences

KANSAS STATE UNIVERSITY
Manhattan, Kansas

2007

Abstract

An underlying goal of studying atomic or molecular dynamics with short laser pulses is to reach a time scale short enough to study the evolution of the system in the time domain. In this thesis, the strong field ionization of atoms and molecules has been investigated with the highly resolved technique known as cold target recoil momentum spectroscopy (COLTRIMS). The thesis can be divided into two parts: single and double ionization.

In the first part, we studied the momentum vectors of low energy electrons generated by short laser pulses of wavelengths varying from 400 to 800 nm with atomic and molecular targets with intensities in the tunneling region. Most of the structures observed in the momentum spectra of atomic and molecular targets can be explained as due to above-threshold ionization, and Freeman resonances. The most significant structure in our observed spectra is the angular structure in the lowest part of the momentum image, and this is attributed to the diffraction pattern evolved by tunneling electrons. Surprisingly, we observed that the structure produced by the electrons from high Rydberg states is independent of the internal structure of the target atom and molecules. The same work is extended to aligned molecules. The basic idea of this part of the work is to see whether the angular distribution of electrons from aligned molecules resembles the orbital structures of the molecules. The rotational revival structure was used to align the molecules. We observed pronounced energy and angular structures of the momentum images which show a dependence on the alignment of the molecule.

The last part of this work mainly focuses on double ionization, i.e. the removal of two electrons from the target atoms sequentially by a short laser pulse. Measuring the complete momentum vector of Ar^{2+} and Ne^{2+}, we demonstrate that these can be used to extract the angular correlation between two electrons sequentially released in the circularly polarized pulse. We demonstrate how the measurement of full momentum vectors of the doubly ionized argon and neon ions can be used to extract the time gap of the two emissions.

MOMENTUM IMAGING STUDIES OF ELECTRON AND ION DYNAMICS IN A STRONG LASER FIELD

by

CHAKRA MAN MAHARJAN

M. Sc., Tribhuvan University, Nepal, 1992
B.Sc., Tribhuvan University, Nepal, 1989

A DISSERTATION

submitted in partial fulfillment of the requirements for the degree

DOCTOR OF PHILOSOPHY

Department of Physics
College of Arts and Sciences

KANSAS STATE UNIVERSITY
Manhattan, Kansas

2007

Approved by:

Major Professor
C. L. Cocke

Copyright

Abstract

An underlying goal of studying atomic or molecular dynamics with short laser pulses is to reach a time scale short enough to study the evolution of the system in the time domain. In this thesis, the strong field ionization of atoms and molecules has been investigated with the highly resolved technique known as cold target recoil momentum spectroscopy (COLTRIMS). The thesis can be divided into two parts: single and double ionization.

In the first part, we studied the momentum vectors of low energy electrons generated by short laser pulses of wavelengths varying from 400 to 800 nm with atomic and molecular targets with intensities in the tunneling region. Most of the structures observed in the momentum spectra of atomic and molecular targets can be explained as due to above-threshold ionization, and Freeman resonances. The most significant structure in our observed spectra is the angular structure in the lowest part of the momentum image, and this is attributed to the diffraction pattern evolved by tunneling electrons. Surprisingly, we observed that the structure produced by the electrons from high Rydberg states is independent of the internal structure of the target atom and molecules. The same work is extended to aligned molecules. The basic idea of this part of the work is to see whether the angular distribution of electrons from aligned molecules resembles the orbital structures of the molecules. The rotational revival structure was used to align the molecules. We observed pronounced energy and angular structures of the momentum images which show a dependence on the alignment of the molecule.

The last part of this work mainly focuses on double ionization, i.e. the removal of two electrons from the target atoms sequentially by a short laser pulse. Measuring the complete momentum vector of Ar^{2+} and Ne^{2+}, we demonstrate that these can be used to extract the angular correlation between two electrons sequentially released in the circularly polarized pulse. We demonstrate how the measurement of full momentum vectors of the doubly ionized argon and neon ions can be used to extract the time gap of the two emissions.

Table of Contents

List of Figures

List of Tables

Acknowledgements

First of all, I would like to thank all those people who have contributed to the success of this work.

I would like to express my deepest gratitude to Prof. C. L. Cocke for giving me the opportunity to carry out this exciting work in his group. His outstanding scientific mind motivated me to handle every single problem at hand during the course of my PhD work. He is a tireless supporter and great promoter of our work. He has not only taught me the relevant physics of the project but also shown the beauty of physics. He always creates a wonderful atmosphere in which to learn, both collegial and intellectually challenging.

I am very grateful to Prof. Peter Pfromm for serving as the chairperson of my PhD committee and giving me useful suggestions.

I am thankful to Prof. Brett DePaola, Prof. Brett Esry, Prof. Douglas MacGregor, and Prof. Zhengu Chang for giving their valuable time to serve in my supervision committee and for suggesting interesting directions for my work.

I am very grateful to Prof. Igor Litvinyuk for providing most of the ideas realized in the alignment experiment, giving me advice and helping in all questions.

I was very fortunate to work closely with former postdoc Dr. Ali Alnaser, who has a sharp sense of exactly which experiment to perform in order to answer the scientific question at hand. His style of work and quick understanding of the problem always taught me how to go ahead as a research student. I am indebted to Dr X. M. Tong and Dr Toru Morishita for providing their theoretical guidance to understand the complicated experimental results, and also for being always open for discussions. I would like to thank Mike Wells, Al Rankin and Scott Chainey for their hands-on help in solving any kind of problem in my setup during the experiment. I am indebted to Carol Regehr for her help with the correction of my thesis.

I would like to express my sincere thanks to all my colleagues: Predrag Ranitovic, Irina Bocharova, Dipanwita Ray, Ben Gramkow and Maia Magrakvelidze and former group members Steven Voss and Birte Ulrich.

Finally, I would like to express my deepest gratitude to my wife Hasana for all of the love, support, and patience she has given me over the past years.

Dedication

To my late father Ram Maharjan and my Mom

CHAPTER 1 - Introduction

The interaction of intense ultrafast light with matter has a wide range of technological applications already, from surgery to the ignition of nuclear fusion; however, there are still many open questions regarding the underlying fundamental physics of this interaction. The main goal of this study is to add to this body of knowledge. An extremely clean way to test the structure and dynamics of this interaction is to place just one single atom or molecule in the laser focus and examine it in the time domain. This study is possible only if the length of the pulse is available on the time scale of the dynamics of interest.

Owing to the rapid progress in femtosecond laser technology, in particular since the invention of the titanium-sapphire (Ti-S) femtosecond laser, generation of laser fields with strengths comparable to inner atomic fields has become routine. This opened the door to a completely new study in the AMO field. On the other hand, experimentally, the advent of KHz repetition rate, high-peak power lasers has provided an essential tool necessary to span the entire intensity range of importance.

In 1964 Keldysh [19] showed that at infrared and visible wavelengths the dynamics of strong field atomic ionization undergoes a change in character as the intensity increases. In a weaker field, a bound electron will be promoted into the continuum by the simultaneous absorption of enough photons to increase its energy above its ionization potential. This is called the multi-photon process. However, as the laser intensity increases, a completely different mode of escape becomes possible. At large distances from the nucleus the electrostatic attraction of the ion core can be overwhelmed by the laser's instantaneous electric field, producing a barrier through which the valence electrons can tunnel. Once an electron in a strong field has made the transition into the continuum from its initial bound state, its motion is dominated by its interaction with the external laser field.

Laser pulses of a few optical cycles are routinely available in several labs around the world. The search for shorter pulse lengths is motivated by two factors. First, a shorter optical pulse affords a higher time resolution in pump probe experiments, allowing a wealth of physical processes to be studied including rotational revival, vibration of wave packet, ionization and dissociation. Second, a short optical pulse can produce extremely high powers with only

moderate energies. This makes it possible to study the electron and molecular dynamics in the time domain more precisely and accurately. Moreover, the electric field strength of such a pulse is comparable to the field which binds electrons in the outermost orbit of atoms (~5 x10^9 V/cm). Further, the extremely high intensity (~10^{20} W/cm^2) of such a laser can be obtained by squeezing all the photons of such an ultrashort pulse to a very tiny area with the help of optical devices like a mirror or a lens with the exploitation of Gaussian properties of the beam. Surprisingly, these intensities are even greater than all the sunlight incident on earth (2.7x10^{17} W) focused on a pinhead.

One of major problems of such a focusing arrangement is that everything inside the interaction volume will be ionized, thus creating the problem of identifying the real species from the interaction volume. Moreover, if the size of the gas jet is comparable to the focal volume, the real species of gas experiences a gradient of intensity due to different iso-intensity contours. Instead of having events only from the peak intensity, there is a greater chance to have events from different iso-intensity contours, making it difficult to record the real events. This problem is more serious for an electron experiment. Arranging proper jet size controlled by piezoelectric slits and producing an ultrahigh vacuum in the chamber help greatly to partially remedy this problem.

The first part of this work mainly concerns the dynamics of electrons released from single ionization of atoms or molecules. Single electron emission from atoms exposed to intense short-pulse laser fields is one of the most fundamental and well studied reaction channels in nonlinear strong field physics. As laser intensities increase, atomic Rydberg levels as well as the ionization limit shift up by the pondermotive energy (wiggle energy of electron in laser field) U_p. At particular intensities the different highly excited (Rydberg) states shift into resonance with an integer number of photons, and survive longer in the laser pulse (long life time), leading to a strong ionization rate. It can then happen that ionization from the excited states occurs before the intensity has appreciably changed, so that it always proceeds at the intensity required to fulfill the resonance condition, and accordingly, at some certain value of pondermotive shift. If the peak intensity is higher than the resonant value, the resonant condition can be fulfilled somewhere in the laser focus [1]. The various Rydberg–state resonances produce electrons that have different kinetic energies, which account for the subpeaks within each ATI (above-threshold-ionization) order. Given the resonant nature of this process, the photoelectron peaks

corresponding to specific transient resonances appear in the kinetic energy spectra and they do not shift with absolute laser intensity. Therefore the bound-to-bound transition is much stronger than direct ionization; and once populated, the excited states ionize easily.

At higher intensities any intermediate state may be completely deformed by the laser field. However, numerical simulations [2] have shown that some excited states may remain surprisingly stable, and can even be induced by the laser field (light induced states). The part of the wave function that tunnels out of the atom might effectively populate these extended quasi-bound states producing resonant-like structures in the photoelectron spectra [3].

We present most of the studies with two dimensional momentum space images recorded with linear polarization and integrated over the azimuthal angle. All the interesting features can be seen explicitly over a range of energies. The well known above-threshold ionization process can clearly be observed from the lower to higher energy part of the spectrum, whereas a more complex diffraction structure can be observed in the lower energy part of the spectrum. A ring structure, with alternate maxima and minima along it, gives a well-defined angular momentum of the electron in that energy domain. This angular structure appears to be determined less by the quantum numbers of the Rydberg states than from the characteristics of the continuum electrons including diffraction of these electrons in the field of the ion [4]. Also a theoretical explanation has been attempted for the underlying mechanisms for those processes, by D. Arbó *et al*. [5], M. Wickenhauser *et al*. [6,7] and most recently by Z. Chen *et al*. [8] and T. Morishita *et al*.[9]

The resolution in every observed spectrum is determined by the momentum resolution of our technique, as well as the bandwidth of the laser. The high resolution in the lower energy part of the spectrum makes it possible to identify the most intensity-dependent and -independent structures. The study of these energy and angular structures has been extended to randomly oriented as well as aligned linear O_2 molecules. Comparing the spectra of the electrons from molecules oriented parallel and perpendicular to the polarization direction, we attempt to understand the emission process related to the orbital structure of these molecules. The rotational revival structure has been used to find the exact delay between the pump and probe required to set molecules oriented parallel and perpendicular to the polarization direction.

The second part of this work shows the dynamics of two electrons released sequentially from the argon and neon atoms. The process of double ionization of atoms or molecules can be categorized into either sequential or nonsequential, depending on the intensity of the laser at

hand. Nonsequential ionization occurs when the first electron is emitted near the peak of a laser pulse and the electron's subsequent revisit of the parent atom driven by the reverse field in another half cycle of the pulse. The second electron is knocked out by the returned electron. In the sequential process, both the electrons are released by the field and the process is more probable when the pulse is very short. An electron can be released sequentially either by tunneling through the resultant potential produced by the combination of the field of the laser pulse and the Coulomb field of the core or over-barrier. The former process has been studied extensively and the theoretical approach was first considered by Perelomov, Popov, and Terent'ev [10] and further developed by Amosov, Delone and Krainov [11]. If the pulse is very short, the second process is more probable. The electric field of the pulse rises so quickly that both valence electrons can be emitted over this short duration of time.

In our study of double ionization, we have measured the full momentum vector of doubly charged argon and neon ionized in a circularly polarized pulse. We demonstrate in Chapter 7 how the angular correlation of two electrons released sequentially influences the momentum vector of the doubly charged ion. We demonstrate how the measurement of the full momentum vectors of the doubly ionized argon and neon ions can be used to extract the time gap between the two emissions using a pulse envelop as a minute hand of a clock. This experiment could be a reference for another experiment involving the measurement of momentum vectors of two electrons independently. The ultimate goal of this experiment is to measure the time difference of two emissions of electrons sequentially using the optical cycle of a pulse as a clock. This would be a second hand clock if the pulse length were on the order of an optical cycle.

All the experimental observations for the present study were taken in the LASER COLTRIMS facilities in the J. R. Macdonald Laboratory of the Department of Physics in Kansas State University. The COLTRIMS technique involves the standard imaging technique able to measure the complete kinematics of the reaction products from the reaction zone.

CHAPTER 2 - Theory

2.1 Single ionization

Most atoms and molecules ionize rapidly when subjected to laser intensity greater than $3x10^{13}$ W/cm^2. Depending on the strength of the field experienced by an atom or molecule in a pulse, both single ionization and multiple ionizations are possible. This section is an overview of different mechanisms of the single ionization processes: multi-photon, above-threshold ionization, tunneling, and barrier suppression.

2.1.1 Multi-photon process

Single electron emission from atoms exposed to intense short pulse laser fields is one of the most fundamental and well studied reaction channels in nonlinear strong field physics. Different well known mechanisms are responsible for the single ionization of an atom or molecule in a strong laser field. These mechanisms can be thought of as ionization either by absorption of a single photon or several photons depending upon the energy of photon used. In a synchrotron radiation experiment, single ionization can easily occur by absorbing one photon, which is analogous to the photoelectric effect where the photon energy is divided into two parts, partly used to put an electron into the continuum, and the rest as kinetic energy of the electron

$$KE = h\nu - I_P . \tag{2.1}$$

Here I_p is the ionization potential of an atom or a molecule. The energy of a photon of an IR laser is so small (1.55eV at 800nm) that a single photon is typically not enough for ionization. In such a case, a loosely bound electron in a valence orbit might absorb just enough photons for ionization, or more. The former process is known as multi-photon and the later is called above-threshold ionization (ATI). In early experiments the multi-photon process was successfully explained by lowest-order perturbation theory [12, 13].

The n-photon ionization rate is given by

$$W = \sigma_n I^n \tag{2.2}$$

where n is the minimum number of photons needed for ionization, σ_n is the generalized cross section, and I the intensity of laser light. The ionization rate increases like I^n. For a very high order process, this is very difficult to observe. It is very clear from the expression that the process is highly nonlinear. However, this intensity scaling breaks down at the saturation intensity above which there is a change in intensity dependence [14].

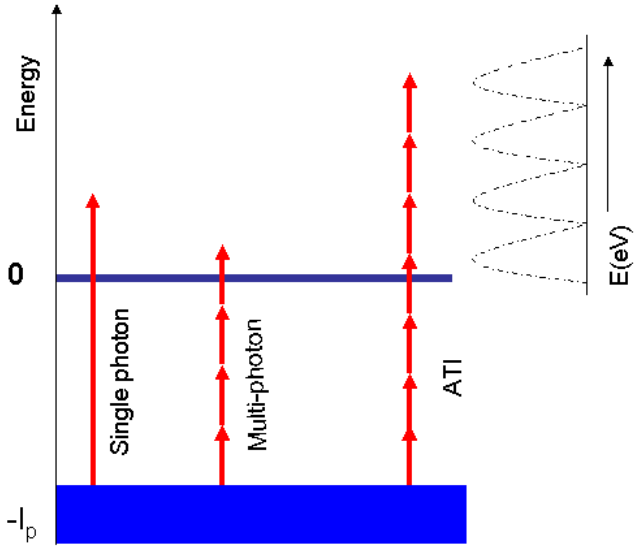

Figure 2.1 Schematic of the three modes of photo-ionization: Single photon, multi-photon, and above-threshold ionization

2.1.2 Above-threshold ionization

When an atom is in an intense optical field, it may absorb more photons than the minimum requirement during the ionization process. This process, first reported by Agostini *et al.* [15] over 25 years ago, is known as above-threshold ionization (ATI). In the photoelectron energy spectra, ATI typically manifests itself as peaks that are separated by the photon energy as shown in Figure 2.1. A typical photoelectron spectrum at high intensity consists of several features: intensity-dependent and -independent features at lower energy, and a plateau part until it terminates at a cutoff. The single ionization part of this study is mainly concerned with the range of energy 0 to $2U_p$ which is populated by "direct electrons." The semi-classical treatment has proven to be very successful to explain some of the high energy features of the spectral envelope, e.g. the existence of a high energy plateau extending to well defined cutoff at $10U_p$ [16].

2.1.3 Resonances (substructure in ATI)

In the short pulse limit (100fs-25fs), each ATI peak of the photoelectron spectra exhibits substructures (satellite peaks). The substructure is more pronounced in the lower energy part of the spectrum where the resolution is good enough to observe experimentally. These peaks can be attributed to the transient resonances of highly excited Rydberg states [17] with the harmonics of the laser field. As the laser intensity increases, the ionization limit and higher Rydberg states shift by the pondermotive shift U_p [17]. The pronounced peaks corresponding to these transient resonances appear in the photoelectron spectrum, and the position of these peaks remains unchanged even with variation in intensity.

Stark Shift:

The second order perturbation theory results in a shift of energy level i of an atom by an amount ΔE_i which can be expressed [18] as

$$\Delta E_i = \frac{e^2 E_o^2}{4m\omega^2}\left[1 - \sum_{i \neq f} f_{fi} \frac{\omega_{fi}^2}{\omega_{fi}^2 - \omega^2}\right] \quad . \tag{2.3}$$

In this expression, the sum is over all the intermediate states of the electron, $h\omega_{fi}$

is the difference in energies of initial and final states, and f_{fi} is the oscillator strength. For very weakly bound states, satisfying the condition $\omega_{fi}<<\omega$,

$$\Delta E_i = \frac{e^2 E_o^2}{4m\omega^2} \tag{2.4}$$

which is equal to the wiggling energy of an electron in a laser pulse (pondermotive energy), as weakly bound states are expected to behave much like free electrons. At the opposite extreme, very deeply bound states (for example the ground state) have energy spacings to other levels that are much larger than a photon, $\omega_{fi}>>\omega$, the sum is approximately equal to the sum of oscillator strengths which is identically 1. This leads to a zero energy shift. This simple argument is used to justify the most common assumptions in understanding bound states in an AC field – ground states undergo basically no shift compared to excited states. The weakly bound states and the free electrons in the continuum shift by the pondermotive potential U_p. This has the net effect of increasing the ionization potential.

The ionization potential and the energy of highly excited states of an electron in an atom increase in a laser field by an amount equal to the pondermotive energy (quiver energy gained by the electron in an oscillating field of a pulse), which is proportional to the laser peak intensity and the square of the wavelength of light used as expressed by

$$U_p = 9.33\times10^{14} I(W/cm^2)\,(\lambda(\mu m))^2 . \tag{2.5}$$

Generally the kinetic energy of the electron ($E_{Kinetic}$) after absorbing the n photons is expressed as

$$E_{Kinetic} = nh\nu - (I_p + U_p) . \tag{2.6}$$

Now consider the multi-photon resonance of any particular Rydberg state with pondermotive shift after absorbing N_1 photons. If the electron in that state absorbs additional M photons as shown in Figure 2.2, then the previous equation is modified,

$$E_{Kinetic} = (N_1 + M)h\nu - (I_p + U_P) . \tag{2.7}$$

Further

$$E_{Kinetic} = E_{res} + Mh\nu - (I_p + U_P) , \tag{2.8}$$

where $E_{res} = N_1 h\nu$. But if the energy of the transient state also increases by the pondermotive energy, then

$$E_{Kinetic} = E_{Ryd} + U_p + Mh\nu - (I_p + U_P), \tag{2.9}$$

$E_{Ryd} + U_p = E_{\mathrm{Re}s}$ where E_{Ryd} is the energy of the Rydberg state without pondermotive shift. This equals

$$KE = E_{Ryd} + Mh\nu - (I_p). \tag{2.10}$$

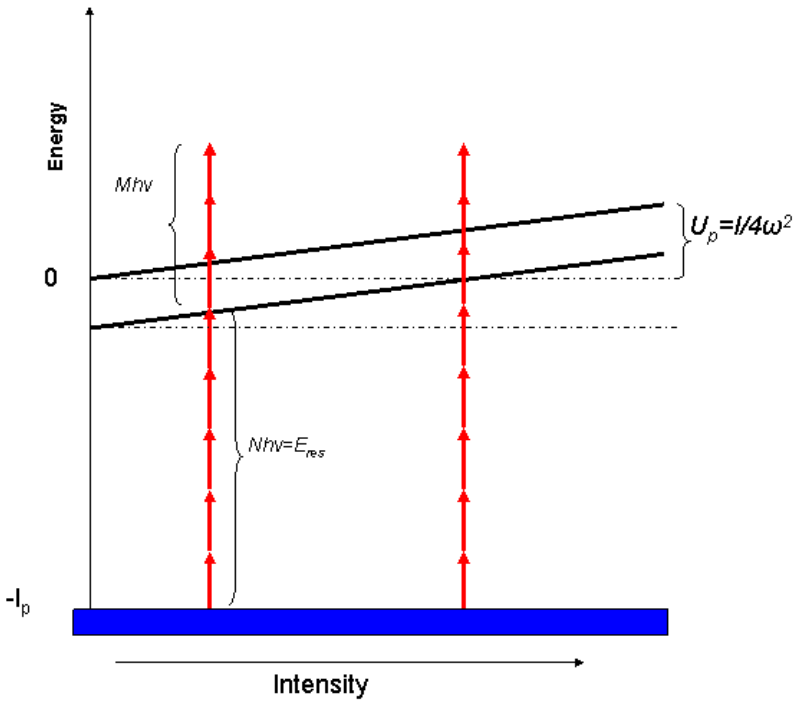

Figure 2.2 : Schematic representation of the above-threshold process. The ionization level and the higher Rydberg state are shifted by the pondermotive potential (Up), whereas the tightly bound state remains unperturbed. It also shows the resonance of particular highly excited states with the harmonics of the photons.

Thus, it is found that the kinetic energy of the electron emitted from the pondermotively shifted transient state (the shift is also the same for the ionization level) is completely independent of the laser intensity, but solely determined by the field free binding energy of the state. If some numbers of photons are resonant with an excited state of the system, the rate of

ionization will be much greater than for purely non-resonant ionization. This is because of the larger cross-section of the real intermediate state. For a peak intensity I_o, a laser pulse must ramp through all intensities below I_o. As the pulse grows in time, the Stark shift will increase and bound excited states of the atom will become resonant for a short time.

2.1.4 Tunneling ionization

The evolution of tunneling ionization from the multi-photon process is mostly determined by the range of intensities considered. In general, at intensities between 10^{14} and 10^{15} W/cm^2, the laser field is sufficient to distort the Coulomb potential strongly. Hence it becomes possible for the electron to tunnel through the barrier formed by the suppressed atomic potential. Unlike the multi-photon process which involves the transition between states with different energies, the tunneling is associated with the transition through a barrier, where initial and final states have the same total energy.

2.1.4.1 Keldysh Theory

Keldysh realized (1965) [19] that an alternative mechanism for ionization in a strong field could take place under specific conditions. At fairly modest intensities (~ 10^{14} W/cm^2) the normal multi-photon excitation route for ionization via intermediate states applies. If the field strength of the incident laser is strong enough and frequency is low, then, within the quasi-stationary approximation, the field is able to distort the atomic potential to such an extent that a potential barrier is formed through which the electron in the well can tunnel out. The ionization in the strong field is via multi-photon or tunneling, and can be well classified according to the so-called Keldysh parameter,

$$\gamma = \sqrt{\frac{I_p}{2U_p}}\,. \qquad (2.11)$$

Here I_p is the ionization potential of an atom, and U_p the pondermotive energy of the electron. If $\gamma < 1$ then tunneling dynamics dominates the process, but if $\gamma > 1$ then multi-photon dynamics will be significant.

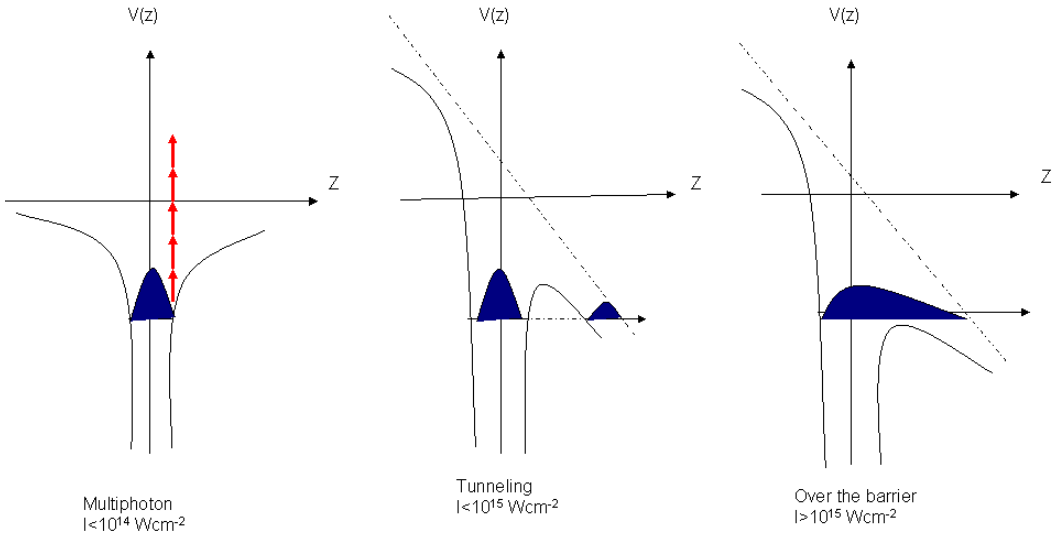

(a) (b) (c)

Figure 2.3: Schematic of the three different processes of strong field ionization. Figure (a) shows the ionization of an atom with the absorption of harmonics of photons at intensity below $I=10^{14}$ W/cm^2. As the intensity of light increases above 10^{14} W/cm^2, the atomic potential is distorted to such an extent that the bound electron comes out of the atom by tunneling as shown in (b). At even higher intensities, the electron is free to escape from the atomic potential without tunneling.

2.1.4.2 ADK Theory

The ADK tunneling model of ionization of an atom in intense laser fields has proved to be a central element in current theories of strong field physics. The key point of the theory is that substantial ionization occurs in such a short period (a fraction of an optical cycle), such that the electric field can be regarded as quasi-static. This theory is based on the ionization rate of a hydrogen-like atom in a static electric field with modification introduced for a many-electron atom [11].The basic point of the ADK model is that the ionization rate depends critically on the ionization potential of an atom.

The static tunneling ionization (ADK) rate [11] is given by

$$W_{stat}(F,0) = \frac{B^2(m)}{2^{|m|}|m|!}\frac{1}{\kappa^{\frac{2Z}{\kappa}-1}}\left(\frac{2\kappa^3}{F}\right)^{\frac{2Z}{\kappa}|m|-1} e^{-\frac{2\kappa^3}{3F}} \tag{2.12}$$

where F is the electric field for peak intensity and $\kappa = \sqrt{2I_p}$, $B(m) = C_l Q(l,m)$ and C_l measures the amplitude of the electron wave function.

$$Q(l,m) = (-1)^m \sqrt{\frac{(2l+1)(l+|m|!}{2(l-|m|)!}} \tag{2.13}$$

Here l and m are the angular momentum and its projection along the polarization direction.

The probability of ionization of atoms can be calculated using the expression

$$P = 1 - \exp[-\int_{-\tau}^{\tau} W_{stat}\, dt] \tag{2.14}$$

Here τ is the duration of a laser pulse. The value of P =1 corresponds to the saturation of single ionization. For a given intensity, all the atoms within the pulse are singly ionized. The saturation intensity estimated for a laser pulse of pulse length 8fs for argon is equal to $6\text{x}10^{14}$ W/cm^2 as shown in Figure 2.4.

For an atom in the strong laser field, the ionization occurs only in a fraction of the optical cycle. So the average ionization rate over the cycle can be calculated

$$W(F) = \frac{1}{T}\int_0^T W_{stat}(F,0)\, dt$$

$$= \left(\frac{3F}{\pi\kappa^3}\right)^{\frac{1}{2}} W_{stat}(F) \tag{2.15}$$

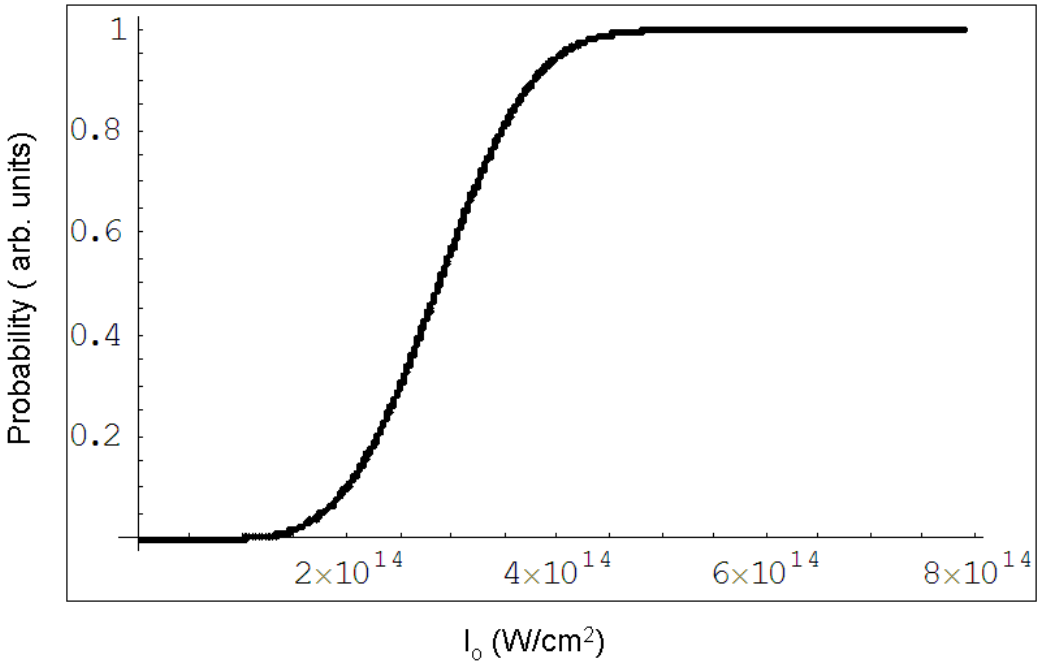

Figure 2.4: The plotting of yield of single ionization of an argon atom at 8fs pulse at different intensities using above equation (2.12) and (2.14)

2.1. 5 Barrier suppression ionization theory (over-barrier)

The multi-photon or tunneling of an electron from an atom or molecule in a laser field is critically determined by the strength of the electric field or peak intensity of a pulse. It is natural to raise the question in our mind of what happens to the potential barrier if the intensity is relatively very high. One of the answers to this problem is the barrier suppression model [20, 21] which successfully determines the threshold for the over-barrier process quantitatively.

For extremely high intensity and low frequencies, the ionization process may be viewed as the suppression of the Coulomb potential barrier as shown in Figure 2.3 (b). As the field strength is increased, it distorts the potential gradually making the barrier lower and narrower over which the electron may tunnel. Eventually the electron is no longer bound .The electrons escape to the continuum states by going 'over-barrier' as shown in Figure 2.3 (c).

For simplicity, this theory considers a one-dimensional ionization model. It begins with the superposition of the Coulomb potential and a quasi-static laser field. The resulting total potential is written as

$$V(x) = -\frac{z}{|x|} - \varepsilon x \quad . \tag{2.16}$$

Here z is the effective charge and ε is the electric field of the pulse.

This potential has a relative maximum located at x_{max} which can be easily found by setting $\left.\frac{\partial V}{\partial x}\right|_{X=X_{\max}} = 0$,

then

$$V(x_{\max}) = -2\sqrt{z\varepsilon} \tag{2.17}$$

$$\varepsilon = \frac{V^2}{4z} \quad . \tag{2.18}$$

The critical electric field necessary in order to permit the bound electron to escape without tunneling is

$$\varepsilon = \frac{I_p^2}{4z} \quad . \tag{2.19}$$

Thus the threshold intensity of the laser for over-barrier is

$$I_{th} = \frac{1}{2} c \varepsilon_o \varepsilon^2 \quad , \tag{2.20}$$

$$I_{Th}(W/cm^2) = 4.0 \times 10^9 \frac{I_o^4(eV)}{z^2} \quad . \tag{2.21}$$

The last expression is easy to use for calculating the threshold intensity for an electron for over-barrier. For example, the first and second ionization potentials of argon are 15.8 and 27.6 eV respectively. Substituting these values in expression (2.21) will give the threshold intensities necessary for the first and second ionization which are 2.49×10^{14} W/cm^2 and 5.75×10^{14} W/cm^2

respectively, through over-barrier. The process will be explained in more detail with the experimental results in chapter 7.

However, many atoms have saturation intensities which take place before I_{Th} is reached. This means that the atom did not survive the laser pulse's intensity rise past saturation (all atoms are well ionized by multi-photon ionization well before). In general, the over-barrier process dominates for intensities above 10^{15} W/cm^2.

2.2 Double ionization

The strong field double ionization of atoms is one of the simpler and hence more fundamental test cases for understanding many electron systems. The dynamical angular correlation and momentum distributions in continuum states are a few examples of some puzzles in few body dynamics which have not been clearly understood yet.

2.2.1 Sequential and nonsequential double ionization in a linearly polarized pulse

In the second part of the literature survey, we are mainly considering the double ionization processes, either with the tunneling or over-barrier process, other than due to a multi-photon process. In the former process, the two bound electrons tunnel out of atoms one after another at different phase points of a pulse. In the latter case, if the field is strong enough to suppress the potential barrier created by the Coulomb field, they can escape from the well without tunneling. In both cases, each electron comes out independently at different times during the laser pulse. The former process is quantitatively explained by the ADK model [11] which has been very successful at explaining single ionization. Both tunneling and the barrier suppression processes are referred to as sequential ionization and in both cases the ionization is mainly due to the electric field of the laser pulse. The electric field of a laser pulse grows gradually or quickly depending upon the temporal size of a pulse. Overcoming the potential barrier depends on how short the pulse is and also on its intensity. The second electron also follows the same process at the higher electric field of the pulse. It hadn't been realized that there could be another route of double ionization until B. Walker *et al*. [22] published their astonishing result on the double

ionization of helium with a clear knee part separating the higher and lower intensity parts of the yield curve. The key physics behind the process has been first put forward by P. Corkum [23] in his paper in 1993 and Kulander [24]. The theory explained the path of the second emission considering the returned electron still in the laser field. The proposed model, popularly known as rescattering or simple man is based on semiclassical theory, and explained the puzzle at the knee part of double ionization of helium. It is actually the boundary between the two regions of ionization where either sequential or nonsequential ionization dominates the process of double ionization. This well known picture first treats the electron quantum mechanically during the tunneling process, and subsequently classically in the electromagnetic field of a laser pulse. The rescattering process involves three steps for double ionization. When an atom is in the laser pulse, the bound electron of the distorted potential well, first tunnels out of the atom at a certain phase of the positive optical half cycle of the pulse. During the next half cycle, the direction of the field reverses, and thus it drives the electron back to the parent atom. Depending on how much energy it has gained in the pulse, which in turn depends on the phase at which the electron was born, there is some probability that the electron can be recombined with the parent atom and reside at its ground state with release of the excess energy it has gained in the laser field, or that it knocks out a second valence electron and both escape in the same direction in another half cycle of the laser pulse [24]. The former process is called high harmonic generation [25]. Let us also look at another possibility, that if the re-scattered electron has not gained enough energy, it might only excite the second electron and later the second electron will be ionized by the field [26]. The rescattering process strongly depends on the type of laser polarization. The absence of rescattering phenomenon on switching the polarization of a pulse from linear to circular provides strong evidence for the theory [27]. The rescattering mechanism is inhibited by circular polarization since the rotating field does not drive the electrons back to their origin. Summarizing the strong field double ionizations:

I) Sequential ionization: field releases both the valence electrons [28]

II) Nonsequential ionization: The first electron tunnels out of the atom in the first half cycle of the field and is driven back to the same atom with the reverse field of the next half cycle. The returning electron knocks out a second electron.

III) Impact excitation followed by ionization: The electron returns with lower energy, first excites the second electron to a higher excited state, and later a subsequent laser field ionizes the excited electron.

In order to get deep insight into the rescattering process, first consider the motion of a charged particle in a linearly polarized laser field which is given by the oscillating electric field vector (ε) with envelope function $\varepsilon_o(t)$,

$$\varepsilon = \varepsilon_o(t)\cos\omega t \quad . \tag{2.22}$$

The electron within the pulse experiences the force due to the above field. The magnitude of force is simply expressed by the Lorentz force equation,

$$F = q\left[\varepsilon + V \times B\right] \tag{2.23}$$

where the first term is the force experienced by an electron due to the electric field vector and the second term is the result of charge particle q moving with velocity V in the magnetic field. The second term can be neglected compared to the range of intensity considered here. The resultant momentum (P) of electron in the laser field can be found by integrating from born time (t_o) to at any instant of time (t) is expressed as

$$P(t_o,t) = \int_{t_o}^{t} \varepsilon(t')\,dt' = q\int_{t_o}^{t} \varepsilon_o(t')\cos\omega t'\,dt' \tag{2.24}$$

$$= \frac{q}{\omega}[\varepsilon_o(t')\sin\omega t']_{t_o}^{t} + \frac{q}{\omega}\int_{t_o}^{t} \varepsilon_o'(t')\sin\omega t'\,dt' \tag{2.25}$$

$$\approx \frac{q}{\omega}[\varepsilon_o(t')\sin\omega t']_{t_o}^{t} - \frac{q}{\omega}\frac{\varepsilon_{\max}}{\tau\omega}[\cos\omega t']_{t_o}^{t} \tag{2.26}$$

where $\varepsilon_o' = \frac{\varepsilon_{\max}}{\tau}$, ε_{max} is the maximum electric field during the pulse (τ). If the pulse duration is long compared to the oscillation period, the second term can be neglected.

$$P(t_{o,}t) = \frac{q}{\omega}[\varepsilon_o(t)\sin\omega t - \varepsilon_o(t_0)\sin\omega t_o] \tag{2.27}$$

Here the first term explains the oscillatory motion of an electron in an alternating field and the second term corresponds to the drift momentum, the magnitude of which is determined by the phase ωt_o when the electron was born. As the laser pulse passes by, the oscillatory motion vanishes with $\varepsilon_o(t)$ and the final drift momentum (P_{Drift}) remains

$$P_{Drift}(t_o) = \frac{q}{\omega}[\varepsilon_o(t_0)\sin\omega t_o] \tag{2.28}$$

The charged particle gains maximum drift momentum if it is ionized at the zero crossing of the field,

$$P_{\max} = \frac{q}{\omega}\varepsilon_o(t_0) = 2q\sqrt{U_p} \tag{2.29}$$

where U_p is the pondermotive energy of the electron. It is equal to the quiver energy gained by an electron in the oscillating field of a pulse. Moreover, it is also clear that the magnitude of the energy gained by the electron is also determined by the phase at which the electron was born. The magnitude of quiver motion is determined by the strength of the field.

$$U_p = \frac{e^2\varepsilon^2}{4m\omega^2} \tag{2.30}$$

$$U_p(eV) = 9.33\times 110^{-14} I(W/cm^2)(\lambda\,\mu m)^2 \tag{2.31}$$

For example, if $I_0 = 1\times10^{14}$ W/cm^2 and $\lambda = 0.8$ μm, the pondermotive energy of the electron is equal to 5.97eV. The electron trajectory ($x(t)$) can be found by

$$\int_{t_o}^{t} dx = \frac{q}{m\omega}[\int_{t_o}^{t}\varepsilon_o \sin\omega t dt + \int_{t_o}^{t}\varepsilon_o \sin\omega t_o dt] \tag{2.32}$$

$$x(t) = \frac{q\varepsilon_o}{m\omega^2}[(\cos\omega t_o - \cos\omega t) + (\omega t - \omega t_o)\sin\omega t_o] \tag{2.33}$$

Here, the last equation describes the bunch of trajectories of particles undergoing the influence of the laser electric field. The equation explicitly explains how these trajectories are determined by the two phase factors, return phase (ωt) and birth phase (ωt_o) respectively. Therefore, the question of how much energy an electron can gain from the laser field depends on the birth phase of the optical cycle. Apparently, the electron born at the peak laser field will not gain any energy from the field. However, if an electron is born close to the peak field, it will gain maximum energy. Figure 2.5 shows the electron trajectories in the electric field of the laser pulse.

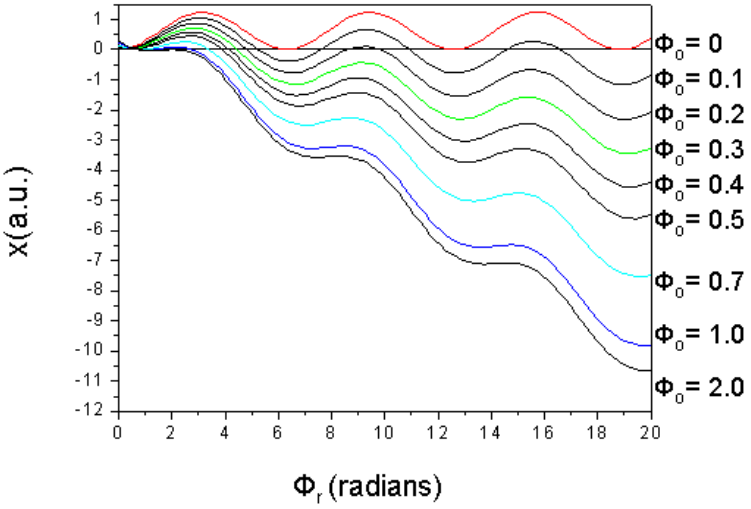

Figure 2.5: Electron trajectories in the electric field of a laser pulse obtained from Eq.(2.33) for different birth phases(ωt_o). It can be noticed clearly from the above electron motion that some electrons return to the atom several times, some return only once whereas some never return to the parent atoms. All these conditions are determined by the birth phases.

$$E = \frac{P^2}{2m} \tag{2.34}$$

$$= \frac{q^2 \varepsilon_o{}^2}{2m\omega^2}[\sin\omega t - \sin\omega t_o]^2 \tag{2.35}$$

$$= 2U_p[\sin\omega t - \sin\omega t_o]^2 \tag{2.36}$$

For a direct electron without rescattering, the maximum possible energy that an electron can have is two times the pondermotive energy ($2U_p$) [29]. The maximum energy that the returned electron can have from the field is equal to $3.17U_p$ corresponding to the phase at 109^o or 17^o as

shown in Figure 2.6. If the returned electron backscatters, the maximum energy of the electron is given by

$$E = (\sqrt{2U_p} + \sqrt{3.17U_p})^2 \approx 10U_p \tag{2.37}$$

Characteristics of electron spectra.

Basically, all the photoelectron spectra consist of the two distinct parts associated with the electrons having low and higher values of energies depending on the phase at which they were born: the direct and re-scattered part of the envelope of the electron spectrum. The electron spectrum on the lower energy side up to $2U_p$ is mostly dominated by the direct electrons with very low scattering probability. The comparatively flat part of the spectrum beyond $2U_p$ is a consequence of the elastically rescattered and backscattered electrons. The spectrum falls off several orders of magnitude over this region and forms a plateau region for re-scattered electrons. The plateau extends up to $10U_p$ with distinct cutoff [16].

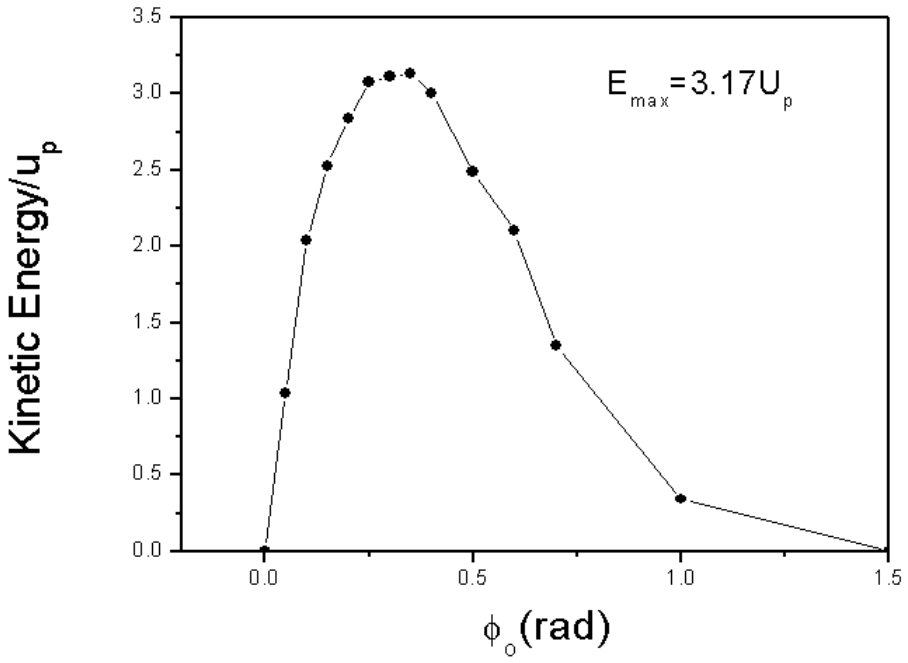

Figure 2.6: The kinetic energy of returned electrons to the core expressed in units of U_p as a function of birth time (t_o). It is seen that the maximum possible kinetic energy of returned electron is equal to 3.17 U_p.

2.2.2 Sequential double ionization in a circularly polarized pulse

The single and double ionization in the circularly polarized pulse are found to occur either by tunneling or by the over-barrier process, depending on the shortness of the pulse. If the pulse is of the order of a few optical cycles, the faster rise time of the pulse produces both single and double ionization within a very short time, even before reaching the peak of the pulse. The potential barrier is distorted by the field to such an extent that the bound electrons in the well can exit without tunneling [21]. Therefore over-barrier becomes the dominant process for sequential double ionization.

In circular polarization the amplitude of the electric field varies smoothly with time. Therefore the ionization process is not modulated with the rapidly changing electric field as for a linearly polarized pulse. The final direction of the electron in circular polarization rotates with the electric field vector. Thus motion consists of a large drift momentum in the direction normal to the electric field direction at the time of ionization and a circular component whose velocity goes to zero as the field goes to zero [30,31]

Consider a circularly polarized pulse. Its instantaneous electric field can be expressed by

$$\varepsilon = \varepsilon_o(t)\left(\hat{x}\sin\omega t + \hat{y}\cos\omega t\right) \tag{2.38}$$

Let us consider only one component of the field at a time:

$$\frac{dv_x}{dt} = \frac{e\varepsilon_x}{m} = \frac{e\varepsilon_o(t)}{m}\sin\omega t \tag{2.39}$$

Here, v_x is the x component of velocity. Integrating the expression from time t_o to infinity will give the magnitude of the x component of drift velocity. Once an electron leaves a pulse, the circular component goes to zero and it is left with drift momentum

$$v_x = \frac{e\varepsilon_o}{\omega m}\cos\omega t_o \tag{2.40}$$

or the x component of momentum is given by

$$P_x = \frac{e\varepsilon_o}{\omega}\cos\omega t_o\,. \tag{2.41}$$

Similarly the y component of drift momentum can be expressed as

$$P_y = -\frac{e\varepsilon_o}{\omega}\sin\omega t_o\,. \tag{2.42}$$

The resultant drift momentum is

$$P_{drift} = \sqrt{P_x^2 + P_y^2} = \frac{e\varepsilon_o}{\omega} \quad . \tag{2.43}$$

Unlike the ionization dynamics for a linearly polarized pulse in which the drift momentum of the electron is solely determined by the phase at birth, the drift momentum of charged particles in circular polarization depends on the electric field at the time of ionization.

$$P_{drift} = \sqrt{P_x^2 + P_y^2} = \frac{e\varepsilon_o}{\omega} \tag{2.44}$$

The expression shows that the drift momentum is independent of the phase factor. Furthermore, the electron will possess maximum drift momentum at the peak of the pulse where the electric field vector is largest, which is exactly opposite to the case of linear motion where the electron will have zero drift momentum.

If the pulse is long, there is greater probability that single ionization occurs at the peak of the pulse. In such a case we expect to see isotropic distribution of momentum in the polarizing plane. But if the pulse length is really small, both first and second ionization may occur even before reaching the peak value of the field. The drift momentum at the time of ionization is expressed as

$$P_{Drift}(t_1) = \frac{e\varepsilon_o(t_1)}{\omega} = \frac{eI_{P1}^2}{4z_1\omega} \tag{2.45}$$

$$P_{Drift}(t_2) = \frac{e\varepsilon_o(t_2)}{\omega} = \frac{eI_{P2}^2}{4z_2\omega} \tag{2.46}$$

where $\varepsilon_o(t_1)$ and $\varepsilon_o(t_2)$ are the over-barrier fields necessary for single and double ionization, and they are uniquely determined by the first (I_{P1}) and second ionization potential (I_{P2}) of an atom.

CHAPTER 3 - Experimental technique

This section of the dissertation provides an overview of the experimental technique with a brief introduction of the laser system for generating ultrashort pulses, pulse diagnostics, and the current status of the complete COLTRIMS technique.

3.1 Introduction: Short pulse generation

The production and measurement of ultrashort electromagnetic pulses is one of the most rapidly growing fields of modern physics. Recent technical achievements in ultrafast optics have permitted the generation of light pulses comprising only a few optical cycles. The spatial extension of these pulses along the direction of propagation is limited to a few times the wavelength of radiation in the visible and near infrared spectral ranges [32]. The pulses are delivered in the diffraction limit and hence focusable to a spot size comparable to the wavelength (a few micrometers in diameter). As a consequence radiation can be temporarily confined to a few cubic micrometers at the focus of a lens or spherical mirror (parabolic mirror). Because of this, peak intensities higher than 10^{15} W/cm^2 can be easily achieved. The amplitude of the electric field (8.6×10^{10} V/m) at this intensity level approaches a value that exceeds the static Coulomb field experienced by an electron in the outermost orbit of atoms or molecules. Therefore, it opens a new route to study optical field (strong field) ionization.

The investigation of atoms and molecules in a strong laser field has benefited enormously from the rapid progress in femto-second laser technology in the past decade. One of the particularly remarkable achievements is the generation of pulses of fewer optical cycles. The desire for shorter pulses in the AMO field thus relies on the following factors:

1. It makes it possible to carry out very highly time resolved experiments including pump probe experiments associated with fast molecular and atomic phenomena including vibration and rotation.

2. Shorter pulses result in higher peak power.

3.2 Chirped pulse amplification

The basic purpose of the laser system used in strong field research is to generate the highest possible energy in the shortest period of time. The system mainly consists of an oscillator for the generation of short pulse duration and a pulse train and amplifier for amplification of the energy of a pulse. The energy of the output of the oscillator is usually very small, of the order of 10^{-9} J. In order to get the energy of a pulse in the scale of a few mJ, it is necessary to amplify the output energy of the oscillator by several orders of magnitude (order 10^{6}). It is also very important that the amplifier must have a broadband to cover fully the frequency spectrum of the input; otherwise, the missing of any frequencies ultimately leads to lengthening the pulse. In order to avoid damage to the amplifier with the input pulse via self focusing because of the highly strong nonlinear refractive index, amplification is achieved by a chirp pulse amplification mechanism [33, 34]. In chirp pulse amplification as shown in Figure 3.1, the pulse to be amplified is first stretched in time into its frequency components by dispersive media which consist of a pair of gratings, so that a chirped pulse is generated with a band of frequencies stretching from red to blue. At the same time it reduces the peak intensity of the pulse and it is very suitable for safe amplification. At the output, another pair of gratings is used to recombine the dispersed frequencies creating a short pulse with extremely large peak intensity. Finally, the resulting amplified short pulse is focused on a small area. After focusing, intensities can be achieved up to 10^{18} Wcm^{-2} routinely. The chirped pulse amplification system currently available in the JRM Laboratory at Kansas State University employs Ti:Sapphire both for the oscillator and the amplifying medium. The excellent thermal conductivity and favorable thermo-optic properties of the Ti:Sapphire and the availability of KHz-rated solid state pump sources opened the way to implementing chirped pulse amplification at the KHz repetition rate. However the spectral width directly generated by the chirp pulse amplifier is limited by the finite bandwidth of gain narrowing during the amplification process. Consequently, the shortest pulse duration that could hitherto be directly generated from the multi-TW amplifier chains with repetition rates smaller than 15 Hz is the range of 16 fs to 25 fs.

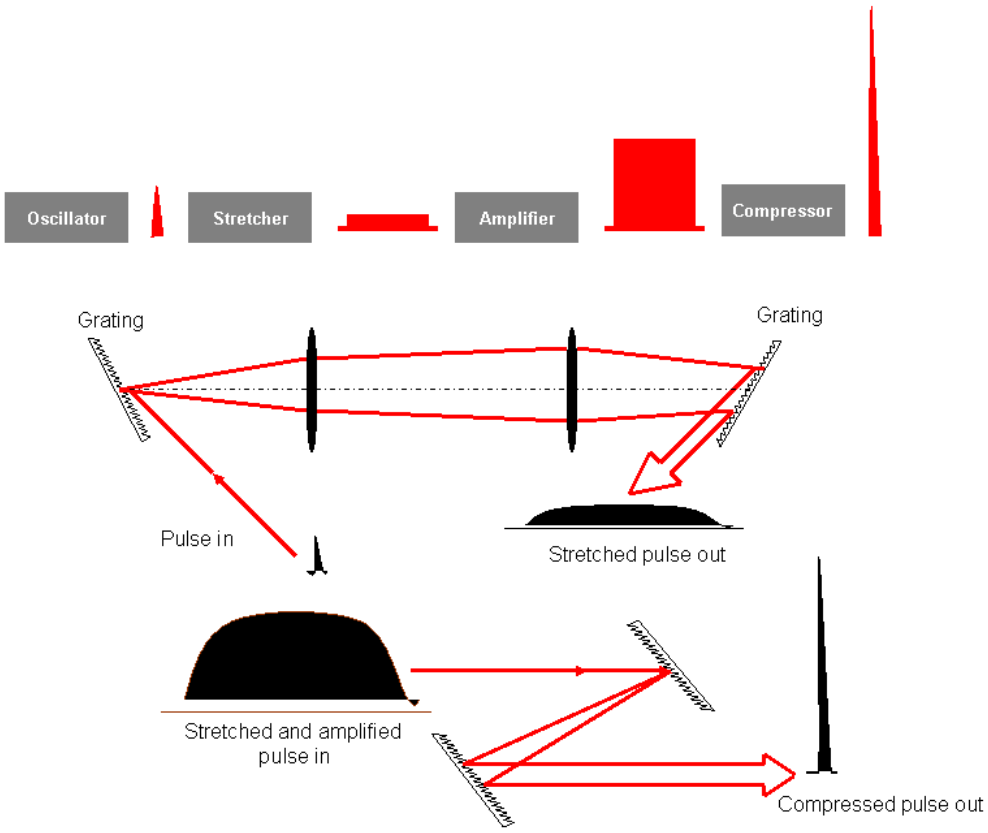

Figure 3.1: Schematic of the principle of the chirped pulse amplification (CPA) method. An oscillator produces a short pulse, which is stretched in time into its frequency components. As a result, the peak intensity of the pulse is lowered, so that it can be used for amplification without damaging the amplifier. The amplified chirped pulse is then compressed in time. The final pulse after the compressor is short with high intensity.

3.3 Frequency broadening in hollow core fiber

The pulse compression technique generally relies on spectral broadening via non-linear propagation and subsequent compression of spectral chirps in broadband negative dispersion lines. Spectral broadening can be achieved by nonlinear propagation in a waveguide filled with a noble gas at a certain pressure. Wave propagation along hollow guides (fiber) can be thought of as occurring through grazing incidence, reflections at the dielectric inner surface.

The long pulses (~30fs) with the pulse energy (~1mJ) from KLS are subsequently fed into a fused silica capillary with an inner diameter of 400 μm (~2/3 of the size of focus of the focusing mirror). The capillary is kept straight in a v groove on an aluminum bar placed in a tube that is filled with argon at a pressure of a few bars. Antireflection-coated fused silica windows of thickness 0.5 mm are used at the entrance and exit to minimize the nonlinearity. With a thin (f = 1m) focusing mirror, as much as 60% of the input pulse can be transmitted through the 90 cm long capillary [35]. The importance of using the noble gas is due to the following facts: (1) the nonlinearity strength can be controlled by changing gas pressure; (2) argon has high threshold intensity for multi-photon ionization.

3.3.1 Self phase modulation (nonlinear phase shift) in fiber

The Kerr nonlinearity of argon imposes self phase modulation (SPM) on the pulse propagating down the waveguide. The refractive index of the medium is no longer independent of the intensity of the light. The intensity of the Gaussian beam is a function of time and can be expressed as

$$I(t) = I_o \exp(-4 \ln t^2 / \tau^2) \tag{3.1}$$

where τ is the FWHM length of the pulse. At the high intensities, the refractive index of the medium changes with the intensity of a pulse. The leading and trailing edges of a pulse where the intensities are comparatively low, show less change in the index of refraction according to the relation

$$n(t) = n_o + n_2 I(t) . \tag{3.2}$$

The nonlinear refractive index n_2 is recognized as a source of new frequency components during the propagation of an intense light through a Kerr medium. The values of the nonlinear refractive

indices of air and fused silica are 5.0 $\times 10^{-19}$ cm^2/W and 3.2 $\times 10^{-16}$ cm^2/W respectively. The time-dependent nonlinearly induced phase shift,

$$\Delta\varphi(t) = -\frac{2\pi}{\lambda_0} n_2 I(t) L, \tag{3.3}$$

where $I(t)$ is the time dependent intensity and L is the propagation length, manifests itself as a self phase modulation and tends to broaden the spectrum [36]. The chirp or frequency sweep of a pulse is given by the time derivative of the phase shift

$$\frac{d\Delta\varphi}{dt} = -\frac{2\pi}{\lambda_o} n_2 L \frac{dI(t)}{dt} \tag{3.4}$$

Therefore the leading edge of the pulse is red shifted whereas the trailing shows blue shift. Getting a large initial chirp is a necessary and important condition for producing shorter pulses. Thus the SPM in a hollow core fiber produces positively chirped pulses. And only a chirped pulse can be compressed by group velocity dispersion (GVD) of material with length l_m expressed as

$$GVD(\varphi'') = \frac{\lambda^3 l_m}{2\pi c^2} \frac{d^2 n(\lambda)}{d\lambda^2} \tag{3.5}$$

The GVD of the material is measured in units of fs^2.

The compensation of a positively chirped pulse is achieved with the dispersion compensation mirror or broadband chirped mirror [36]. These mirrors are constructed in such a way that the thickness of the layers of the multilayer coating varies continuously. The wavelengths corresponding to the red light are reflected at more deeply lying layers close to the substrate .The blue light reflects closer to the front surface of the mirror. The number of necessary bounces in chirped mirrors for this study (Chapter 7) was estimated by accounting the total air distance (~3m, equivalent to 3mm of fused silica plate) from the output of the last chirped mirror to the reaction volume, the window (3mm) used in the COLTRIMS chamber, and other components of optics used in the setup. Sometimes a more negatively chirped pulse has to be compensated for by placing the proper thickness of fused silica windows in between the chirped mirror and the chamber. At 800nm, one reflection in the chirped mirror introduces a group velocity dispersion of -30fs^2. It can be compensated by 1mm thickness of fused silica. We have used about six reflections to compensate the total air distance and window of the chamber.

3.3.2 Pulse characterization and measurement

The basic principle behind all the procedures to measure a short pulse is to use the same pulse to scan itself. This includes all the autocorrelation measurements like FROG (frequency resolved optical gating) and SPIDER (spectral phase interferometry for direct electric-field reconstruction) [37]. The autocorrelation process involves the splitting of a pulse into two, delaying with respect to another with a delay arrangement, and finally spatially overlapping them into a nonlinear medium such as a Beta Barium Borate (BBO) crystal (second harmonic generation crystal) which produces light with double the input frequency. The output field at the crystal is given by

$$E_{SHG} \propto E(t)E(t-\tau) \tag{3.6}$$

where τ is the delay between the two separated pulses. The intensity at the output is proportional to the product of the intensities of the two pulses.

$$I_{SHG} \propto I(t)I(t-\tau) \tag{3.7}$$

The detector response of the signal is too slow to resolve in time, hence actual measurement consists of the time integral given by

$$A(\tau) = \int_{-\infty}^{\infty} I(t)I(t-\tau) \tag{3.8}$$

This is the necessary definition for an autocorrelation process. There will be no second harmonic intensity until the two pulses overlap in time. Thus the intensity of autocorrelation gives the pulse length. A relative delay of one pulse length will typically reduce the SHG intensity.

FROG involves operating in the time-frequency domain. Measurement in the time frequency domain involves both temporal and frequency resolution simultaneously. For detail of the operation and theory please see the reference [38].

3.4 TOPAS: Generation of wavelengths of laser different from fundamental

Most of the work presented in this thesis relates to the experiment conducted on the fundamental laser wavelength centered at 800nm. But in Chapter 4 on the single ionization of argon atoms, we have also used other different lower laser wavelengths, generated from the

fundamental, to ensure that the substructure in the ATI peaks in the lower energy portion of the electron spectra are attributed to Freeman resonances. We have employed the TOPAS [45] pumped by the output of the Ti:Sapphire multipass amplifier (790nm,35fs,1.5 mJ, 1KHz) to generate pulses in the range 580-1150 nm. The optical parametric amplification (OPA) output is frequency doubled in a nonlinear crystal (BBO) to generate pulse wavelengths below the fundamental. Figure 3.2 explains the working principle of OPA schematically.

TOPAS (traveling optical parametric amplification superfluorecence) consists of one stage of superfluorecence (SFL) generation and four light amplification amplifier stages arranged in a single BBO crystal. The SFL generator (first pass through the nonlinear crystal) serves as a

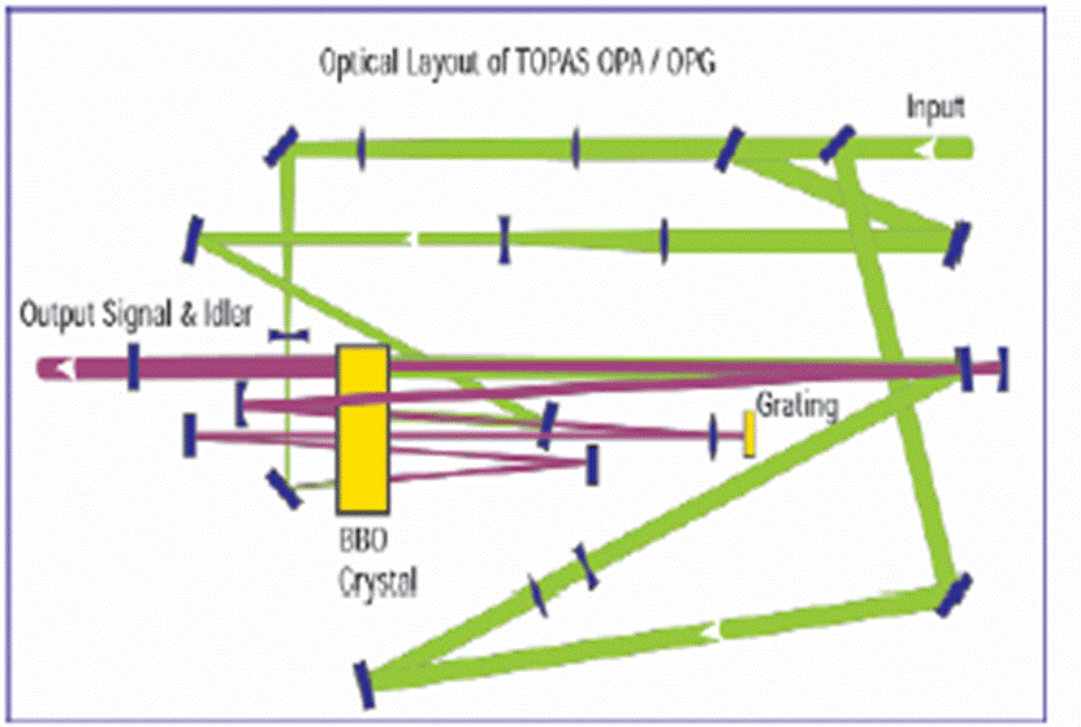

Figure 3.2: Schematic of optical parametric amplification optical layout. The first three passes through nonlinear crystal (BBO) in the system are used for the generation and the pre-amplification of the stable seed pulse for subsequent amplification stages. The fourth pass is used for the generation of stable, nearly transform limited, and low diffraction seed for the power amplifier. The seed beam that has been pre-amplified in the fourth pass will be amplified to its final power level in the 5th pass by using the bulk of the incoming beam. In order to have high energy conversion efficiency, the seed and pump pulses should overlap both in time and space (extracted from [39])

seeder emitting broadband superfluorecence. Preamplifiers (second and fourth passes through the nonlinear crystal) shape the beam acting as a small amplifying aperture placed in the far field of the seeder. In the third pass through the nonlinear crystal, the amplification usually is negligible. The last amplification stage (fifth pass though nonlinear crystal), which is usually pumped by the bulk of the available pump, boosts the energy of the parametric pulse. With a pump beam of high spatial coherence and a carefully adjusted pump beam size in the pre-amplification stages, TOPAS emits beam with divergence close to the diffraction limit.

3.5 COLTRIMS: Cold target recoil ion momentum spectroscopy

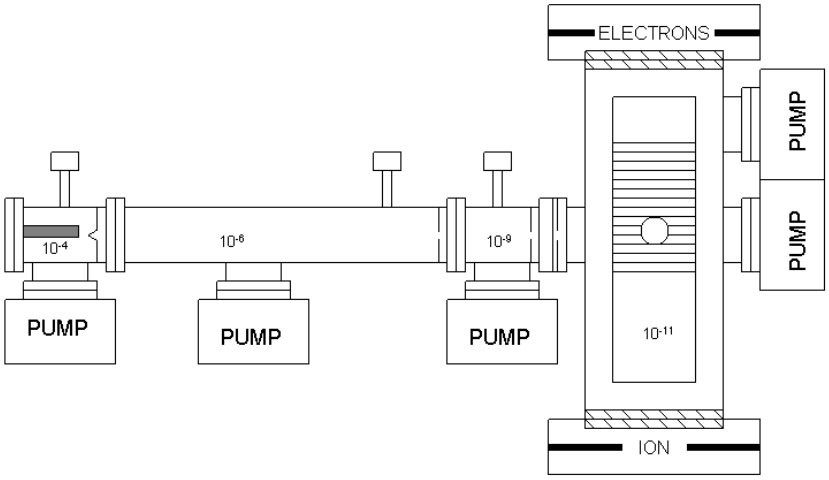

Figure 3.3: Schematic of COLTRIMS setup. It consists of five differential pumping stages with different base pressures maintained by turbo-molecular pumps backed by a roughing pumps in each stage. The main part of the setup is a highly evacuated chamber fitted with the spectrometer, and MCP, and position-sensitive detectors at each side of the chamber.

The word COLTRIMS stands for cold target recoil ion momentum spectroscopy. Historically, it was basically used for imaging the ion from the reaction products of ion and atom collisions. At the present time, the technique has been popular for detecting both ions and electrons from the interaction of both ion beams and photons with gaseous targets. Hence this approach is sometimes referred to as a reaction microscope. This technique can give us a broad picture of the reaction products in momentum space: capturing all aspects of the final state and providing bright, high resolution pictures of all the breakaway channels of atoms and molecules. The overview of the COLTRIMS system is shown in Figure 3.3.

Key advantages of using the COLTRIMS technique [40] are:

1. Kinematically complete experiments
2. 4π solid angle collection for ions and for low energy electrons
3. Ion and electron measurement with high resolution.

The COLTRIMS setup consists of the following main parts:

1. Gas jet
2. Ultrahigh vacuum chamber and differential pumping stages
3. Focusing mirror
4. Magnetic coils
5. Spectrometer
6. Detectors: (a) MCP; (b) Delay line detector

3.5.1 Gas jet

Providing a cold target is essential for the recoil ion momentum because the typical value of the momentum to be measured is of the order of or less than the thermal momentum spread of atoms or molecules at room temperature. A supersonic jet in the COLTRIMS setup requires, most importantly, a dense gas that is well localized and internally cold. In order to get the supersonic jet, the gas is allowed to expand from higher pressure (order of a few bars) into a high vacuum chamber through a nozzle (30 μm). The jet is made more directional and collimated by using a skimmer and two other slits before it reaches the interaction region in the chamber. The

first slit is fixed at the border between the second and third pumping stages, while the last one is an electrically controlled piezoelectric slit located just above the chamber.

To determine the jet velocity $V_{jet(atom)}$ let us consider the internal and the compression energy ($k_B T_o$) of a monatomic gas (inert gas) before expansion. The final kinetic energy of a partially supersonic jet (that depends upon the driving pressure and temperature before expansion) is found by summing these two energies:

$$\frac{1}{2} M_a V_{Jet(atom)}^2 = \frac{3}{2} k_B T_0 + k_B T_o = \frac{5}{2} k_B T_o , \tag{3.9}$$

where T_o is the temperature of the gas before expansion, M_a is the mass of an atomic particle and k_B is Boltzmann's constant ($1.38.10^{-23}$ JK^{-1}). Therefore the momentum of the gas particles in the jet direction after expansion through the nozzle can be found from the absolute temperature before expansion and the mass of a particle in the jet, as given

$$V_{Jet(atom)} = \sqrt{\frac{5 k_B T_o}{M_a}} \tag{3.10}$$

In general the final jet velocity [41] can be expressed as

$$V_{jet} = \sqrt{\left(\frac{\gamma}{\gamma - 1}\right) \frac{2 k_B}{M} T_0} \tag{3.11}$$

Table 3-1 γ parameter of different gases

Gas	γ
He, Ne, Ar	1.66
H_2,N_2,O_2	1.4
CO_2	1.3

where γ is the specific heat ratio $\frac{c_p}{c_v}$, and M is the mass of a gas particle of the jet. Typical values of γ for different target gases are shown in the table 3.1.

Consider the expansion of helium gas at room temperature (T_o=300K). Using equation (3.11), the momentum gained by helium after expansion is found to be equal to 5.9 a.u.; similarly for Ar, its value is 18.6 a.u. This corresponds to a velocity of 560 m/s. Thus the heavier the mass

of gas particles, the greater the momentum they have in the jet direction. The mass of an electron is 1836 times less than that of a proton. Thus the momentum spread of the electron due to the center-of-mass motion of its parent atom or molecule is negligible. The quality of a supersonic jet can be expressed by a quantity called the speed ratio [41] which is defined as the ratio of mean velocity to the thermal spread in velocities

$$S = \frac{V_{jet}}{V_{thermal}} = \sqrt{\left(\frac{\gamma}{1-\gamma}\right)\frac{T_o}{T}} \quad . \tag{3.12}$$

where T_o is the absolute temperature of gas before expansion and T is the internal temperature of gas after expansion. For an argon jet, the speed ratio is equal to

$$S = \sqrt{\frac{5}{2}\frac{T_o}{T}} \quad . \tag{3.13}$$

Knowing the speed ratio (S) and the temperature of the gas before expansion (T_o), the internal temperature of the jet (T) after supersonic expansion can be estimated by the above expression. The speed ratio (S) also depends on the gas species and the product of driving pressure, and nozzle diameter [40, 41]. In Figure 3.4, the COLTRIMS geometry is depicted in the rectangular co-ordinates system.

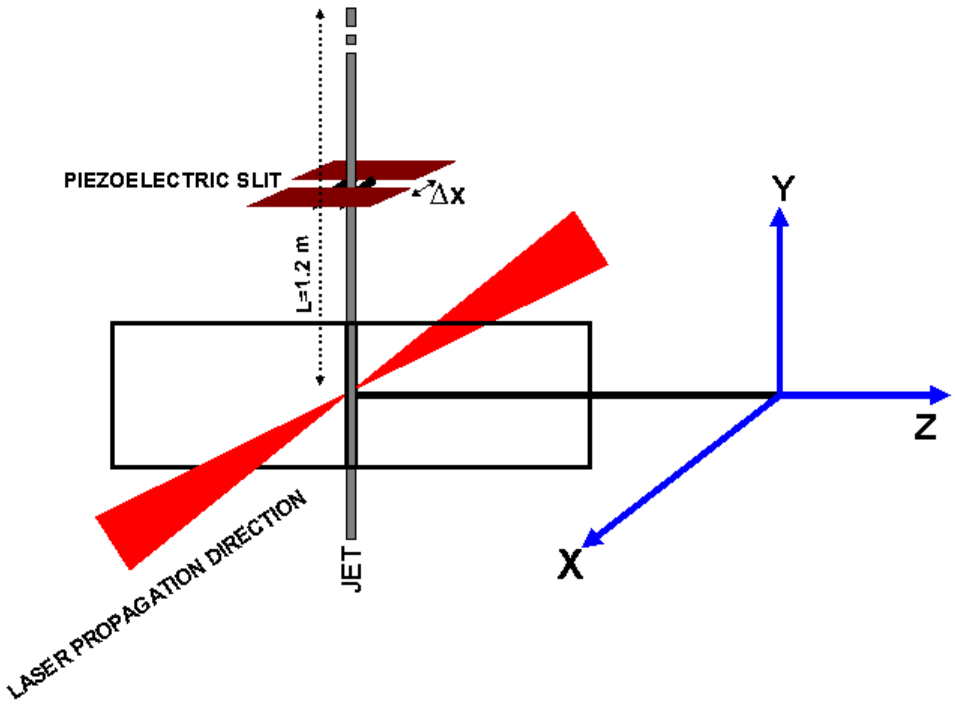

Figure 3.4:The coordinate system used in the COLTRIMS geometry. The X, Y and Z directions indicate the laser propagation, jet and detector axis (field).

Let us see how the momentum resolution is affected by the different types of jet parameters and other geometries including skimmer diameter.

The width of the momentum resolution in the jet direction is equal to the ratio of jet momentum to the speed ratio as expressed by

$$\Delta P_{jet} = \frac{\sqrt{5Mk_B T_o}}{S} = \sqrt{2Mk_B T} \qquad (3.14)$$

For example, an argon jet with driving pressure of 1 bar (14.5 psi) at room temperature (T_o=300K) has a speed ratio equal to 12.9 [42]. Then the momentum spread of argon is 1.4 a.u. If the driving pressure of the jet doubles (2 bar), the speed ratio increases. The width of the momentum resolution function is directly proportional to the square root of the temperature after expansion provided that the speed ratio remains fixed. In such a case the resolution can be much improved by pre-cooling of the gas.

Similarly the momentum width perpendicular to the jet direction is determined by taking account of several factors such as jet momentum, skimmer diameter, and skimmer nozzle distance. The momentum of argon in the jet direction is estimated as 18.6 a.u. at T_o= 300K and the skimmer diameter and skimmer nozzle distances in our setup are 30μm and 10mm respectively. Hence the momentum spread in the direction perpendicular to the jet is estimated to be 0.093 a.u., which is much smaller than the width in the jet direction. This is true only in the region just below the skimmer. The resolution is much better in the region (center of chamber or focus) at a distance 1.2 m from the nozzle where the angle subtended by the interaction size transverse to the jet motion is considerably smaller. The piezoelectric slit just above the center of the chamber can be used to control any desired size of jet varying from 2mm to 40 μm in the direction normal to the spectrometer axis. However, the width of the piezoelectric slit along the spectrometer axis remains the same (1.5 mm) for the whole time. The piezoelectric slit is closer to the chamber; basically the jet size at the focus is the same as the dimension of the slit.

The width of momentum along the spectrometer axis is given by

$$\Delta P_z = P\cos\theta\Delta\theta \tag{3.15}$$

This can be expressed in terms of the momentum of the jet as follows:

$$\Delta P_z = P_y\Delta\theta = P_{jet}\Delta\theta = \sqrt{5Mk_BT_o}\,\Delta\theta \tag{3.16}$$

If the size of the argon jet in the interaction region along the z-direction perpendicular to the jet is Δz =1.5 mm, then the momentum spread

$$\Delta P_Z = \sqrt{5Mk_BT_o}\,\frac{\Delta z}{L} = \frac{18.6(a.u.).1.5\times10^{-3}(m)}{1.2(m)} = 0.0231 a.u. \tag{3.17}$$

In general the focal size is much smaller than Δz, so the effective size of the interaction is much smaller than 1.5 mm. Therefore we expect much better resolution than that shown in equation (3.17).

Similarly the momentum resolution in x-direction can be estimated by the relation

$$\Delta P_X = \sqrt{5Mk_BT_0}\,\frac{\Delta x}{L}. \tag{3.18}$$

Thus the crucial factor for achieving higher resolution in the x-direction is the width of the slit (Δx) which controls the jet in that direction. Its size can be varied from 45μm to 2mm.

3.5.1.1 Collimation of jet

Figure 3.5 shows how different slits in the COLTRIMS system help to collimate the jet at the interaction region. Obviously, when a target jet exits the nozzle from higher pressure to lower pressure into the source chamber, it spreads out around the jet direction. The special arrangement of the skimmer (0.5 mm) followed by two more narrow slits (2mm) and one piezoelectric slit, not only keeps the jet cold but also helps to control the desired size of the jet as well as collimating the jet down to the chamber. The voltage controlled piezoelectric slit can change the size of the jet at the interaction region from 40 μm to 2mm in the laser beam direction.

The extremely thin jet provides two key advantages for a high intensity laser experiment. First, molecules or atoms can be confined almost entirely to the highest intensity of a tight laser focus (w_0~6μm). Second, owing to the ultrasmall interaction volume, it is possible to carry out the experiment on a single gas-phase experiment.

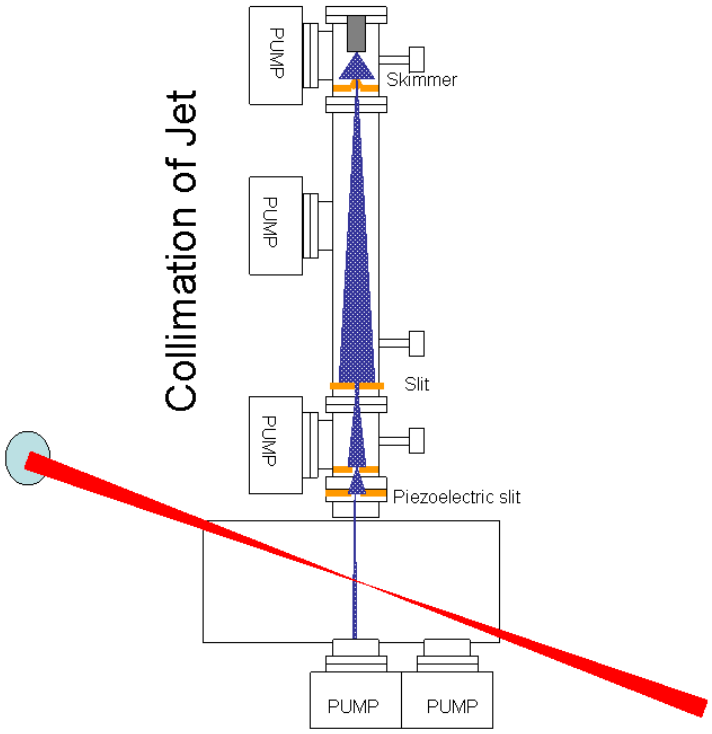

Figure 3.5: Jet collimation. Gas from a gas bottle expands through a very narrow nozzle into the high vacuum of source chamber. The skimmer position in between the source and first intermediate chamber cuts only the central portion of jet. The piezoelectric slit close to the detector chamber provides the final collimation.

3.5.1.2 Controlling the size of the jet with the piezoelectric slit

Strong field ionization is a highly nonlinear process. It is very worthwhile to resolve all the phenomena occurring in the focal volume according to the intensities. But the intensity varies over the spatial extent of the focus. It is in our interest to adjust the position of the jet so that it overlaps only at the central part of the focus. But in a real situation, the gas jet overlaps not only at the center portion of the focus but also with the consecutive shells around it where the intensity is lower. Moreover, these outer shells are larger in volume than the central part. In practice there is no easy solution in order to tackle this problem.

The voltage-controlled piezoelectric slit mounted just above the chamber in the present setup is the ultimate choice for collimating the jet at the center of the focus. The slit width can be changed into any desired value from 2mm to 45 μm by changing the potential difference of -15 V to 115 applied to the piezoelectric element. The voltage dependence of the slit width was calibrated by noting the different catcher pressures for different slit voltages. The calibrated value of the piezoelectric slit size was estimated to be 15μm/V. The high ratio of double to single ionization yield shown in the Figure 3.6 is the result of the ultrathin jet at the intense part of the focus and achieved by the narrow width of the piezoelectric slit.

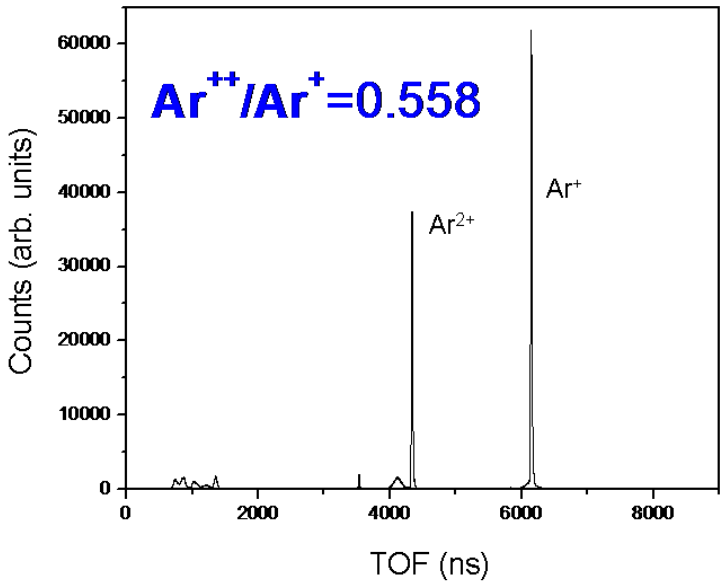

Figure 3.6: The time of flight of single and double ionization of argon in circular polarization. The high ratio of double to single ionization yield shown in the graph is the result of the ultrathin jet at the intense part of the focus and achieved by the narrow width of the piezoelectric slit. The size of jet for this particular experiment was ~40μm.

3.5.2 .Ultrahigh vacuum chambers and differential pumping stages

In the strong field process, a laser beam of high power is focused to a tiny volume inside the chamber, which gives rise to an intensity at the focus on the order of 10^{15} W/cm^2. The intensity at the focus is high enough that it can ionize almost everything there. Especially, this problem becomes more serious if the size of the jet is smaller than the focal size. Eventually, it will give more false events from background than real ones from the jet. Keeping this fact in mind, there is no alternative other than to make the vacuum as good as possible. But technically the possibility of achieving very high vacuum is limited by the efficiencies of the pumping

system. Having ultrahigh vacuum is especially crucial for an electron experiment since there is no way to identify whether the electrons are from the background or from the jet.

In the present COLTRIMS setup, the whole vacuum system has been separated into five stages: source chamber, two intermediate chambers, main chamber (detector chamber) and catcher. The first two are the differential pumping stages separated by a skimmer (0.5mm) and they are evacuated by turbo-molecular pumps with pumping speeds of 500 l/s and 100 l/s respectively, backed by roughing pumps. The base pressures in these stages are 10^{-7} and 10^{-8} torr, respectively. The two intermediate chambers are separated by a slit of diameter 2mm, and also are differentially pumped, (The pumping speed of turbo molecular pump connected to the third stage is 230 l/s). The third chamber is separated from the main chamber by an externally controlled piezoelectric slit. The base pressure of the each of the five chambers is monitored by using an ion gauge. Having taken care of all the necessary steps to maintain UHV, the base pressure in the chamber stays below 10^{-10} torr. All the residual gas of the jet after interaction with the laser beam will be collected by a catcher pumped with another turbo-pump (speed 230 l/s). Each turbo-molecular pump is connected to the roughing pump by a pneumatic gate valve. There is a high speed valve (MDC Vacuum Products Corporation, Model # GV-4000M-P) located between the main and intermediate chambers. The valve is used occasionally while opening either the upper or lower part of the chamber during maintenance work. Closing the valve during the work isolates the upper three from the detector chamber. Regular monitoring and proper maintenance of the system are very important in order to avoid the failure of any parts of the system due to power outages and other mechanical problems.

Water and hydrogen are known as the main contaminants of ultrahigh vacuum systems. Water bonds strongly to the walls of the chamber and can be removed partially by baking the chamber for a few days at a temperature around 250^{o}F while still pumping. However, some water always remains on the walls and continually outgases into the system. Hydrogen is more difficult to extract because it diffuses into the chamber walls. Even turbo-molecular pumps are not efficient to pump the hydrogen out of the chamber. Activating non-evaporable getter (NEG) pumps during the baking time helps greatly to extract the hydrogen from the chamber. They can help to provide a better ultimate vacuum than is achievable without them. The hydrogen molecules that land on the surface of the getter material break up into two atoms and diffuse into the bulk of the getter, forming a solid.

3.5.3 Focusing mirror

One of the main advantages of doing the optical field ionization experiment is the ability to concentrate the energy of a pulse in a tiny region by optical means such as using a lens or a mirror. In order to avoid the increase in pulse length in dispersive media using a lens, we use a parabolic mirror inside the chamber to focus the laser beam at the jet. The peak intensity at the focus is an inverse function of the size of the focus which in turn depends on the focal length of the mirror used. A smaller focal length of the mirror gives a smaller size of the focus. This gives rise to higher intensity. This is the basic principle behind the use of a smaller focal length (7.5cm) parabolic mirror in this experiment.

For example, the cycle averaged peak intensity (I_o) of a laser pulse at the focus of the given mirror is given by

$$I_o = \frac{P}{\pi \omega_o^{\,2} \tau R} \tag{3.19}$$

where P is the measured time averaged power, τ is the duration of the pulse, and R is the repetition rate of the laser. For a Gaussian beam the focal radius (ω_o) is directly related to the focal length of the given mirror by

$$\omega_0 = \frac{f\lambda}{\pi\omega} \quad . \tag{3.20}$$

Therefore the shorter the focal length of the given mirror, the smaller the size of focus it produces. As a result, high peak intensity can be easily achieved with low pulse energy.

For the typical beam radius, ω = 3mm, the size of focus is calculated as

$$\omega_0 = \frac{f\lambda}{\pi\omega} = \frac{7.5\times10^{-2}(m)\times800\times10^{-9}(m)}{\pi\times3\times10^{-3}(m)} = 6.37\mu m \tag{3.21}$$

Thus, it produces a focal spot of diameter 6.37μm, and it is completely overlapped by the jet, which is a favorable condition for achieving a higher signal-to-noise ratio. Furthermore, the advantage of using a parabolic over a spherical mirror is that it is free from the problem created by spherical aberration. Figure 3.7 shows the overlapping of the focused laser beam with the jet.

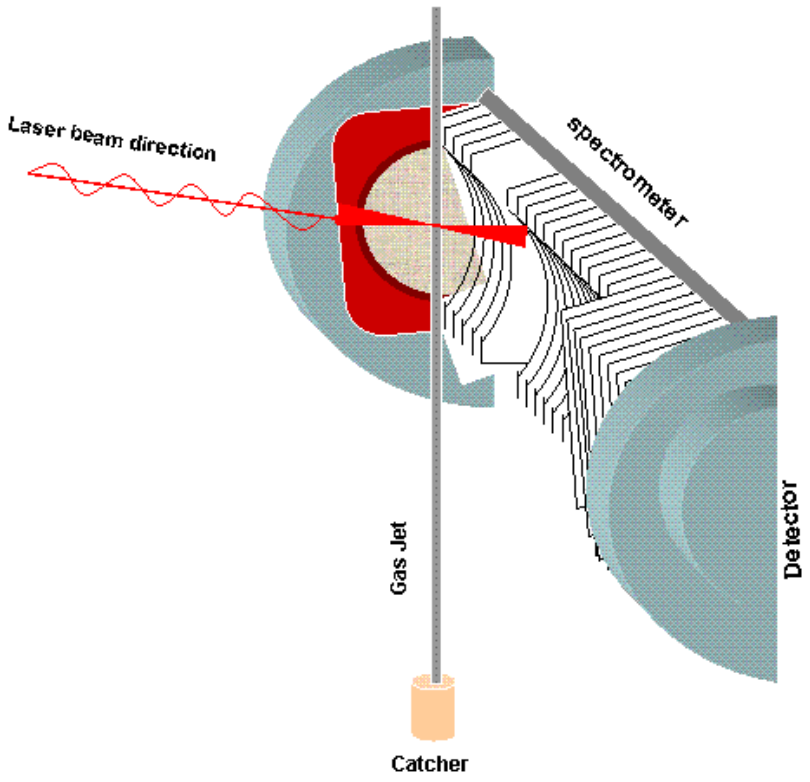

Figure 3.7: The overlapping of the focused laser beam back reflected by a parabolic mirror with the supersonic jet inside the UHV chamber housing the spectrometer and detectors.

The mirror is positioned in a metallic holder just behind the interaction region of (a wide gap in) the spectrometer. The position of the mirror can be adjusted into three mutually perpendicular directions by an XYZ translation manipulator until the back reflected laser focuses on the target jet. Noting the number of counts with and without the jet, the exact position of the focused laser on the jet can be tuned.

3.5.4 Magnetic coils

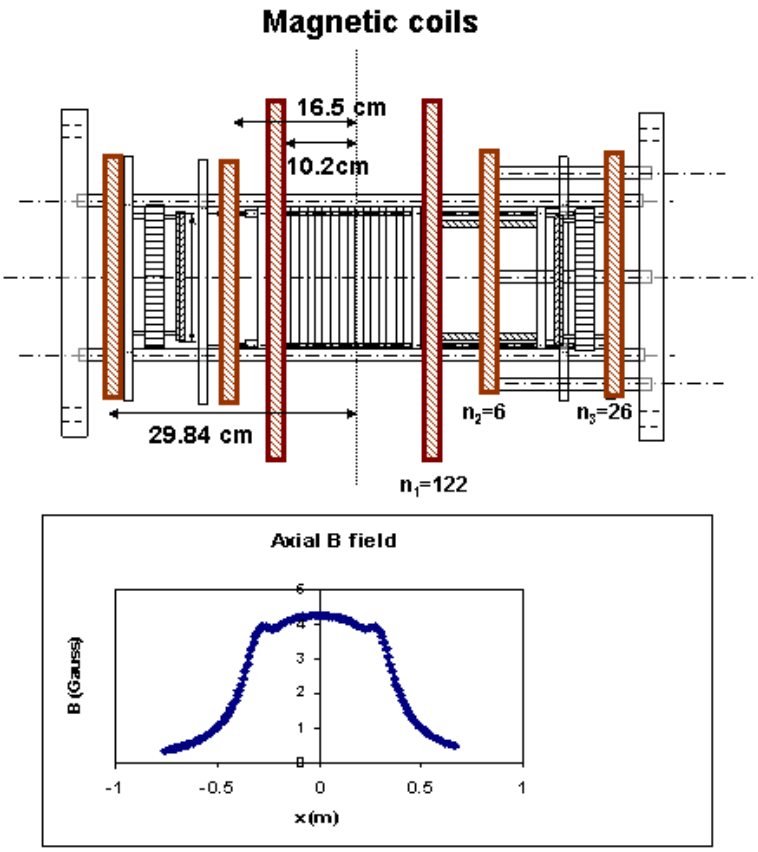

Figure 3.8: The position of the three pairs of magnetic coils over the COLTRIMS chambers which are used for driving the transverse electrons towards the detector. The larger pair is for the main source of the B field and the smaller pairs are for the correcting field. The radii of the two larger coils and four smaller coils are 33.0 cm, and 10.16 cm, respectively. The number of copper wire turns in each larger is 122. The number of turns in the smaller coils closer to the larger one is 6 and other pairs of coils close to the end of chamber is 26 as shown in figure 3.8. The graphical plot shows the axial B field produced by the combined coils in the spectrometer with a current of 1A pasing though them.

The electrons born in the interaction region can move all possible directions with energies ranging from a few electron volts to higher values depending on the laser intensity. The electrons with higher energies can reach the detector easily if their initial velocity is directed toward the detector even without having any driving field. Low energy electrons can be collected with the extraction field in the spectrometer. The purpose of applying a homogenous magnetic field along the flight path superimposed to the electric field is to increase the acceptance angle of

the electrons whose initial velocities are directed transverse to the spectrometer axis. Two large coils with the Helmholtz (the two coils are separated by a distance equal to the radius of the coil) arrangement are often used for this purpose. But in our current setup, we have used a different arrangement which consists of one pair of large coils for producing the B field and two extra pairs of smaller coils to correct the field along the spectrometer axis as shown in Figure 3.8.
The magnetic field along the axis of this coil at any point x is given by

$$B = \frac{\mu_o nI}{2} a^2 \left(\frac{1}{\left(a^2 + (r+x)^2\right)^{\frac{3}{2}}} + \frac{1}{\left(a^2 + (r-x)^2\right)^{\frac{3}{2}}} \right) \tag{3.22}$$

where a , n and r are the radius of coil, number of copper wire turns of each coil of a pair and separation between two coils respectively. I is the current through the coils. μ_o is the permeability constant ($\mu_o = 4\pi \times 10^{-7}$ Tm/A)

3. 5. 5 Spectrometer

The purpose of the spectrometer is to guide the electrons and ions onto position sensitive detectors. The spectrometer consists of a series of copper plates of the same size and with holes at the middle, parallel to the interaction volume and detector center as shown in Figure 3.9. Two consecutive plates of the spectrometer are connected with resistors and separated by a very narrow gap to avoid the fringe fields. The electric field region of the spectrometer is separated by two 80% transmission grids. Thus, applying a potential difference over this structure (arrangement) generates a homogeneous field inside the spectrometer. A homogeneous electric field is produced within the spectrometer by uniformly decreasing the potential of each electrode from left to right. This is achieved using the voltage divider scheme in which adjacent electrodes are connected in series by a single ultrahigh vacuum-compatible 100kΩ resistor.

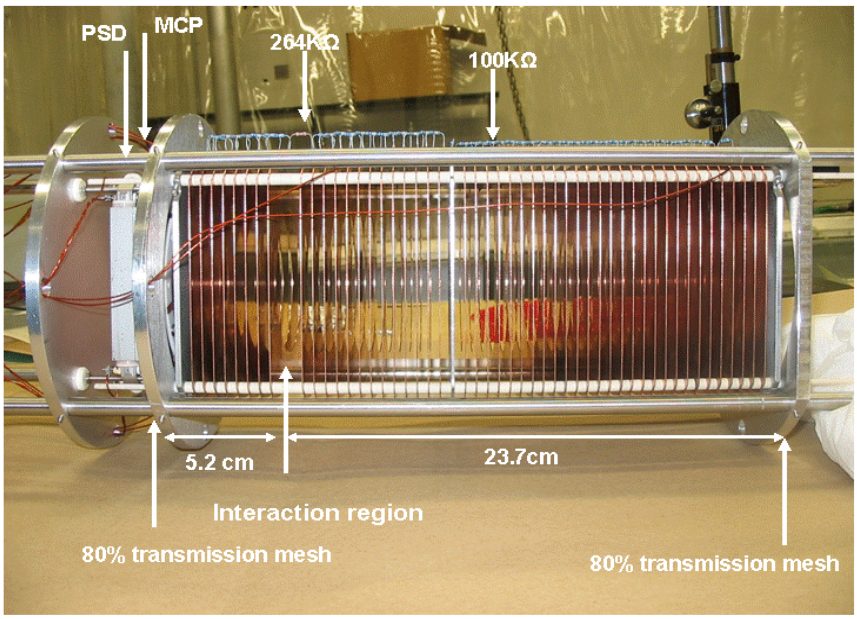

Figure 3.9 : The spectrometer with MCP and position sensitive detector in the left end. The spectrometer consists of a series of copper plates, and every two consecutive plates are separated by a gap with a resistor of 100KΩ. The gap at the interaction region is three times larger than the other gaps with resistor 264 kΩ. There are 8 copper plates (electrodes) on the left and 42 on the right side of the interaction region. The two detectors are on each side are separated from the field region by 80% transmission grids (meshes).

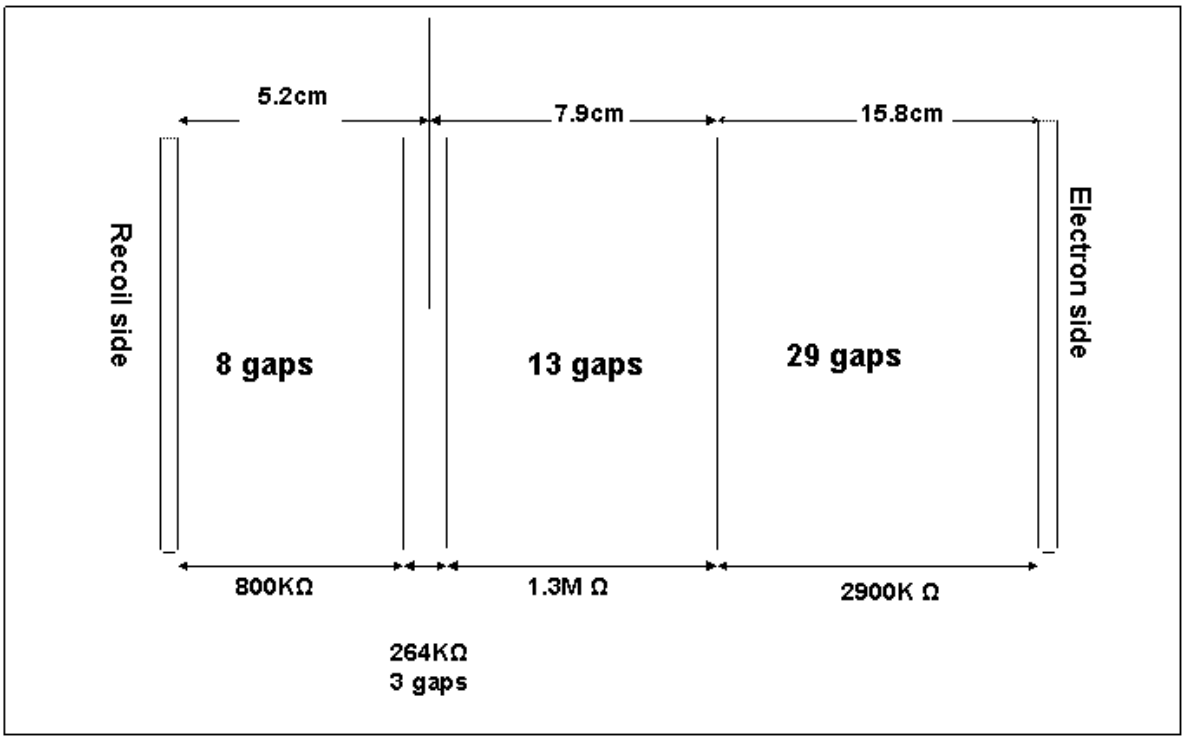

Figure 3.10: The length of the ion and electron spectrometer arms from the interaction region with the value of resistance connected to each gap of spectrometer arm.

3. 5. 6 Multihit detectors: MCP and PSD

The detector assembly consists of two detectors, each of which is made up of a microchannel plate (MCP) and a position sensitive detector (PSD) located at approximately 5 and 24 cm away from the interaction regions. The longer distance was chosen as the electron flight path in order to maximize the resolution.

3. 5. 6. 1 Microchannel plates (MCP)

The main purpose of using the microchannel plate in the detecting system is to amplify the charge of the impacting particle to a level such that it can be measured electronically. The

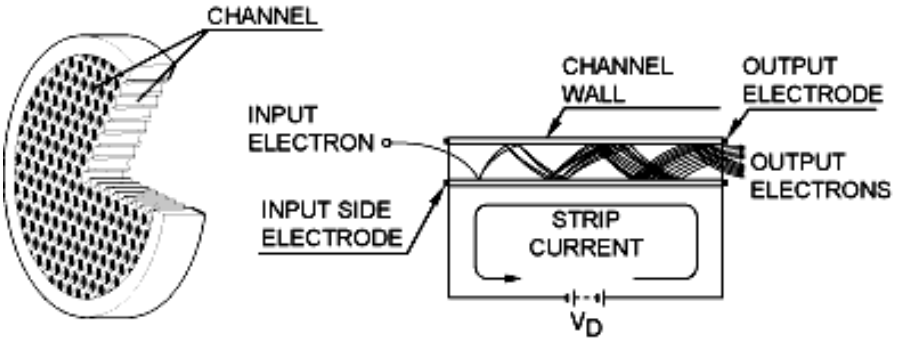

(a)

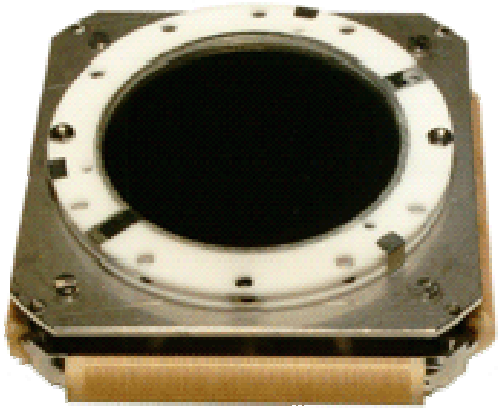

(b)

Figure 3.11: (a) Illustration of the structure and working principle of micro channel plates; (b) a real picture of the MCP used in our setup. An MCP is a specially fabricated plate that amplifies the electron signal similar to a secondary electron multiplier (SEM). An MCP has several million independent channels and each channel works as an independent electron multiplier. The MCP consists of a two-dimensional periodic array of very small diameter glass capillaries (channels) fused together and sliced in a thin plate. A single incident particle (ion, electron) enters a channel and emits an electron from the channel wall. Secondary electrons are accelerated by an electric field developed by a voltage applied across both ends of the MCP. They travel along their parabolic trajectories until they in turn strike the channel surface, thus producing more secondary electrons. This process is repeated many times along the channel; as a result, this cascade process yields a cloud of several thousand electrons, which emerge from the rear of the plate. If two MCPs are operated in series, a single input particle can generate a pulse of 10^8 or more electrons at the output [43, 44]

two MCPs of active diameter 8cm are positioned on each side of the UV chamber. A microchannel plate is an array of miniature electron multipliers oriented parallel to one another as shown in Figure 3.11. Both of them are assembled in chevron configuration (V-shaped). The channel axes are typically normal to biased at a small angle (~8^{o}) to the normal to the MCP input surface. The advantage of such a configuration is that it guarantees that the incoming particle hits the wall of the channel due to the channel being at an angle to the plates and thus the angle of impact. The impact starts a cascade of electrons that propagates through the channel, which amplifies the original signal by several orders of magnitude depending on the electric field strength.

3. 5. 6. 1. 1 Biasing the ion detector

The front part of the MCP detector on the ion side is biased with 2.1 kV negative potential and the back is at ground. The electrodes (transmission grids) at the ends of the spectrometer were maintained at a negative voltage, typically -30V to -1500V depending on the type of fragments to be detected. The other end of the spectrometer, near the electron detector, was grounded. The overview of the biasing scheme is shown in Figure 3.36. The ions emerging from the spectrometer undergo a brief post-acceleration before impinging upon the detector. These primary electrons emit the secondary electrons on the way to the MCP.

3. 5. 6. 1. 2 Detection of ions

All the ions created in the reaction volume (or focus of mirror) see the negative voltage at the end of the spectrometer close to the ion detector. Recoil ions (atomic ions) have typically such low energy that they can be efficiently collected by a weak electrostatic field. Unlike the ions created by neutral atoms, the fragments produced by the Coulomb explosion channel are comparatively higher in energy and momentum. The ions which are directed towards the detector can be collected even with a low extraction field, but their counterparts cannot be pulled to the ion detector without having a sufficiently high extraction field. In addition to the initial energies, the ions also gain enough extra energy during their flight time in the electrostatic field of the spectrometer to be able to generate plenty of electrons on the front MCP detector provided with a

negative high potential (-2.1KV) with respect to the back of the MCP stack. Each MCP was connected to the power supplies via a load resistor. Therefore, each particle starting an avalanche caused voltage drops over the resistor which could be used to measure the particle's time of arrival on the detector (stop time). The timing signal is taken from this center of ring through the signal-pick-up box as shown in Figure 8.5 B (Appendix B). The potentiometer of this device can be used to adjust the impedance, which helps to minimize reflections of the fast timing signal due to impedance mismatch. After amplification by an Ortec VT120B fast preamplifier, the signal amplitude was about 2V and signal rise time was ~4 ns. The noise level was less than 300mV.

3. 5. 6. 1. 3 Biasing the electron detector

The experiments related to the angular correlation and low energy structure of an electron were carried out with an electron detector consisting of the two MCPs in a chevron configuration and with a delay-line anode. But all data of the alignment experiments were taken on the modified MCP detector. Due to the resistance mismatch between front and back parts of the MCP, we have separated the two MCP by a middle layer electrode. Before the modification, the front and back MCP were biased as a single unit with zero and positive 2.1 kV.

3. 5. 6. 1. 4 Detection of electron

Electrons are the more energetic particles because of their small mass. The electron momenta are mostly directed preferentially in the direction of the polarization of the laser. But there is some probability that some electrons are initially directed perpendicular to the polarization direction with energy ranging from zero to higher kinetic energies depending upon the electric field of the pulse. The COLTRIMS technique is even suited for collecting electrons with zero to ultralow energy. The spectrometer has higher collection efficiency for electrons moving towards the electron detector. For a typical application, applying the extraction field 1V/cm over the spectrometer we can collect up to 5eV electrons traveling opposite to the electron detector side in our current geometry as shown in Figure 3.12.

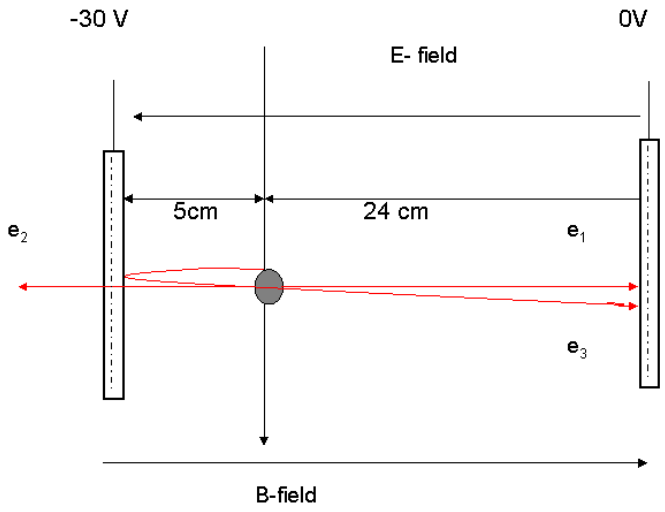

Figure 3.12: Illustration of the collection of longitudinal electrons by an electron detector guided by the spectrometer field. The figure shows the three different types of electrons moving in different directions: the one that is moving towards the detector can be collected by the field easily; the second is a low energy electron (below 5 eV) moving away from the electron detector but is reflected back to the electron detector, and the third one has higher energy (more than 5eV) and can pass the electrode near the ion detector, and never returns to the electron detector.

For a 30V potential across the spectrometer, the retarding potential experienced by an electron at the grid at the end of the ion spectrometer arm is calculated as

$$V = -\frac{5(cm)}{29(cm)} \times 30(V) = -5.17V \qquad (3.23)$$

The maximum energy needed for an electron to overcome this potential is thus 5.17 eV. Therefore all the electrons having initial energies equal to and below 5.17 eV will be retarded (reflected) from the electrodes of the ion side at this particular spectrometer voltage. However, if the energies of the electrons are more than 5.17eV, they will never come back to the electron detector. But this consideration is not important at higher spectrometer fields and also does not apply to the electrons emitted toward the electron detector. Therefore longitudinal electrons can be collected best by just applying the electric field. Moreover, the electrons which move

transverse to the time of flight direction can be diverted back to the detector by applying a uniform magnetic field superimposed on the electric field of the spectrometer. We have used the three pairs of circular coils with different numbers of turns to generate a quasi-uniform magnetic field along the axis of the detector. The electron motion in the spectrometer consists of a cyclotron motion in the detector plane (x-y plane) perpendicular to the spectrometer's symmetry axis and fields as shown in Figure 3.13, and uniform acceleration followed by the drift along that axis (z-axis). The cyclotron radius of an electron with the energy E_e is given by

$$r_c = \frac{\sqrt{2m_e E_e}}{eB} \quad , \tag{3.24}$$

$$r_c.10^{-2}(cm) = \frac{\sqrt{2.9\times1\times10^{-31}\times1.6\times10^{-19}E_e(eV)}}{1.6\times10^{-19}\times10^{-4}.B(G)}, \tag{3.25}$$

$$r_c(cm) = 3.37\frac{\sqrt{E_e(eV)}}{B(G)}. \tag{3.26}$$

Obviously, the last expression gives a much easier way to calculate the magnetic field required to divert the transverse electron into the electron detector and vice versa. For example if we want to collect the transverse electrons with initial energies up to 5eV, the necessary magnetic field can be found by using the equation:

$$B(G) = 3.37\frac{\sqrt{E_e(eV)}}{r_c(cm)} = 3.37\frac{\sqrt{5(eV)}}{2(cm)} = 3.76\ G, \tag{3.27}$$

where we have taken r = 2cm to ensure that all the electrons within that range (0-5 eV) strike the detector. In such a case we must have

$$R_{\det ector}(4cm) > 2r_c \tag{3.28}$$

The distance of electron (r_e) from its starting point at time t_e in the x-y plane is given by:

$$r_e = r_c\sqrt{2\left(1-\cos\left(\frac{2\pi t_e}{t_c}\right)\right)} \tag{3.29}$$

where t_c is the cyclotron period,

$$t_c = \frac{2\pi m_e}{eB} \tag{3.30}$$

or

$$t_c(ns)\times 10^{-9} = \frac{2\pi \times 9.1\times 10^{-31}}{1.6\times 10^{-19}\times 10^{-4} B(G)}, \tag{3.31}$$

$$t_c(ns) = \frac{358}{B(G)} \tag{3.32}$$

If B = 4G, then t_c = 89.5 ns

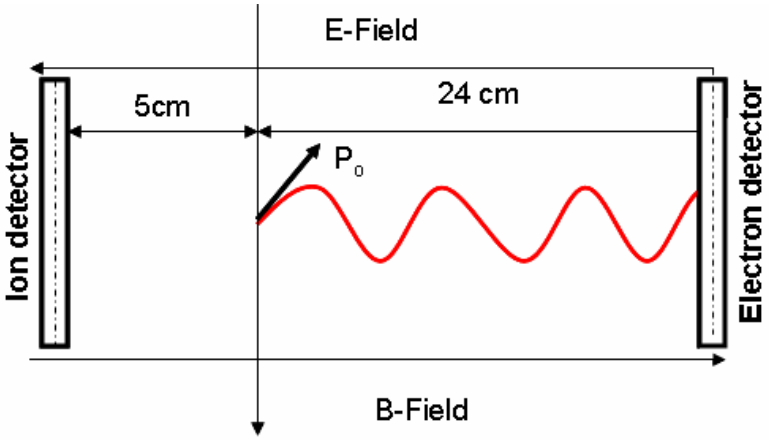

Figure 3.13: The schematic of the electron motion in the superposition of the electric and the magnetic fields.

3. 5. 6. 2 Delay line detector (position sensitive detectors)

The timing information of the particle to be detected is obtained by the MCP and the x and y positions of the particle read out by the delay line detector at the back of the MCP. The position sensitive detectors of both detectors in this experiment are RoentDek 80mm delay line detectors. The delay lines are made up of double spiral wire wound on the frame of ceramics and aluminum. The wire which is called the signal is maintained more positive (+50V) than the other (reference). Only the signal wire gets an electron signal while both the wires get capacitively coupled electronic noise. Later these signals are processed by a differential amplifier. In the differential amplifier (KSU EDL DLA800), the signals on the reference wire are subtracted from those on the signal wire, eliminating electronic noise induced in the wires. The signal- and

reference- wires are kept close to each other to make sure that both of them pick up the same electric noise. Pulses arriving at each of the ends are amplified and discriminated, before being clocked using a time-to-digital converter.

The principle behind the delay-line technique is to take advantage of the delay that a signal experiences when traveling on a transmission line. A signal induced somewhere on the delay line will propagate in both directions towards the ends. The position of the particle can be found by measuring the time difference between the signals arriving on the two ends of the transmission line for their respective direction. A second delay line structure over the first is to have two-dimensional imaging of the position of impact that also shares part of the electron cloud from the MCP. If l_1 and l_2 are the distances to the ends of the wires from the hit, the arrival times t_1 and t_2 in the x and y directions as shown in Figure 3.14 are written as:

$$t_{x1} = \frac{l_{x1}}{v}, t_{x2} = \frac{l_{x2}}{v} \tag{3.33}$$

$$t_{y1} = \frac{l_{y1}}{v}, t_{y2} = \frac{l_{y2}}{v} \tag{3.34}$$

where t_{x1}, t_{x2}, t_{y1} and t_{y2} are the timing signals from the four corners of the square PSD detector. And v is the transverse velocity of signal across the transmission wires and is approximately equal to 1mm/ns and this velocity is different from the signal velocity in the wires which is equal to the velocity of light ($c = 3\times10^8$ m/s)

For each dimension the respective position of the particle is directly proportional to the time difference t_1 - t_2 where t_1 and t_2 are the arrival times at the two ends of the line measured respective to a time zero, and can be expressed as

$$X = g_x(t_{x1} - t_{x2}) \tag{3.35}$$

$$Y = g_y(t_{y1} - t_{y2}) \tag{3.36}$$

where g_x and g_y are the conversion factors for changing the timing (ns) signal into the position (mm) expressed in units of mm/ns.

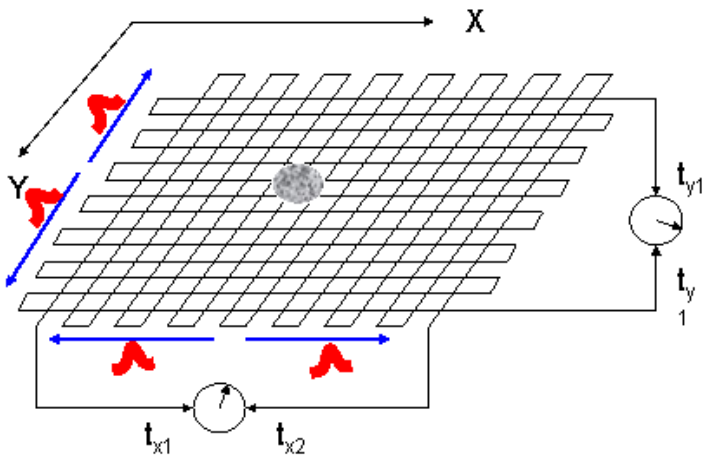

Figure 3.14: Illustration of the working principle of the position sensitive detector

3.5. 6. 3 Time sum

The time sum is defined in order to extract information about the hit position from the delay lines. The sum of arrival times of the signal at respective ends of the transmission line is constant for all positions irrespective of the particle hitting at different parts of the MCP. Therefore

$$t_1+t_2 = \text{constant (with respect to time zero)} \qquad (3.37)$$

The time of the occurrence of the signal on each wire (arrival time) is measured relative to the event signal from the MCPs.

$$t_1+t_2 - 2t_{mcp}= \text{time sum} \tag{3.38}$$

The time sum above is defined with respect to the time of the particle hitting on the MCP stack, and equals the propagation time for the whole length of the transmission line. This is true only if both signals from the ends of the line belong to the same hit. Potentially, there are two signals available on both wire ends per particle. With the additional MCP start signal, two time-sum values per particle can be calculated.

$$t_{sumx} = t_{x1} + t_{x2} - 2t_{mcp} \tag{3.39}$$

$$t_{sumy} = t_{y1} + t_{y2} - 2t_{mcp} \tag{3.40}$$

Particularly in our case, the time sum of each detector is around 80 ns with little difference for x and y position. The x and y transmission lines are wound one above another thereby making one line longer than other. This is the reason why there is a slight difference in the observed time sum in two perpendicular directions. Checking the signals against the time sum condition helps greatly in assigning the proper values of the position coordinates to the corresponding time of flight and to minimize the signal due to noise.

3. 5. 6. 4 Pulse-pair dead time

The pulse-pair dead time will define the actual limit in the multi-hit operability of a detection system. Each signal produced from a single charge cloud is picked up from the four anode contacts and from the MCP contact. The current read-out technique (the RoentDek detectors) with analog timing electronic front-end circuits detecting the pulse arrival times introduce a pulse-pair dead time of ~15ns. If the pulse-pair distance is greater than the dead time and time sum, only one particle's signal propagates on the delay line at a time. For example if two electrons consecutively hit the detector with time separation more than 80ns then only one electron's signal propagates on the delay line at a time. Thus the signals from two electrons will be collected in the same order as they arrive at the detector. If two electrons hit the detector within this period only one time-of-flight signal will be recorded, and at the same time it will give the uncertainty of the position information of the second electron. The pulse-pair dead time is translated directly to the z- component of momentum as shown in Figure 3.15.

From the time of the occurrence of the signal on each wire (arrival time) measured relative to the event signal from the MCPs, the x- and y-position can be determined.

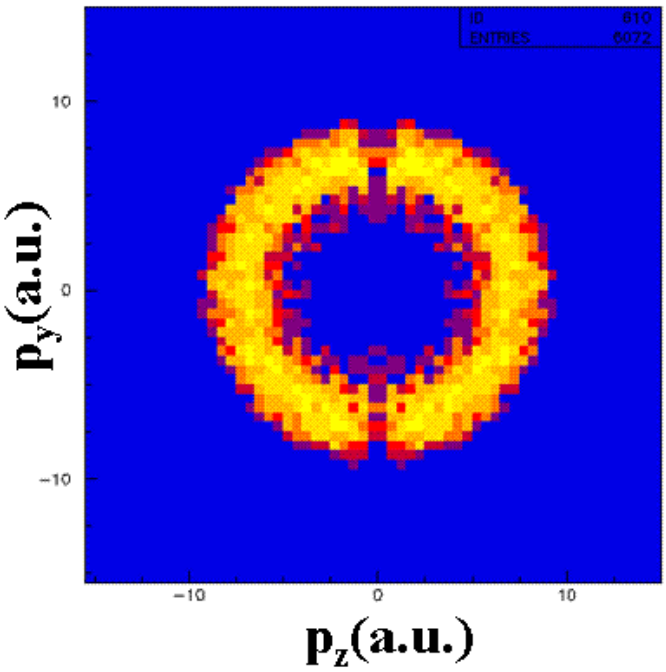

Figure 3.15: The y-z momentum slice of the Coulomb explosion of hydrogen molecules in circularly polarized light. The gap in the spectrum is the result of the limitation of the pulse-pair resolution.

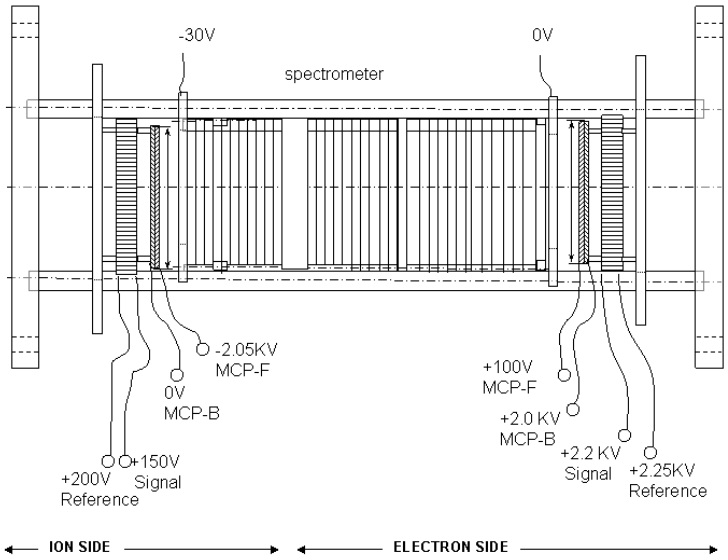

Figure 3.16: Illustration of the overall view of the biasing of the spectrometer, the electron and the ion detector. The two electrodes at the end of the spectrometer closer to the ion and the electron detector are maintained at negative potential and zero in order to accelerate the ion and electron into the respective detectors. The ion detector consists of MCPs in chevron configuration and PSD. The front and back of the MCP are maintained at -2.05 kV and 0 V which provides the necessary accelerating field for cascading the secondary emission of the incident particle in the MCP. The electron shower exits the back of the MCP stack and is accelerated towards the anode which is held at a positive potential with respect to the back MCP. The signal and reference transmission lines of the position sensitive detector are given +150 V and +200 V respectively. The signal wire is given +50 V more than the reference wire to make sure that the signal wire collects real signal and noise, and the reference wire will get only noise. The same principle applies to the electron detector also. In this case the signal starts in the MCP with the incident of an electron in front of the MCP stack.

3.6 Data acquisition

A block diagram overall view of the data acquisition system is shown in Figure 3.17. The key components of the present setup, which determines the dead time and timing resolution of the particles to be detected, are constant fraction discriminators (CFD), time-to-digital converters (TDC) and an analog-to-digital converter (ADC).

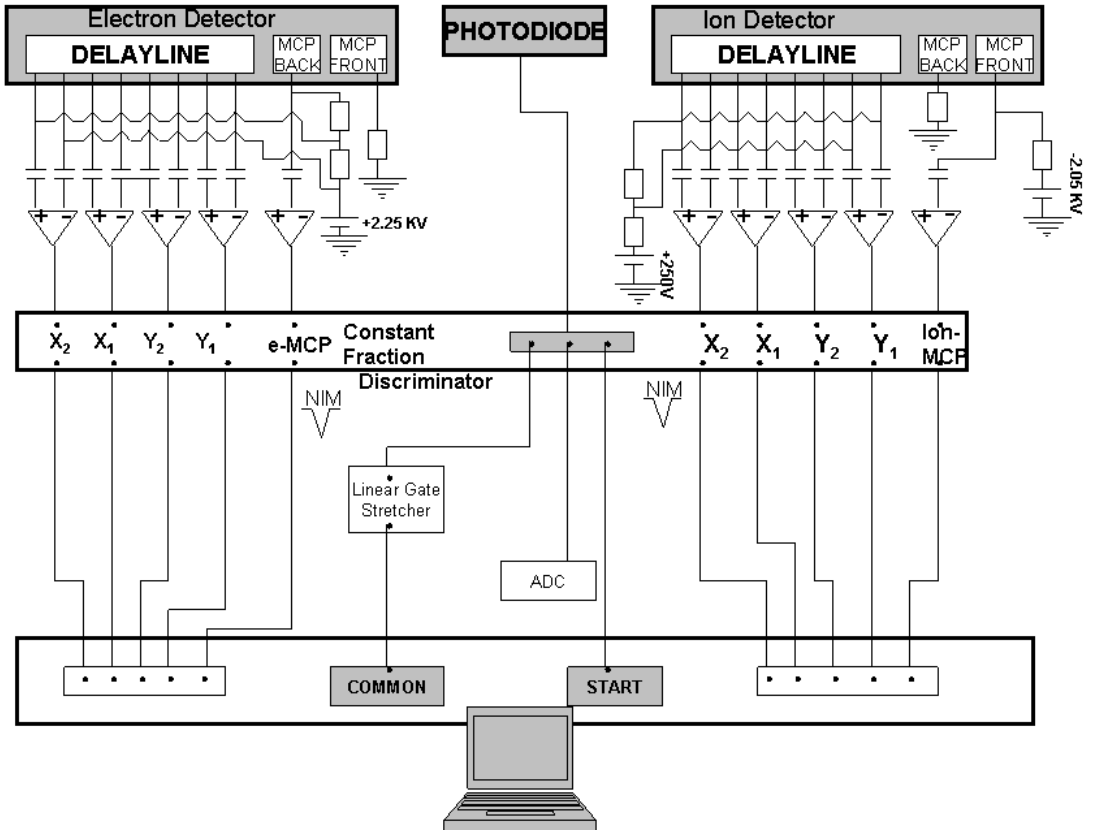

Figure 3.17: The overall view of the signal decoupling, signal processing and data acquisition electronics used in the experiment.

The system is initialized with the detection of a laser signal (start signal) by a photodiode. The signal detected by a photodiode, after being inverted (Ortec inverting transformer IT 100) and amplified (if necessary by a timing-filter amplifier), is sent to a constant fraction discriminator (Ortec 934 quad) for accurate timing and digitization. The three different output signals of CFD of the input signal from the photodiode are fed to the three channels of the TDC as follows:

(1) TDC 'COMMON' via Logic Fan-in/Fan-out and modified linear gate stretcher which set the time window that depends upon the mass and charge state of particle to be detected.

(2) TDC as BUNCH MARKER. This signal defines the START in order to convert the MCP signal into a time-of-flight signal.

(3) ADC (AD 811) 'STROBE' which triggers the CAMAC signal and enables the data to be transferred to computer.

The timing (amplified by fast amplifier ORTEC VT120) and position (amplified by delay line amplifier DLA800 EDL) signals from the electron and ion detectors are fed into the ten channels of a TDC (LeCroy 3377) via the CFD. The CFD produces the negative logic signal (NIM) of the width (~10ns) of each timing and position signal. We have made use of the LeCroy 3377 multi-hit time-to-digital converter having 32 channels capable of registering 16 hits per channel. Moreover, it is characterized by 0.5ns timing resolution, 10 ns pulse pair resolution and 8ns to 32 μs time range per event. Once triggered, the time-to-digital converter records all hits that occur within a predetermined interval of up to 32 μs. When full, the time-to-digital converter's internal buffer digitized by list processor (HYTEC LP1342) is downloaded to the data acquisition computer where the data is analyzed online by a Lab View program. The TDC and ADC are operated in master-slave mode with the ADC as master, triggering the CAMAC crate fast electronics connection.

3. 7 Data analysis

The experimental raw data has been collected in event (laser shot) mode basis by the LabView computer. The raw data provide very basic quantities like the timing and position information of events which can be translated into more physically meaningful dynamical variables (momentum, energy) by a FORTRAN code using the program Physics Analysis Workstation (PAW) for visualization. The initial step of offline data analysis involves the calibration of all the necessary experimental parameters, and is followed by the reconstruction of momentum and energy of a particle to interpret the data. The data itself is the source for calibrating a number of important parameters such as absolute time zero, position zero and cyclotron period except some constants related to the geometry of setup (time-of-flight distance,

spectrometer length, and gap between the spectrometer grid and detector). These dimensions (quantities) were measured during the assembly of the detectors.

3.7.1 Calibration of the absolute time (t_o), zero position (x_o,y_o) and the cyclotron frequency (ω_c)

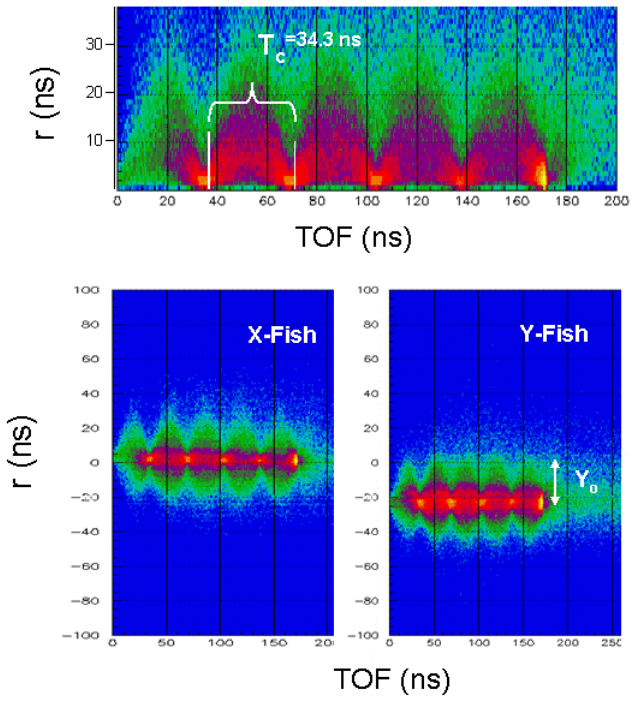

Figure 3.18: Density plots of the wiggle, x-fish and y-fish spectra. The so-called wiggle spectrum is the 2D plot of the time of flight of electrons versus the corresponding distances of hit positions from the center of detector. The different nodes in the wiggle spectrum are the positions of electrons which hit at the center of the detector, and time of flight of such electrons are equal to integer multiples of cyclotron frequency. The distance between any two consecutive nodes is equal to the cyclotron period of a transverse electron in a magnetic field. The wiggle spectrum is very useful to determine the offset time (t_o) in time of flight and the value of magnetic field very precisely. Moreover, a very precise value of the position (x_o, y_o) can be obtained by taking account of the offset value from zero position to the line through nodes in the x- and y-fish spectra (x_o, y_o).

The absolute time zero (~ few ns second) is not so critical for reconstructing the ion momenta because the range of time of flight of such an ion is of the order of thousands of

nanoseconds. But the electron's time of flight even at the low extraction field is so short (~100 ns) that the absolute time zero of a few nanoseconds makes a huge difference in the reconstruction of their momentum. Having the correct value of time zero is the most important step before progressing to data analysis. In order to determine the location of the time zero (offset that has to be added to time of flight to have real time of flight) in the time of flight and the cyclotron period of electrons in the magnetic field, the calibration run can be made at a low extraction field and comparatively higher magnetic field to produce a very broad electron time of flight that will give several positions of nodes as a result of cyclotron motion in the magnetic field as shown in Figure 3.19.

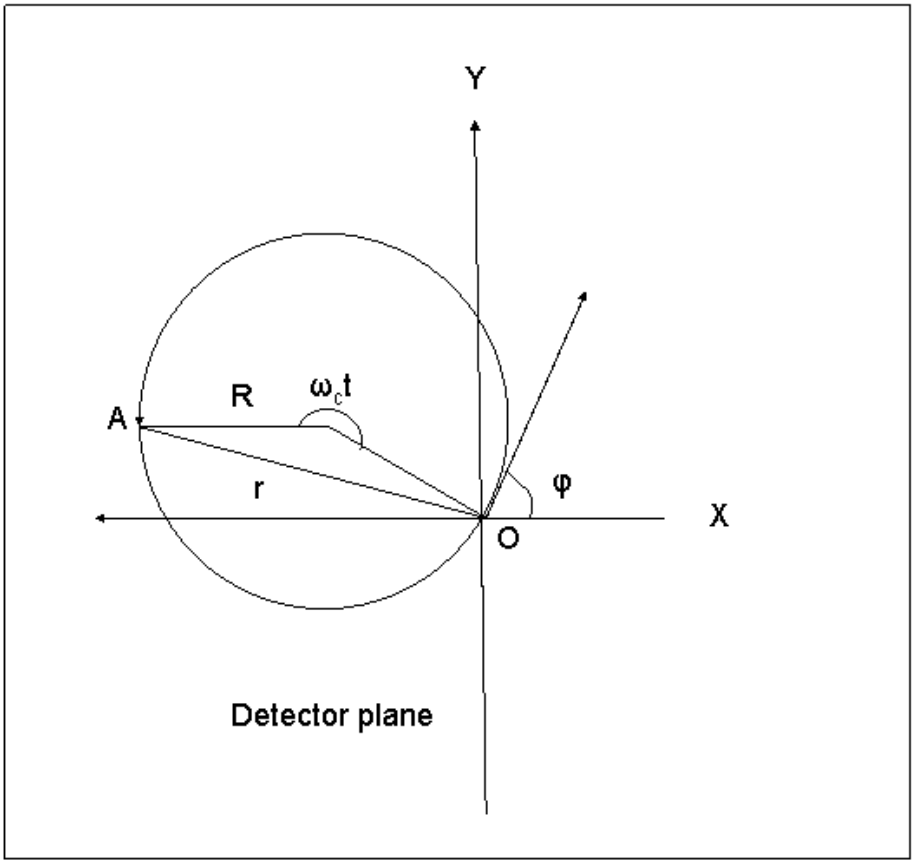

Figure 3.19: Projection of an electron trajectory onto a plane perpendicular to the magnetic field

A plot of the distance of a hit on the electron detector from the center of detector against its time of flight gives the spectrum called 'wiggle' as shown in Figure 3.18. The different nodes spaced consecutively with equal time are the positions of electrons at the center of the detector, and the times of flight of those electrons are equal to an integer multiple of the cyclotron period (T_c). The nodes closer to t = 0 are associated with the TOF of electrons which have higher initial kinetic energy and which are directed towards the detectors (forward electrons). The farther nodes are related to the lower energy electrons or to those electrons which at first fly away from the electron detector and are later diverted by the electric field back to the detector. The boundary which separates the two types of electrons moving in opposite direction can be found by calculating the time of flight of an electron with zero initial kinetic energy.

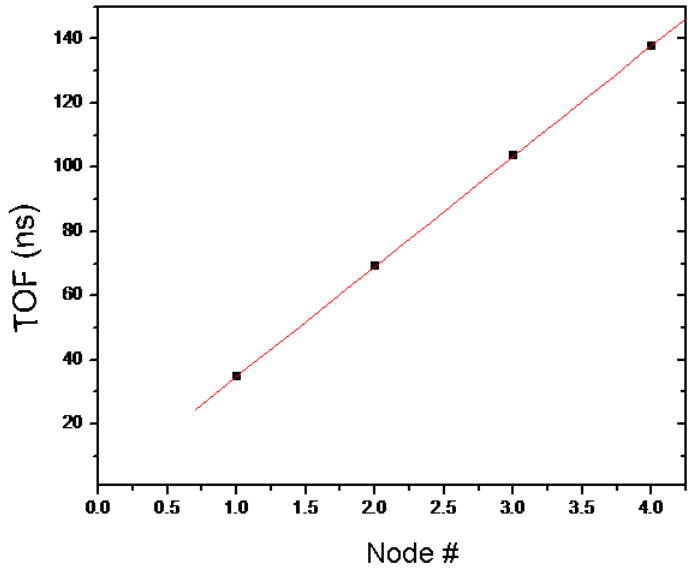

Figure 3.20: Plot of number of nodes versus TOF taken from Figure 3.18. The absolute time zero and the cyclotron period (T_c) of electrons in the magnetic field found from the extrapolation are 2ns and 34.3 ns respectively.

It is clear from the wiggle spectrum that one of the nodes corresponds to the time zero position, and this position can be extrapolated from the position of the other nodes as shown in

Figure 3.20. The absence of counts for this position is due to the fact that no electrons will have zero time of fight. While calibrating the time zero position, it is important to have at least three or four nodes in the wiggle spectrum. The variation of the magnetic field changes the node positions and they are completely independent of the initial energy of electrons and the spectrometer field. Adjusting the magnetic field, the locations of the nodes are given by the expression:

$$T_c = \frac{2\pi m}{Be}, \tag{3.41}$$

where T_c is the inverse of cyclotron frequency and is equal to the distance between any two consecutive node positions. The cyclotron period of an electron T_c observed in the above spectrum is equal to 34.3 ns. The value of the strength of the magnetic field as estimated by equation (3.41) is found to be 10.4 G which is more precise than that measured by gaussmeter, and is enough to collect the transverse electrons having maximum kinetic energy of 27.4 eV. The cyclotron frequency in this example can be calculated as:

$$\omega_c = \frac{2\pi}{T_c} = \frac{2.\pi}{34.3ns} = 0.18309\,GHz \ . \tag{3.42}$$

3. 7. 2 Reconstruction of momentum of ion and electron

The next step of the data analysis involves the reconstruction of the momenta of ions as well as of electrons after calibrating all the necessary experimental parameters. Both the ion and electron detectors provide the timing and position information of the detected particles. Once the distance of the detector from the reaction zone (S_r), the value of the electric field (E) over the length of the spectrometer, and the experimentally observed time zero position (t_o) including the time of flight and hit position, are known precisely, then the three components of momentum gained by an ion in the laser field in three mutually perpendicular directions are calculated by using simple relations:

$$P_{z(ion)} = \frac{m_{ion} S_r}{t_i} - \frac{Eqt_i}{2} \tag{3.43}$$

$$P_{x(ion)} = \frac{m_{ion} X_r}{t_i} \tag{3.44}$$

$$P_{y(ion)} = \frac{m_{ion} Y_r}{t_i}, \tag{3.45}$$

where $P_{z(ion)}$ is the momentum of an ion in the z-direction parallel to the detector axis. In this equation the timing information of the detected particle is provided by the difference between the START and STOP signal from the photodiode and the MCP detectors with correction for the time zero (Time of flight as shown in Figure 3.21). The other two transverse components X_r and Y_r positions of the ion are obtained from the position sensitive detector as shown in Figure 3.22.

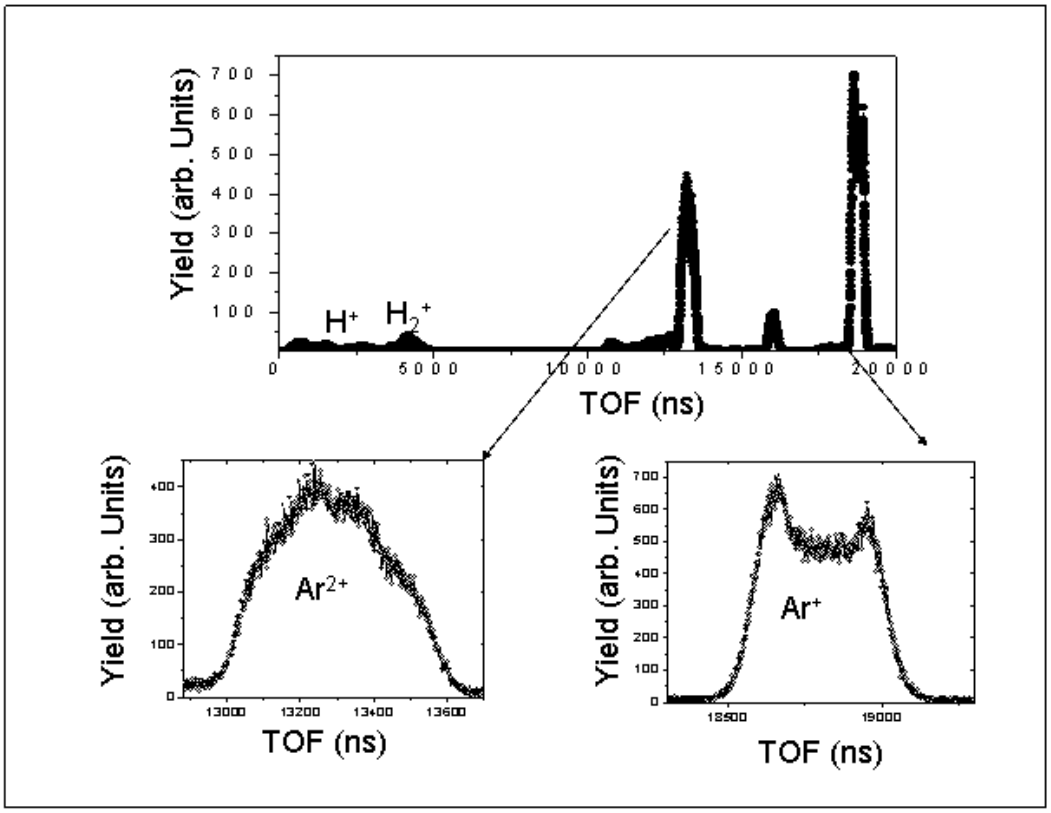

Figure 3.21: Time-of-flight spectrum of the recoil ions. It is noted that this timing information of any selected channel is used for off-line calculation of momentum of the channel (fragment) by using the list of equations (3.43 - 3.45).

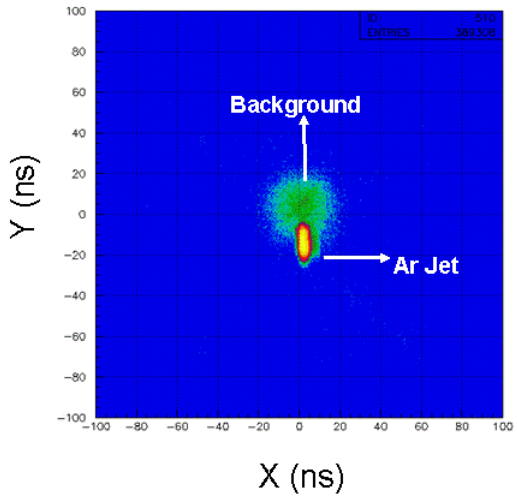

Figure 3.22: The ion detector image observed for an argon target at low extraction field (1V/cm). Similarly the position information is also used for the momentum calculation by using equations (3.44) and (3.45). The position of the jet (Ar ions) and the background (mainly H_2O^+) are well resolved.

Similar to the detection of ions, the photoelectrons directed to the electron detector along the spectrometer axis can also be collected by the spectrometer fields. The expression used to determine this component of electron momentum is basically the same as that for an ion. Since the transverse electrons are driven by an external magnetic field, then an additional parameter (cyclotron frequency ω_c) is needed to calculate the momenta of those electrons [45]:

$$P_{ze} = \frac{m_e S_e}{t} - \frac{Eet}{2} \tag{3.46}$$

$$P_{xe} = \frac{m_e \omega_c}{2}\left(X_e \cos\left(\frac{\omega_c t}{2}\right) + Y_e \right), \tag{3.47}$$

$$P_{ye} = \frac{m_e \omega_c}{2}\left(Y_e \cos\left(\frac{\omega_c t}{2}\right) - X_e \right), \tag{3.48}$$

where t, X_e and Y_e are time of flight and position signals obtained from the PSD, and ω_c is the cyclotron frequency , and is calculated by using the cyclotron period

$$\omega_c = \frac{2\pi}{T_c}.$$

The timing information can be obtained from the electron time of flight as shown in Figure 3.23.

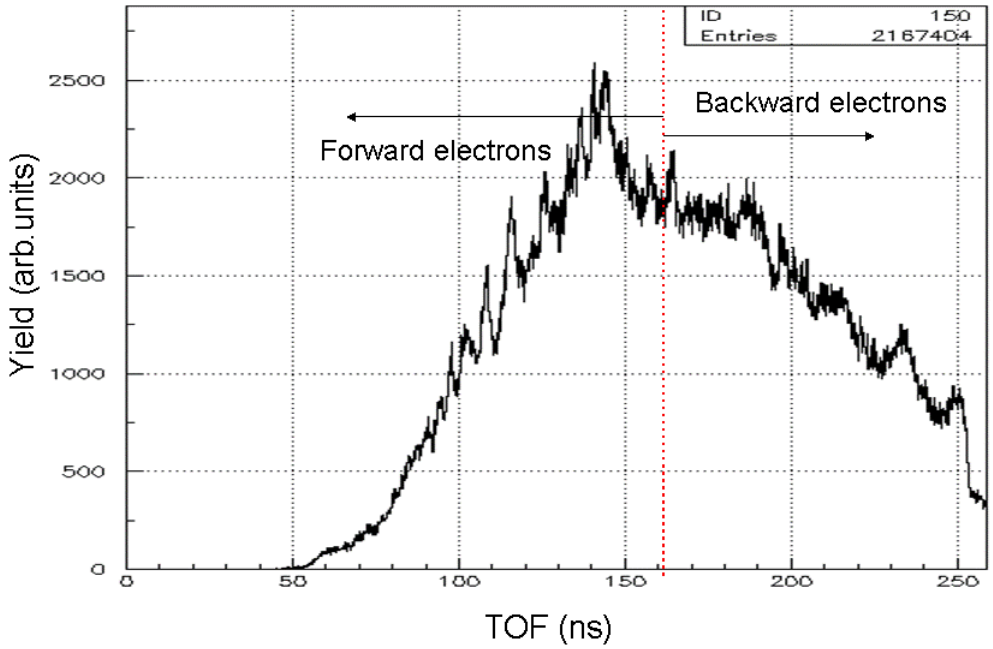

Figure 3.23: The typical example of the time of flight of electrons observed at peak intensity (~1x10^{14}W/cm^2) in low extraction (1V/cm) and magnetic field (3 G) using the detector at the longer side of the spectrometer arm (24 cm from the focus). The red line corresponds to the time of flight (162 ns) of the electrons released with zero initial kinetic energy. The left part of the spectrum is the time of flight of those electrons which are directed towards the detector, whereas the right part is the TOF of an electron initially directed opposite to the detector, and eventually driven back to the detector by the extraction field. This is why backward electrons have longer time of flight. The electrons having higher initial kinetic energies show the shorter time of flight.

3. 7. 3 Calibration of laser parameters

3. 7. 3. 1 Pulse duration

The essential parameters of a laser pulse such as its length and peak intensity need to be determined accurately. Especially, the correct values for them are very crucial for any kind of time resolving and intensity dependent experiments. There are well known and comparatively standard ways to determine the duration of a pulse by different autocorrelation methods. One of them, frequency resolved optical gating (FROG), is routinely available to extract the length and bandwidth of a pulse. The pulse length measured by FROG can be rechecked, *in situ*, accurately by inspecting the energy released by the fragments of the Coulomb explosion channel of H_2 or D_2. The measured KER (kinetic energy release) produced by the sequential ionization can be used to read the inter-nuclear distance at different times in units of a half optical cycle [46]. One can deduce the inter-nuclear distance by observing the sum energy of the fragments. The fragments will possess more energy if they start exploding at a small inter-nuclear distance and vice versa which is in turn determined by the shortness of a pulse. It has been shown [47] that when pulse rise time is sufficiently short ($\tau < 15$fs), Coulomb explosion of H_2 (D_2) may occur at a small inter-nuclear distance via sequential ionization. The kinetic energy released by protons from the hydrogen molecules in such a case is directly associated with the shortness of the pulse used.

3. 7. 3. 2. Peak intensity

Peak intensity of the laser is one of the most important and very sensitive parameters of a laser pulse to be determined correctly in order to make a correct interpretation of the strong field phenomena. Obviously, there are various ways to determine the peak intensity in the reaction zone. I would like to discuss some of approaches we have actually used during the course of different experiments.

1. One of the easiest approaches to determine the peak intensity of a laser is to use the focal diameter in the calculation of equation (3.49). The focal diameter can be determined using

the CCD camera. Using the information of pulse duration, repetition rate and measured power, the peak power can easily be estimated with the relation

$$I_o = \frac{P}{\pi w_o^2 \tau R}. \tag{3.49}$$

For a typical experiment,

$$I_o = \frac{P}{\pi w_o^2 \tau R} = \frac{10 \times 10^{-3}(W)}{\pi (7.10^{-6}(m))^2 \times 1000(Hz) \times 30.10^{-15}(s)} = 2.16 \times 10^{14} Wcm^{-2} \tag{3.50}$$

where P is the power measured directly by a power meter on the optical path before focusing, w_o is focal radius measured with CCD camera, and τ and R are pulse length and repetition rate of the pulse. The non-uniform intensity distribution at the focus is shown in Figure 3.24.

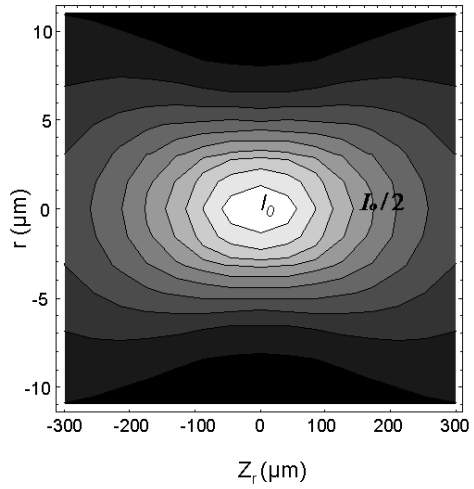

Figure 3.24: Plot of the iso-intensity contours at the focus of the parabolic mirror simulated by taking account of pulses of 30 fs with peak intensity of 2.16 x 10 ^{14} W/cm^2; the radius of focus (w_o) and Rayleigh length (z_r) are 7 μm and 192 μm, respectively.

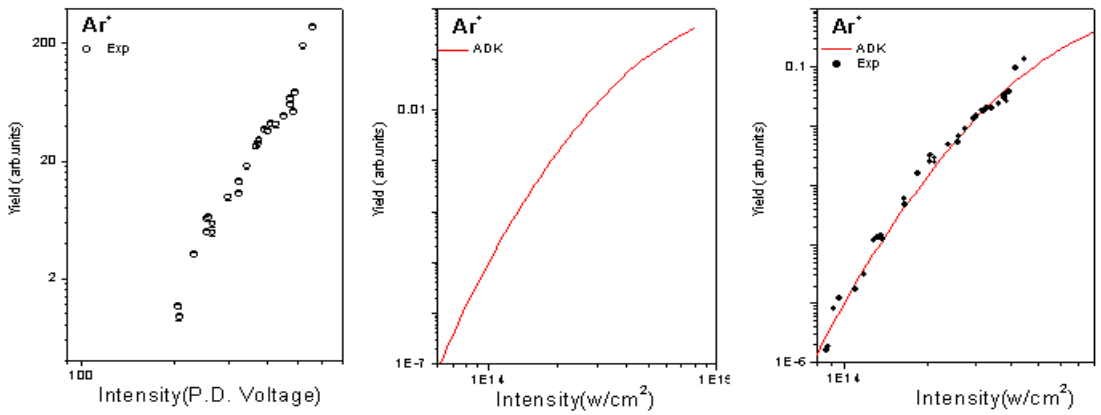

Intensity Calibration constant=0.8x10^{12} W/cm^2

Figure 3.25: Illustration of the typical calibration of the photodiode channels by fitting the ADK to the observed channels of the photodiodes corresponding to the different peak intensities. (a) The experimental yield curve of Ar^+ versus the corresponding photodiode channels; (b) the theoretical ADK yield curve for the single ionization of Ar^+; (c) fitting the theoretical ADK to the experimental yield curve. The fitting constant ($0.8.x10^{12}$ Wcm^{-2}) gives the necessary calibration factor to determine the peak intensity of the laser for any value of the photodiode voltage.

The accuracy of the peak intensity can be rechecked by fitting the yield of ionization of argon to the theoretical ADK curve as shown in Figure 3.25. Fitting all the photodiode channels with the theoretical ADK curve gives the necessary calibration factor (constant) for determining the peak intensity corresponding to each channel of a photodiode measurement.

2. Calibration of intensity measuring the beam diameter in the far region: This is the easiest approach to calibrate the intensity, *in situ*, during the experiment, providing all the other parameters required for the calculation (pulse duration and repetition rate) are known. The method involves the measurement of power for the different diameters of incoming beam at the far field of the focusing mirror. These experimental observations are then fitted to equation (3.51) to determine the FWHM of the diameter of the beam as shown in Figure 3.26.

$$\frac{I}{I_{sat}} = 1 - \exp(-2r^2 / w^2) \tag{3.51}$$

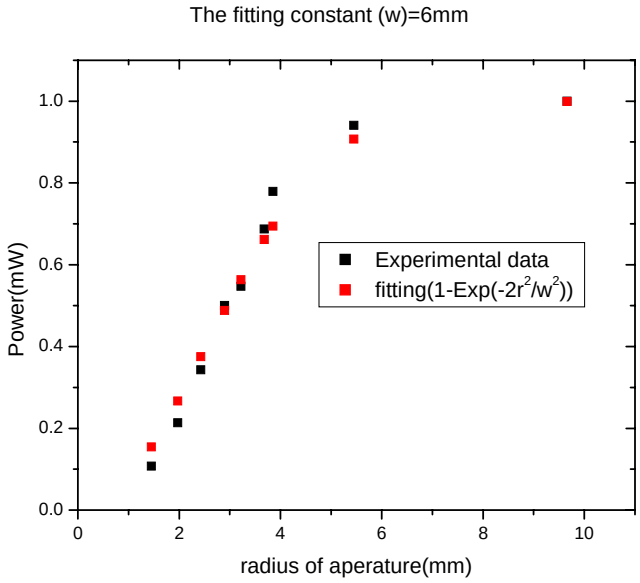

Figure 3.26: The fitting of equation (3.51) to the observed power vs radius of aperture placed perpendicular to the beam direction in the far field of the parabolic mirror. The FWHM of beam diameter of the laser is found to be 6mm.

The beam size at any point closer to the focal spot can be related to the focal spot radius (ω_o), distance of that point from focal spot (z), and Rayleigh length z_R,

$$w(z) = w_o \sqrt{1 + \left(\frac{z}{z_R}\right)^2} \tag{3.52}$$

If the focusing mirror with focal length f is at z = f,

$$w(f) = w_o \sqrt{1 + \left(\frac{f}{z_R}\right)^2} \tag{3.53}$$

where ω(f) is the radius of the beam at the mirror . Since f >> z_R then,

$$w(f) = \frac{w_o f}{z_R} \tag{3.54}$$

and

$$z_R = \frac{\pi w_0^2}{\lambda}. \tag{3.55}$$

The radius of the focus can be expressed in terms of the focal length of the mirror, size of beam, and wavelength of light,

$$w_0 = \frac{f\lambda}{\pi w(f)} \tag{3.56}$$

The FWHM of the radius of the beam sent from the KLS is typically 3mm at the central wavelength of 800nm; the focal length of the parabolic mirror is 7.5 cm. The radius of the focus as calculated by the above relation gives

$$w_0 = \frac{f\lambda}{\pi w(f)} = \frac{7.5\times10^{-2}(m)\times800\times10^{-9}(m)}{\pi\times3\times10^{-3}(m)} = 6.34\mu m \tag{3.57}$$

and Rayleigh length (z_r)

$$z_R = \frac{\pi w_0^2}{\lambda} = \frac{\pi(6.34\times10^{-6}(m))^2}{800\times10^{-9}(m)} = 157.76\mu m \tag{3.58}$$

For example, if the measured power of the beam is equal to 10 mw, then the peak intensity is found as

$$I_o = \frac{10\times10^3}{\pi(6.34\times10^{-6}(m))^2\times1000(Hz)\times30\times10^{-15}s} = 2.6\times10^{14}Wcm^{-2} \tag{3.59}$$

3. Calibration of intensity with the circular polarization of light: One can deduce the peak intensity from the measured drift momentum gained by an electron in ionization by circularly polarized light. The magnitude of the drift momentum gained by an electron in a circularly polarized laser field is directly related to the strength of the electric field of the pulse

$$P_0 = \sqrt{P_x^2 + P_y^2} = \frac{eE_o}{\omega}. \tag{3.60}$$

Unlike the drift momentum gained by an electron in a linear pulse, the drift momentum gained by it in a circular pulse is independent of the phase at which the electron was born [48]. Knowing the magnitude of the drift momentum of the electron in a circularly polarized pulse will eventually give the strength of the electric field at the time of ionization. The peak laser intensity is calculated using equation (3.61):

$$I_o = c\varepsilon_o|E_0|^2 \tag{3.61}$$

where c and ε_o are the velocity of light and permittivity in the medium, respectively.

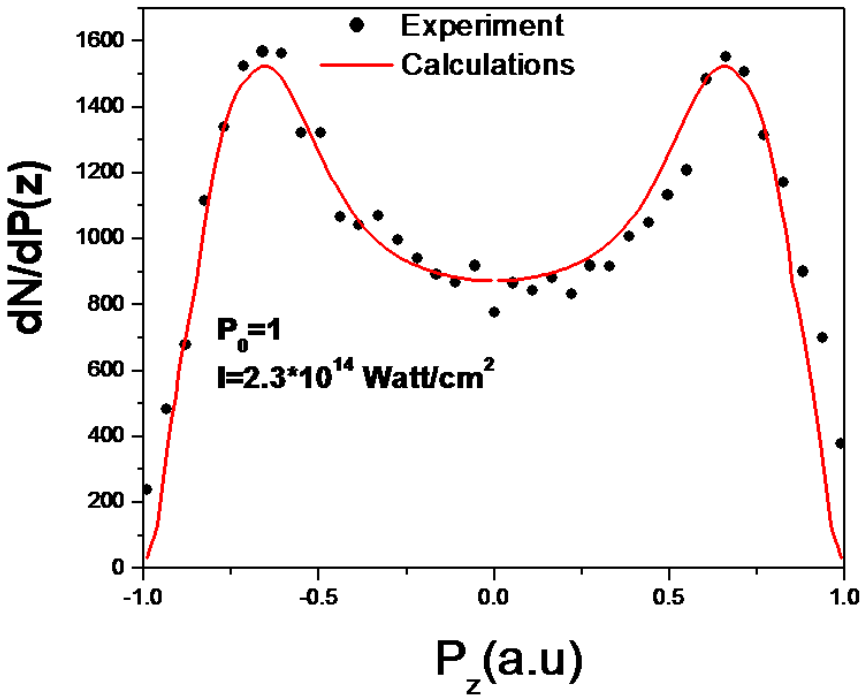

Figure 3.27 : Projection of momentum image of H_2^+ in the polarizing plane of the circularly polarized pulse onto the time direction along the axis of the detector. The theoretical curve (red curve) is fitted to the experimental curve (dotted curve) to find the drift momentum corresponding to the peak intensity. [Simulation was done by A. S. Alnaser.]

From Figure 3.27, at peak momentum, $P_o = 1$a.u.

$$\omega = 2\pi f = 2\pi \frac{c}{\lambda} = \frac{2\pi \times 137.036 \times 5.29 \times 10^{-11}}{800 \times 0^{-9}} = 0.057 a.u.. \qquad (3.62)$$

The peak electric field of a laser pulse corresponding to the given momentum is

$$E_o = \frac{P_o \omega}{e} = \frac{1 \times 0.057}{1} a.u. = 0.057 a.u. = 0.057 \times 5.142 \times 10^{11} Vm^{-1} = 2.9 \times 10^{10} Vm^{-1} , \qquad (3.63)$$

and the peak intensity is

$$I_0 = c\varepsilon_0 E_o^2 = 3 \times 10^8 \times \frac{1}{4\pi \times 9 \times 10^9} \times (2.9 \times 10^{10})^2 = 2.2 \times 10^{14} Wcm^{-2}. \qquad (3.64)$$

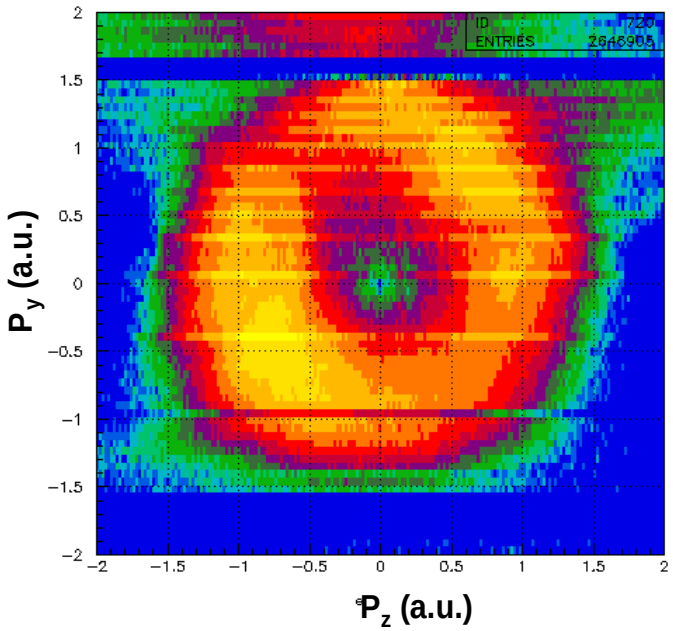

Figure 3.28: The 2D momentum image of electrons in the plane of polarization of the circularly polarized pulse. The radius of the donut (~1a.u.) will give the momentum of the electron at the peak of laser intensity as calculated in the text.

It should be pointed out that this method of determining the absolute intensity is valid for the intensities where the ionization rate changes rapidly before reaching the peak intensity (i.e. below the saturation intensity). In order to determine the peak intensity more accurately, the experimental curve can be fitted to the theoretical ionization rate as a function of temporal profile, and drift momentum at peak intensity [49].

CHAPTER 4 - Angle and energy structure of low-energy electrons generated by short pulses at high intensities from argon atoms

4.1 Introduction

The study of electron energy distributions from tunneling ionization processes has been an active topic of research for the last several years. Most of the theoretical and experimental work has focused on the higher part of the photoelectron spectrum dominated by the above-threshold process. The typical features of the spectrum such as plateau and angular structure related to the ATI in the region can be observed and interpreted [51]. Less work has been reported on the intensity dependence of the momentum resolved photoelectrons of low kinetic energy [52, 53, 54]. In this chapter we present our experimental effort to analyze the complex angular and energy features that appear in the lower energy part of the electron distribution of the strong field ionization of argon over a range of wavelengths.

4.2 Above-threshold ionization in tunneling region: high and low energy parts of energy spectrum

The satellite structures of ATI are well known from resonance enhanced multi-photon ionization at lower intensities [17]. The underlying mechanism has been explained in Chapter 2. In such a case, the bound-to-bound transition is much stronger than direct ionization, and once populated, the excited states ionize easily. However, this is not necessarily expected to be the case in a relatively higher value of intensities (low value of Keldysh parameter). It should be pointed out that all the excited states lie very far above and outside the potential barrier created by the combined action of the laser and Coulomb field [2]. Under this condition, the electron cannot resist the laser field and is driven into a full blown quiver motion. Any resonant states must be completely deformed by the laser, since its pondermotive energy is much greater than its binding energy [2]. Therefore we do not expect to see any resonance structure in this intensity range. However, the narrow width of these individual structures suggests that these states must

have significant lifetime [3]. It is not surprising that the characteristics of the multi-photon resonance remain well within the tunneling regime. Studies of ATI in the high-energy plateau region have revealed complex energy structure and extreme sensitivity to the laser intensity [3, 55]. These were interpreted both in terms of resonant Rydberg structures and channel closing [56, 7].

The two-dimensional momentum images of the laser-generated electrons at intensities in the tunneling regime for very short pulses found by Rudenko *et al.* [53] show complex structure in both energy and angle in the region of the first few ATI peaks in the low energy region. The angular structures are specified with many radial strips originating from the origin with distinct nodes and antinodes. The energy structures which do not move with laser intensity suggest that the multi-photon resonance process plays a key role for producing these structures. Since the experimental report of Rudenko *et al.* [53], various theoretical models have been put forward to interpret these experimental data [5, 6, 7]. Arbó *et al.* [5] suggested that the observed structure originates not from the resonances but from the diffraction of the ejected electrons in the field of the parent of the ion, while M. Wickenhauser *et al.*[6] has suggested that the multi-photon parity and dominant angular momentum of the ATI peaks determine these structures.

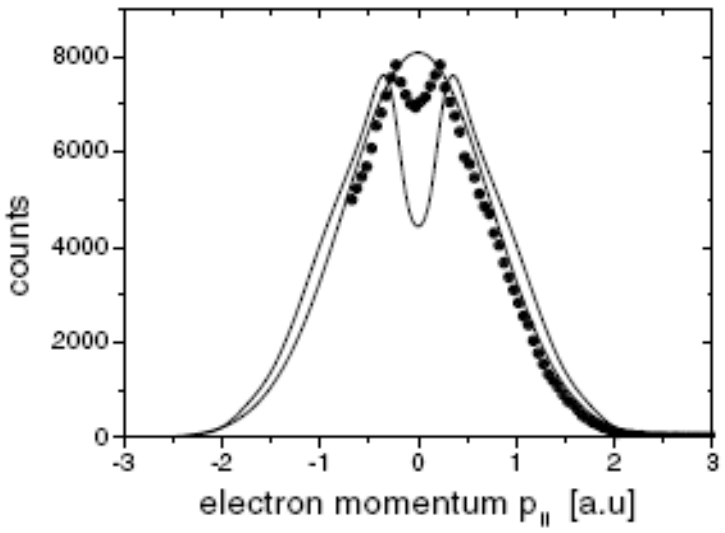

Figure 4.1: The spectral feature for ultralow energy electrons in longitudinal direction generated by laser field at the intensity in the tunneling regime, first reported by R. Moshammer *et.al.* (extracted from [56])

4.3 Low energy features in ion spectra in the tunneling region

Closely related to the issue of the low energy features of electron spectra, Moshammer *et al.* [56] reported the surprising result of the momentum spectrum of single ionization of neon (Ne^+) along the direction of polarization of the laser, which shows a minimum at zero momentum as shown in Figure 4.1. This observation is quite contradictory to the well accepted ADK tunneling model, which predicts peak at zero momentum. They suggested that the structure is due to the rescattering of ultra low energy electrons from the ion core.

This interpretation of the experimental observation of dip in longitudinal momentum was supported by the CTMC (Classical Trajectory Monte Carlo) of Chen and Nam [57]. Soon after, Dimitriou *et al.* presented an alternative interpretation based on their theoretical work of atomic hydrogen ionization using a quasi-classical trajectory method including tunneling [59]. Instead of rescattering, they attributed this structure to the influence of the Coulomb potential of the ion on the outgoing electron wave packet. Furthermore, Faisal and Schelegel added more analysis to this problem using the KFR (Keldysh-Faisal-Reiss) theory of intense-field processes, and concluded that the structure arises from a discrete photon absorption mechanism in the tunnel regime [60].

Basically both the electron and ion momentum images give the same information for the dynamics, since momentum is conserved in the emission event, and the laser field imparts equal momentum to both partners in the single ionization process. Because of better resolution in the electron momentum image in the transverse direction, compared to the ion, the electron momentum image is more capable of giving well-resolved features.

4.4 Method

In order to produce the second harmonic (400nm) from the fundamental (800nm, pulse duration ~ 30fs), a thin BBO (10μm) crystal with about 20 % efficiency was used just before the interaction chamber, and the resulting pulse duration after the BBO crystal was ~45 fs. Other wavelengths (590nm, 615nm, 640nm, 680nm) were produced by frequency doubling of the tunable output of a traveling-wave optical parametric amplifier of superfluorescence (TOPAS,

Quatronix) pumped by an 800nm beam. We estimate the pulse duration of those pulses to be about 40-50 fs. The laser polarized along the spectrometer axis (z-direction), was focused by a parabolic mirror of focal length 7.5 cm onto a supersonic gas jet of argon. The electrons released at the interaction zone were guided to the detector under the combined effect of the electric (1V/cm) and magnetic fields (~4 G).

4.5 Energy and angular features in 2D momentum image

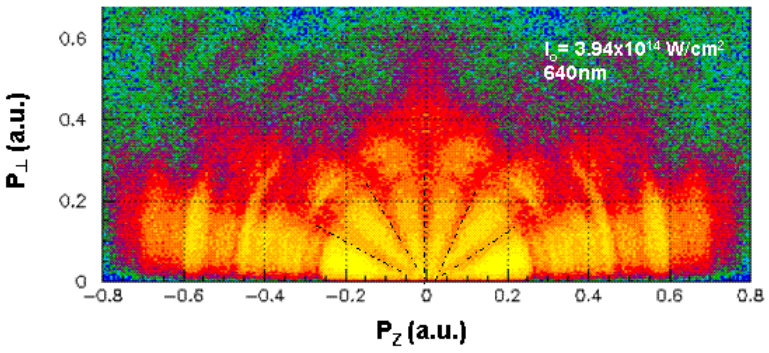

Figure 4.2: Density plot of the 2D momentum image of electrons ionized from argon for wavelength 640 nm.

Compared to the one-dimensional energy plot, the two-dimensional angle resolved spectra are a rich source for information on the ionization dynamics in a laser field. Figure 4.2 shows the density plot for such a purpose. It is the plot of the momentum of electrons generated from single ionization of argon in the longitudinal direction (P_z-direction) and their transverse momentum ($P_t = \sqrt{P_x^2 + P_y^2}$). The vertical scale is a log scale. Electrons created by a given

kinetic energy appear along a well-defined circular pattern. The radius is proportional to the momentum of the electron as given by

$$P = \sqrt{P_z^2 + P_t^2} \tag{4.1}$$

The momentum image contains the signal of photoelectrons created by different processes, resulting in a superposition of many corresponding patterns. The symmetry in the image is the result of the symmetric distribution of the photoelectrons about the polarization axis. In this representation ATI peaks and their substructures manifest themselves as ring-like structures.

In the density plot, it is easier to observe the angular structure of electrons having any specific energy. It is clear from Figure 4.2 that the spectral features in the lower energy side are observed with very rich angular and energy structure. In this part of the thesis, we explain the physics of these structures. All the 2D momentum spectra in the present study are integrated over the azimuthal angle, making the density distribution close to the polarization direction zero.

$$\frac{dN}{d\theta} = \frac{dN}{d\Omega}\sin\theta \tag{4.2}$$

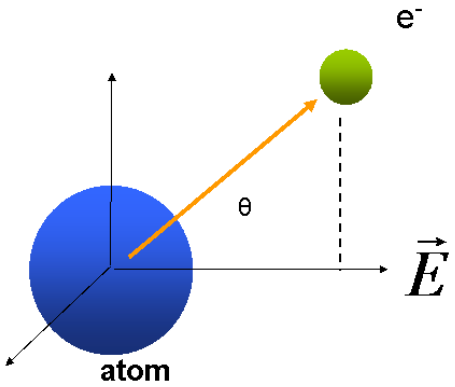

Figure 4.3: Illustration of the emission angle of an electron with the direction of the polarization of the laser.

As we pointed out above, the spectra are symmetric around the zero because symmetry is maintained during the emission process. For the sake of convenience, we have taken the negative axis along the horizontal scale of the plot for those electrons which were directed towards the detector. The positive part of all the spectra presented here is the mirror image of the negative part in order to make them symmetrical. We reflected the negative part of the image onto the positive part to omit some of the nodes present in the lower energy structure of that side. In order to make a 4π solid angle collection of electrons having energy range up to 5eV, we superimposed the magnetic field of strength 4 G with the uniform electric field. The magnetic field produces some nodal structure for those electrons for which the time of flight equals a multiple of the cyclotron period. At nodes the spectrometer has no resolution in the transverse direction.

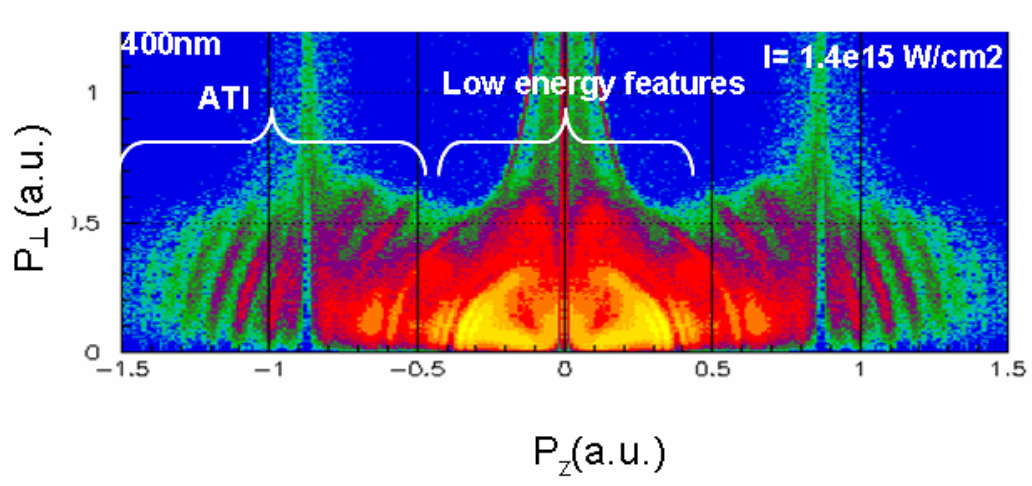

Figure 4.4: Density plot of parallel momentum versus transverse momentum of an electron generated by a laser pulse at 400nm central wavelength. The lower part of the spectrum is rich in angular and energy features but the higher part shows only the well known ATI structure.

Understanding the low energy features of the spectra is the main objective of the present study. On the basis of the structure observed, each spectrum can be studied by separating it into two distinct parts: higher energy and lower energy features. Figure 4.4 shows the momentum space image of the electron generated by a laser pulse at central wavelength 400 nm. The higher

energy part of the spectrum consist of series of truncated rings of constant energy which are associated with the above-threshold ionization (ATI), whereas the feature observed at the lower energy part can be characterized by the ATI and its substructure (Freeman resonance [17]). It can be seen that the density is not constant over these structures, but has maxima and minima. In other words these structures appear as series of radially outward fans coming out of the origin.

4.6 Why do we choose to study the lower energy part?

Properly addressing the special feature of the images of the laser generated electron requires a highly resolved structure, which in turn depends on the laser bandwidth and the resolution of the measurement technique. In addition to these, another factor which limits the resolution is the externally applied magnetic field. Though the magnetic field helps to collect the higher transverse electrons, at the same time it degrades enhancement of the structures of the image. Therefore we applied a low magnetic field of only a few gauss (4 G) which is just sufficient to collect transverse electrons of only a few electron volts. Moreover, the COLTRIMS technique is superior to the other detecting systems for collecting very low energy electrons even of zero kinetic energy, with extraction field along the spectrometer at the expense of resolution. The momentum resolution of the current system along the spectrometer direction is given by

$$\Delta P_z = 0.01 a.u.$$

The energy of the particle can be expressed as

$$E = \frac{P_z^{\,2}}{2m} \quad . \tag{4.3}$$

The energy resolution is given by

$$\Delta E = P_z \Delta P_z \text{ a.u.} \tag{4.4}$$

or

$$\Delta E = \sqrt{2E_z}\,\Delta P_z \text{ a.u.} \tag{4.5}$$

From equation (4.5) it is clear that the energy resolution is better at the low energy part, and it degrades on the higher energy part. The energy resolution at 1eV is calculated as

$$\Delta E = \sqrt{2E}\,\Delta P_z a.u. = \sqrt{2 \times \frac{1}{27.2}} \times 0.01 a.u. = 73.7 meV \; . \tag{4.6}$$

Let us take the higher energy part of the spectrum at $p_z = 0.8$ a.u., and the corresponding value of the energy is 8.7 eV. The energy resolution at this value of momentum is given by

$$\Delta E = \sqrt{2 \times \frac{8.7}{27.2}} \times 01 a.u. = 217 meV \,. \tag{4.7}$$

Obviously, the resolution deteriorates on the higher energy side; consequently we can barely observe substructure in some ATI peaks.

The low density towards the perpendicular direction on the higher energy side of the spectrum is due to the weak magnetic field which is not sufficient to drive the higher transverse electrons to the detector.

4.7 Intensity dependent momentum space images

The electron energy spectra observed at 640 nm for three different intensities are plotted as shown in Figure 4.5. And it shows how the spectral features typically depend on the laser intensity. Some of the spectral features of this spectrum remain unchanged even though they were observed at different intensities. These intensity independent features are attributed to the Freeman resonances. The yield of each peak associated with the Freeman resonances depends strongly on the intensity, but the positions of the peaks remain unaffected. Since these resonance states are aroused from the states close to the continuum which show the same pondermotive shift as the continuum at a specific intensity, these states yield the same electron energy regardless of the volume. The intensity required for Freeman resonance states are contributed by somewhere from the focal volume since we do not control the volume in our experiment. It is pointed out that the resonances can take place before and after the peak field. Apart from these, the electron may come from the region in the interaction volume which is off the propagation direction, and therefore originate from an atom experiencing lower temporal peak intensity. The pronounced resonance peaks are the result of summing all these contributions, and the ionization enhancement due to a particular resonance always produces electrons at the same energy. No matter when or where they have been emitted, the contributions add up to the same energy, thus giving peaked structures. In addition to these, some peaks in the spectra are found to shift their respective positions with the variation of intensities.

The broadening of the peak around 2eV is due to electrons from non-resonant ionization. Unlike the resonant ionization where the contribution always added up to the same energy, non-resonant peaks shift as the intensity is raised. Peaks other than resonance are ATI peaks. Their positions are strongly dependent upon the laser peak intensity [52]. The same features can also be seen for 400nm in Figure 4.7.

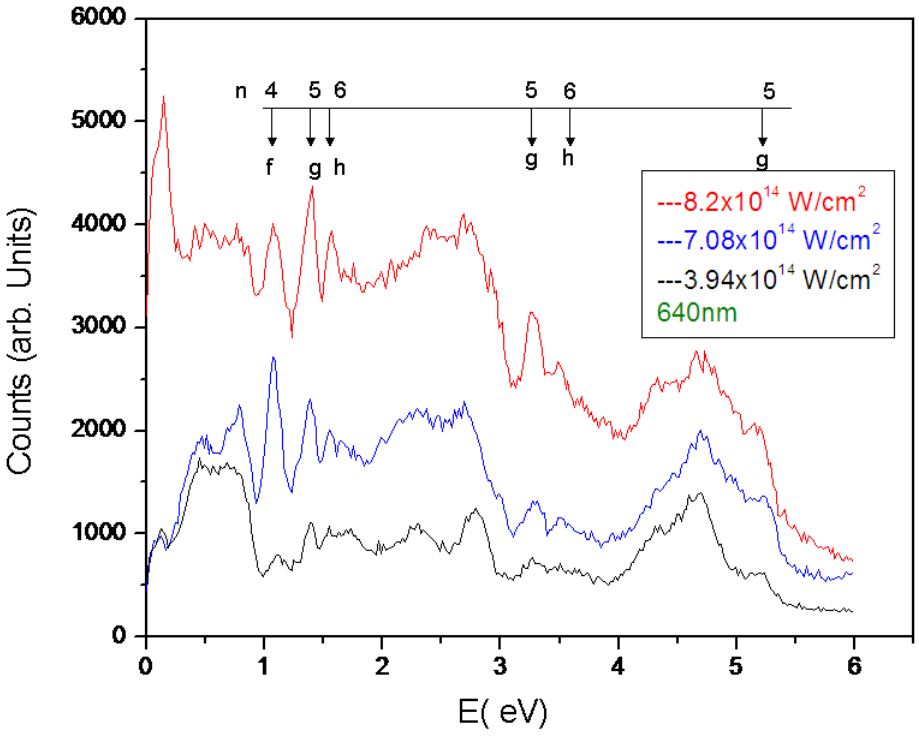

Figure 4.5: Electron energy spectra for 640nm at the intensities 3.94×10^{14} W/cm2, 7.08×10^{14} W/cm^2 and 8.2×10^{14} W/cm^2 respectively. The spectra consist of very pronounced peaks at 1.08eV, 1.39eV and 1.55 eV. These are repeated at other high ATI but they are poorly resolved. They are associated with the electron generated from the corresponding high Rydberg resonance states: 4f, 5g and 6h. The first resonance peak is separated from the consecutive similar peak by one photon (1.93 eV).

In Figure 4.6 we have plotted the momentum of an electron in the polarization direction against the transverse component at 640 nm central wavelength. The signature of all these three spectra is that the basic spectral features remain the same even though they were not observed at the same intensity. All the Freeman resonance structures are clearly seen as very

pronounced ring structures between the momenta 0.2 a.u. and 0.35 a.u. in the second ATI peak in the upper two spectra. They are repeated around 0.4 a.u. but they are relatively fainter in density, and also they are more poorly resolved than the previous one. The resolution is not enough to see these structures beyond 0.6 a.u. As a result we have seen only ATI structures.

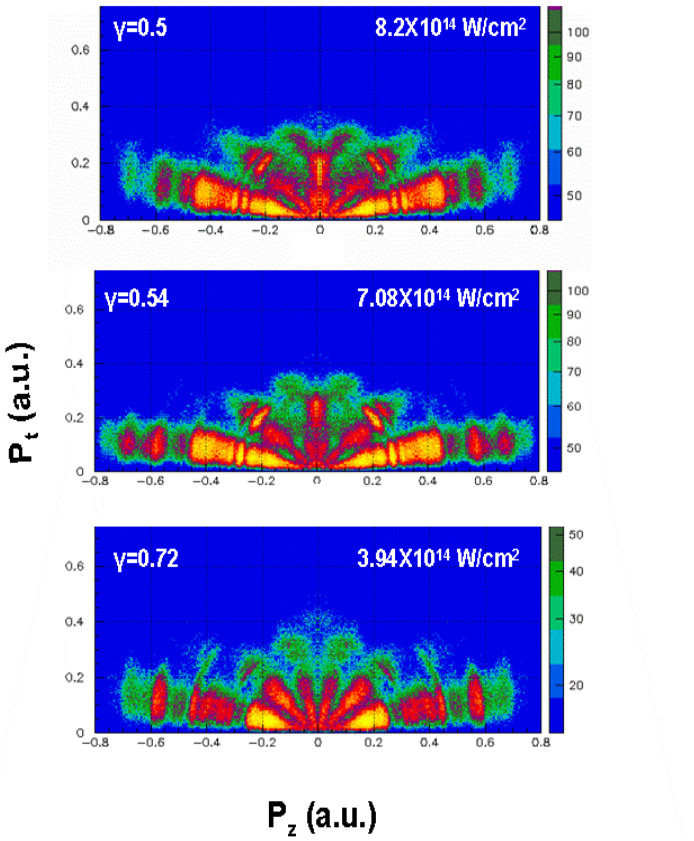

Figure 4.6: Density plot of parallel momentum versus transverse momentum for 640nm at three different intensities as shown in each panel. It is noted that the radial features in the upper two spectra consist of an equal number of nodes and antinode structures, but the bottom one is found to be reduced by one.

The remarkable feature of all these spectra is that the angular structure consists of radial features spreading out of the origin. These structures are made up of a distinct number of alternating nodes and anti-nodes in each ATI; and also the number of nodes is increased by the addition of one to the next adjacent higher ATI. The strong enhancement of the 5g resonance in every spectrum, which is also seen in many published spectra, is associated with the longer lifetime of the state [52]. The number of nodes observed in the first two spectra is 4 even though the two are observed in two different intensities, whereas the number is 5 for the bottom one,

which is at intensity lower than those in the upper two by a factor of 2. The node number in each spectrum is associated with the parity of the first ATI, which is ultimately determined by the number of photons absorbed to ionize an atom initially in the p orbital [6] [please see further discussion in section 4.9]. The intensities in the first two cases are such that both of them required an equal number of photons to ionize; as a result, both spectra show the same dominant angular momentum. However, it is different for the third one.

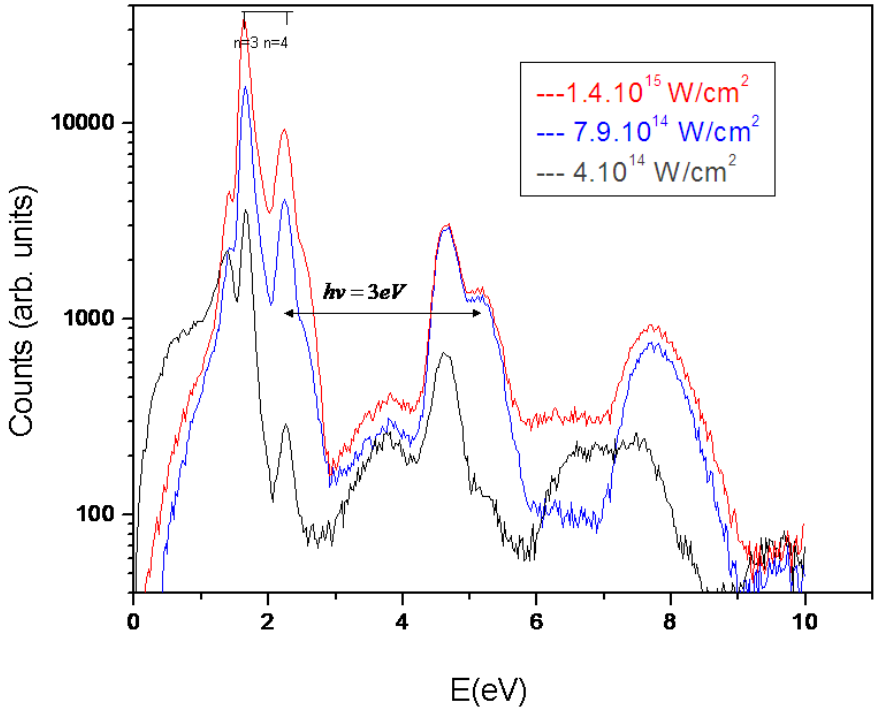

Figure 4.7: The lower energy part of the electron energy spectra for 400nm at intensities 1.4×10^{15} W/cm^2, 7.9×10^{14} W/cm^2 and 4×10^{14} W/cm2 respectively. The pronounced peaks are associated with the Freeman resonances.

Figure 4.8 show the spectra generated by solving the time dependent Schrödinger equation including the effect of laser focus volume [9]. The gas target overlaps not only the center of focus, but also the consecutive shells around it where the laser intensity is lower. The volume effect accounts for a greater contribution of the ionization from the larger outer volume than the central region. The experimental spectra are qualitatively agreement with theory.

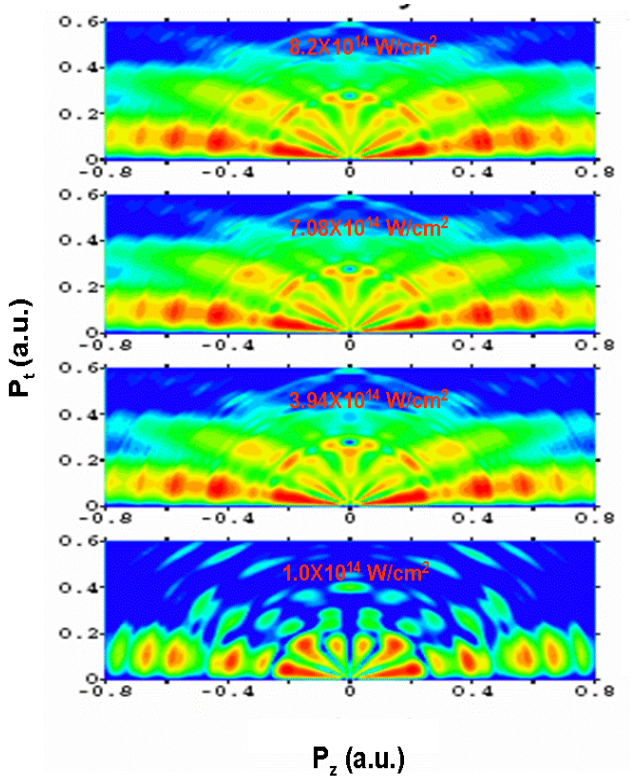

Figure 4.8: Theoretical calculation for comparison of the data presented in Figure 4.6. Adapted from [9].

4.8 Wavelength dependent angular and energy structure

The lower energy features of each spectrum within the range of momentum from 0 to 0.4 a.u. in Figures 4.9 and 4.10 are very rich in structures, and are dominated by the fan-like stripes radiating outwards from the origin. Furthermore, the dominant angular momentum (l) in the continuum does depend on the wavelength and intensity. This is expected because the number of photons necessary to reach a particular resonance depends upon these factors.

If some of the energy structures arise from the electrons released from the highly resonant Rydberg states (Freeman resonance), they must exhibit a specific dependence on the laser photon frequency. In order to point out this issue more specifically, we have studied the wavelength dependence to address the question of whether the observed energy structure can be attributed to Freeman resonances. We have chosen a series of wavelengths of the laser, 400nm, 519nm, 615nm, 640nm, 680 nm and 800nm for our study, more or less at the same intensities for

all the wavelengths as shown in Figures 4.9 and 4.10. The Freeman resonance structures have been studied extensively in past years [52, 60, 62, 63]. All the observations so far have been made in the intensity range for which the Keldysh parameter was below unity, i.e. the intensity range is in the tunneling regime. We have selected the intensity at each wavelength to ensure that the range of intensities is well into the tunneling regime which is specified in each panel of

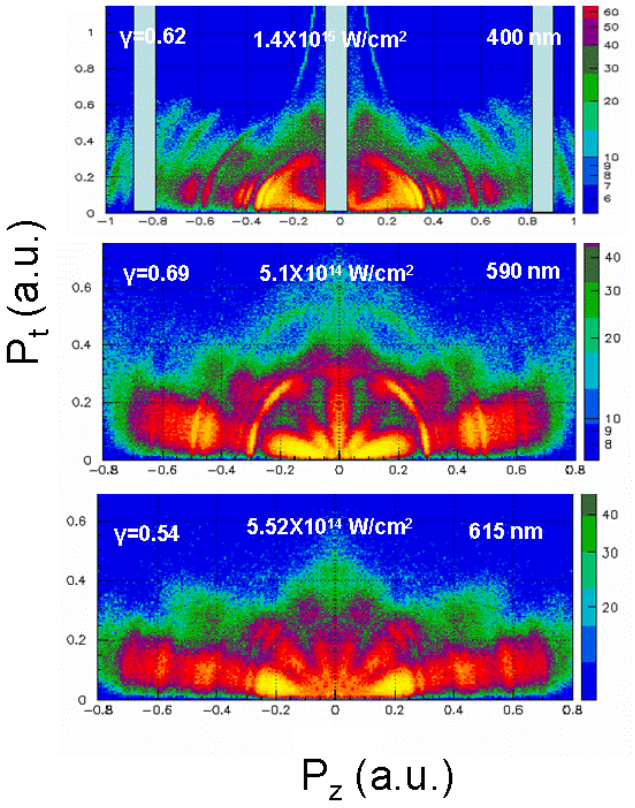

Figure 4.9: Density plots of P_z versus P_t, the electron momenta along and perpendicular to the laser polarization, for different wavelengths (400,590 and 615 nm) on argon. The Keldysh parameter γ, the peak laser intensity and the wavelength are indicated on each panel. The table color is logarithmic.

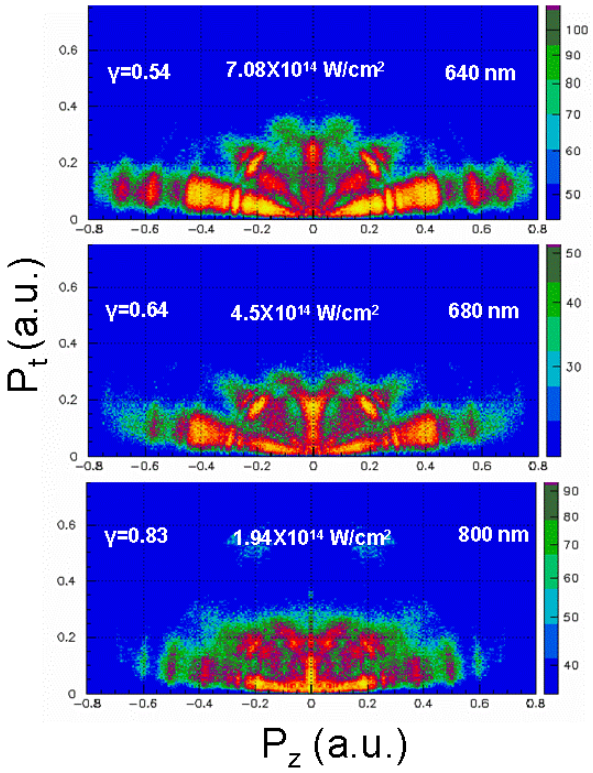

Figure 4.10: Similar to Figure 4.9 but for wavelengths of 640, 680, and 800nm.

spectra as shown in Figures 4.9 and 4.10. The reason for choosing high intensities is to make sure that the observed radial structures associated with the tunneling electrons rather than those released in the multi-photon process [4].

In Figure 4.11 we have plotted the low energy portion of the spectra integrated over the angle for a list of wavelengths. The spectra show evidence for 5g resonance, and possibly other higher 6l-nl Rydberg series above it. These spectra are presented in terms of a binding energy where all the Rydberg series are located at the same position irrespective of photon energy. For each spectrum, the energy of a single photon has been subtracted from the measured electron energy so that the horizontal scale becomes (the negative of) the binding energy. A multi-photon ionization process would occur through the resonant Rydberg state if an additional photon is then absorbed to put the electron into the continuum. The binding energy of the resonant state can be expressed as

$$B.E. = E_{measured} - h\nu \tag{4.8}$$

where $E_{measured}$ is the measured electron energy.

The energy of any resonant state at a particular photon energy can be calculated by

$$E(eV) = h\nu - \frac{13.6}{n^2} \tag{4.9}$$

where $-\frac{13.6}{n^2}$ is the binding energy of the highly excited Rydberg state (n).

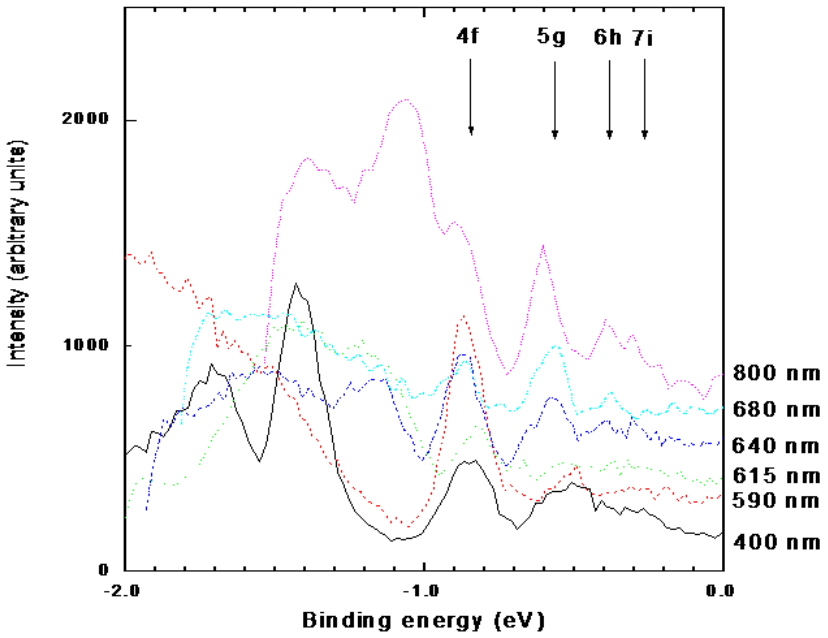

Figure 4.11: Plots of the electron energy spectra, integrated over all the angles, in the region of the first ATI group. The horizontal scale is the electron energy minus the energy of one photon in each case, thus representing (the negative of) the binding energy of the Freeman resonance through which the ionization might be occurring. The positions of several possible active resonant states are shown by vertical arrows above the plot.

This energy should be equal to the measured energy of an electron from any particular resonance. Also the binding energy of these states is the same irrespective of the photon energy used. In addition, a feature centered near the 4f states of argon is seen at a binding energy of

0.86 eV. However, because of the complex level structure of argon in this region we cannot positively identify exact resonances which are active here. Most of these structures are similar to those seen previously in the multi-photon region for argon [52, 63]

Figure 4.12 shows a different representation of the density plot of the momentum images for all wavelengths as shown in the previous Figures 4.9 and 4.10. These plots represent the yield per unit angle versus energy rather than the conventional way of plotting yield per unit solid angle. The former representation gives more resolved angular structure for small theta than the latter one.

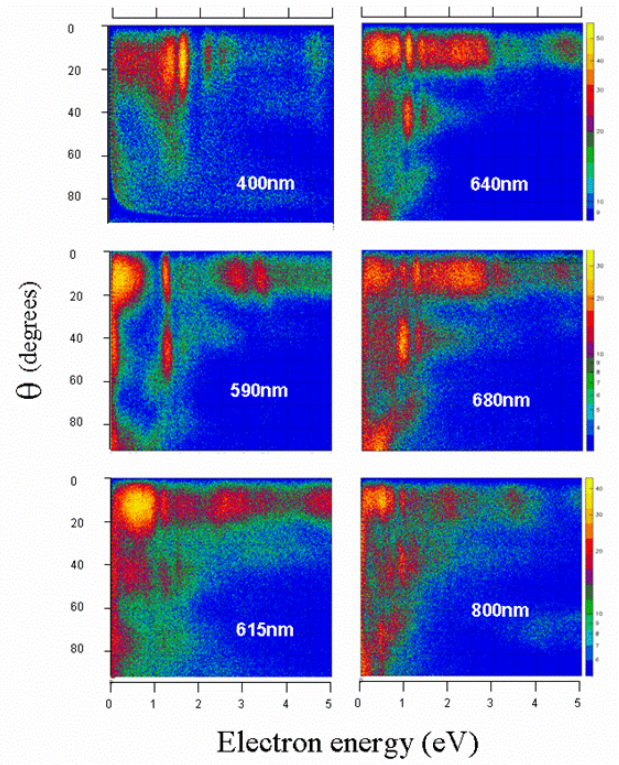

Figure 4.12: Density plot of the angle between the electron's momentum and the laser polarization direction (vertical axis) and electron energy (horizontal scale). These plots are different presentations of data of momentum image from Figures 4.9 and 4.10.

In Figure 4.13 we have shown the projection of the slices of energies from 1.0 to 1.2 eV and 1.2 to 1.5 eV corresponding to the 4f and 5g resonant states onto the angle region. Also,

these experimental plots are compared with the expected distribution for a pure l = 5 partial wave.

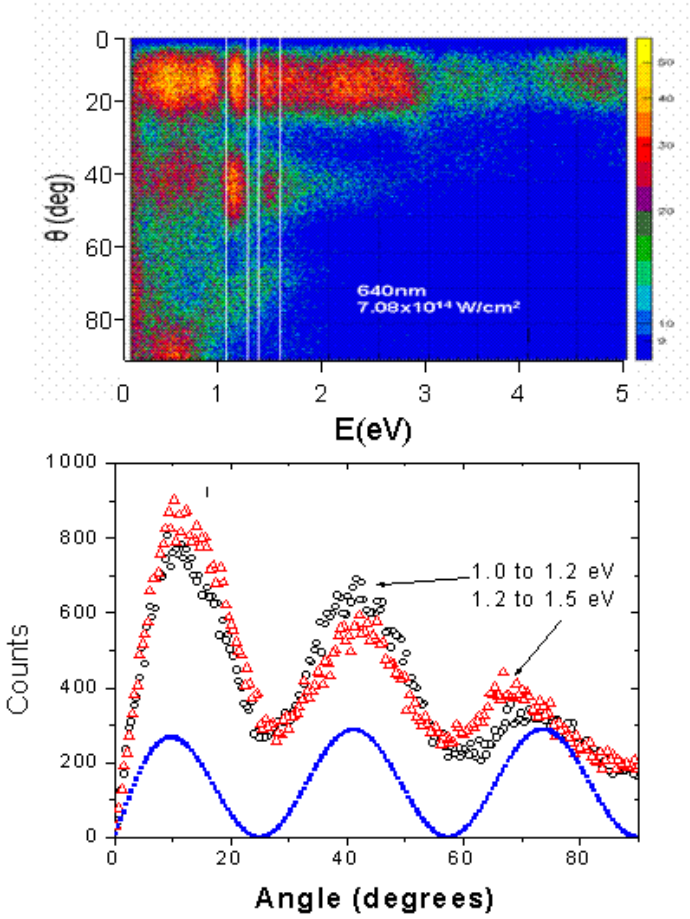

Figure 4.13: The bottom figure shows the projection of the data of the 2D momentum image (upper figure) for 640nm at the intensity 7.08×10^{14} W/cm^2 onto angle axis for selected energy slices. The open circles show a slice from 1.0 to 1.2 (centered on the 4f resonant energy); the open triangles show a slice from 1.2 eV to 1.5 (centered on the 5g and higher Rydberg states). The solid line shows the square of the Legendre polynomial $P_5(cos\theta)$ multiplied by sinθ, which converts the usual intensity per solid angle to intensity per unit angle.

It is seen that the angular distribution of electrons in the continuum is the same for both 4f and 5g regions. This peculiar behavior has been observed not only for the spectrum at 640nm, but also it is the general characteristic of all spectra. Therefore the angular distribution is constant over the range of energies (Figure 4.12), suggesting that angular structure is not relevant to the principle quantum number of a particular resonant state.

4.9 Interpretation of radial pattern observed in momentum space images

The structure of the 2D momentum image could be explained more easily if the intensity of the laser used to generate such a structure is in the multi-photon region. Most of the structure can be definitely explained in terms of well known processes: above- threshold ionization and Freeman resonances. But the structure becomes quite complicated when the intensity regime switches from multi-photon to tunneling. Almost all of our spectra show a complicated angular pattern, which is not so obvious to explain explicitly. Although some of the structures are dominantly governed by the multi-photon processes, the main feature (angular feature) needs more theoretical work to get through the actual process. Let us see how these complex patterns can be understood on the basis of some theoretical models.

4.9.1 Is the complex radial pattern related to the final parity state of the electron in the continuum?

One stream of theoretical work, which is very successful in predicting the correct number of nodes and dominant angular momentum in the low energy region, considers the number of photons absorbed by an electron to transit from ground state to continuum. If we consider only the first ATI and its angular structure, we can explain it by considering the parity rules with the number of photons absorbed by the photoelectron to give rise to the first ATI structure. Such a phenomenon has been successfully explained theoretically by M.Wickenhauser *et al* [6]. For argon, if an electron is released from the atom initially in a 3p state by absorbing a certain minimum number of photons (even or odd number), the angular structure related to the electron in momentum space is determined by the parity of the electron in the continuum. Let us take the specific case of an even number of photons absorbed for the electron to be in the continuum; in this case the parity of the electron will be odd. The reason is straightforward because the electron is initially in a p state (odd parity) and absorbing an even number of photons (even parity) makes the final parity odd. As a result we expect to see an odd number of nodes in the low energy radial pattern.

Furthermore, in order to interpret the dominance of single l in the angular distribution of a low energy electron on basis of the number of photons absorbed by the electron in the

continuum [8], let us consider the initial angular momentum of the electron in a state (p) of the valence orbit of the argon atom. On absorbing one photon, the angular momentum state of electron can switch either to s or d with equal probabilities according to the selection rule of electronic transition ($\Delta l = \pm 1$). If it absorbs one more photon, there can be only one route for s to change it into p; but for d, it can transit either to p or f. If the electron absorbs altogether 5 photons from the initial state p, the electron takes the final angular momentum states s, d, g, i respectively. In this case the l distribution takes the values from 0 to 6. The dominant angular distribution is approximately equal to the average of these two values, and which is equal to 3. In this way we can determine the dominant angular momentum of the continuum electrons after absorbing a certain number of photons. Let us see how this model works in our experimental data. For a given saturation intensity (I_{sat} = 3.3 x10 ^{14} W/cm^2), the minimum number of photons absorbed by an electron to transit into the continuum from the initial state p for a list of observed wavelengths are given in table 4.1. The dominant angular momentum is obtained from reference [8].

Table 4. 1: Comparing the theory and observation of final parity and dominant angular momentum of a continuum electron for a given list of wavelengths.

Wavelength (λ nm)	Photon energy (hv)	Minimum number of photons absorbed	Dominant angular momentum (l) (Theory)	Dominant angular momentum(l) (Experiment)	Final parity theory	Final parity (Experiment)
400	3.1	6	3	3	odd	odd
590	2.1	13	6	4	even	even
615	2	14	5	5	odd	odd
640	1.93	15	6	4	even	even
680	1.82	17	6	6	even	odd
800	1.54	23	8	6	even	even

Even though there is a slight discrepancy between the dominant angular momentum predicted by the theory and the experimental observation for some wavelengths, the final parity states of the continuum electron are well agreed with each other.

4.9.2 Dominance of single l: Is it the effect of long range Coulomb potential on the continuum electron?

A factor which determines the generation of a complex radial pattern in the 2D image is the effect of the long range Coulomb field on an outgoing particle. This fact is similar to that reported by Dimitriu *et al*. [58] in their calculation for the dip at the zero momentum of a singly ionized hydrogen atom. Such behavior of a continuum wave was also predicted by D. Arbó [5]. Their model considers electrons released at close to the maximum field and their subsequent motion due to the combined effect of the laser field and the long range Coulomb field; and quantum interference between the coherent wave packets will lead to the fanning structure in the 2D momentum image. Their results show l = 8 dominate at 800 nm, which supports the dominance of single l in our every observed pattern.

In order to test whether this pattern is relevant to the effect of the Coulomb field or not, most recently Z. Chen *et al.* [8] have reported a similar radial pattern for different wavelengths solving time-dependent Schrödinger equation with and without the Coulomb potential and compared these patterns with the strong-field approximation calculation. They have chosen three different ranges of Coulomb potential i.e. long (infinity), and two short ranges (r_c= 5.a.u., r_c=2 a.u.). The resulting angular pattern was compared with SFA in which the Coulomb potential is not included. They found pronounced radial pattern in the lower energy portion only for the solution with long range Coulomb potential.

The main conclusion of the above discussion is as follows: The tendency for single l (for example l = 5) to dominant is remarkably independent of the resonant state at particular wavelength , and calculation of D. Arbo and Z. Chen supports this as a general property of tunneling ionization at these wavelength in the presence of a Coulomb field.

4.10 Conclusion

Present experimental results show that the lower energy structure which has been observed in the past for longer pulses and low intensities can also survive in high intensities and short pulse. Since all the spectra are averaged over the volume, we cannot rule out that some of the electrons might come from intensities well below the actual peak intensities. By scanning the energy structure over different wavelengths, some of the features can be identified in terms of definite Freeman resonances. The *l* value of in the continuum is not determined by the principle quantum number of the Freeman resonance. The *l* value in the continuum depends on the wavelength and intensity. This is expected because the number of photons needed to reach a given resonance depends upon these factors. The tendency of dominance of a particular angular momentum in our observation is remarkably independent of the resonant state, and the diffraction calculation of Arbo *et al*. [5] supports that this is the general property of tunneling ionization at this wavelength in the presence of a Coulomb field. Most recently, the radial structure in the lower energy electron momentum, and evidence of the Freeman resonances, have been well reproduced theoretically within the framework of the time dependent Schrödinger equation [6, 7, 8]. Our spectra are qualitatively in agreement with these theories.

CHAPTER 5 - Comparison of the angular and energy structure in low energy part of momentum space of electrons ionized from different targets (Ar, O_2, CO_2 and N_2)

5.1 Background

The dominant multi-photon processes such as above-threshold ionization, and intensity dependent and independent resonances have been extensively studied for the intensity range below tunneling ionization using atomic targets, especially noble gases like helium, neon, xenon and argon, for the last several years. However, molecules are much more complex in structure than atoms, and studying the dynamics of electrons released from molecules in a strong field is much more tedious than those released from an atom. It could be easier to study electron dynamics from molecules if this study is made by comparing similar and more relatively simple processes from an atomic target. In this part of the study, we explain some of the angular and energy features of electron spectra from linear molecules (O_2, N_2 and CO_2) by comparing them with similar features observed from atomic targets.

5.2 Comparing the spectral features of Ar, O_2 and CO_2 at 800nm pulses

In order to study whether the angular features of the low energy portion of momentum space depends on the core structure or not, we have chosen three different targets: one atomic target and two linear molecular targets O_2 and CO_2. We explained most of the low energy features of argon in the previous chapter. Here we are going to investigate the same features for molecules. We attempt to find whether the determining factor for these basic features is the structure of the target gas or a property of the laser.

We take our observation at peak intensity which are higher, under these conditions it is approximately true that the major yield of single ionization comes from that part of volume where $I = I_{sat}$. We use this to estimate the number of photons absorbed to account for the resultant parity of the continuum electron. For simplicity, we estimate the saturation intensity out

of the over–barrier intensity as shown in the table 5.1. The over-barrier intensity is uniquely determined by the ionization potential of atom and molecules as described in chapter 2.

Table 5.1 : Calculation of minimum number of photons absorbed for λ=800nm

	Ar	O_2	CO_2
I_p (eV)	15.76	12.56	13.7
I_b (W/cm2)	4.9×10^{14}	1.49×10^{14}	2.8×10^{14}
I_s (W/cm2)	3.3×10^{14}	1.32×10^{14}	1.88×10^{14}
U_p (eV)	19.37	7.73	10.95
n	23	14	16
Final parity	even	even	even

I_p= Ionization potential, I_b= Over-barrier intensity, I_s = Saturation intensity, U_p= pondermotive energy, n = minimum number of photons absorbed by first ATI

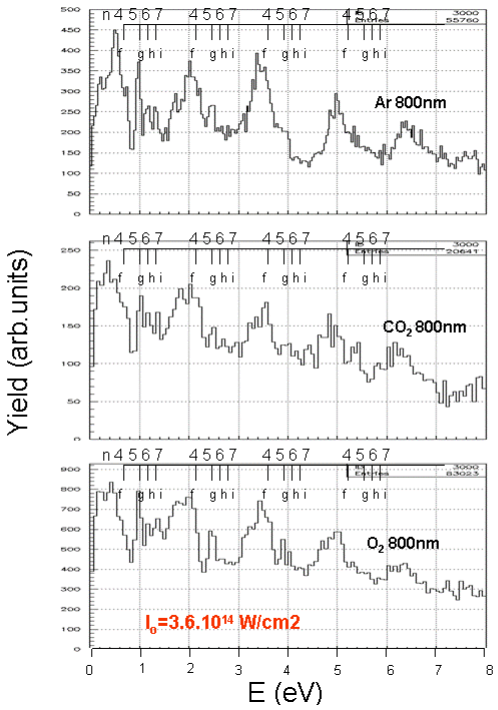

Figure 5.1: Electron energy spectra of Ar, CO_2 and O_2 observed at the same intensity of $3.6\text{x}10^{14}$ W/cm^2 for pulses at central wavelength of 800nm. It is noted that the energy structures are the same for all three targets irrespective of their internal structure. The number with letters in each spectrum indicates the Freeman resonances.

Figure 5.1 shows the electron energy spectra for three different targets. The general feature of the spectra remains the same even though the nature of the targets is different (having different internal structures). The main peaks which are defined as the above threshold ionization peaks clearly show the resonant structures (4f, 5g, 6h, 7i, etc). The exact type and location of Freeman resonances in all three spectra clearly indicate that the highly transient resonant states close to the continuum are almost free from the core potential. The electron in the highly excited state generally "sees" a nucleus with only one proton and will behave much like the electron of a Hydrogen atom.

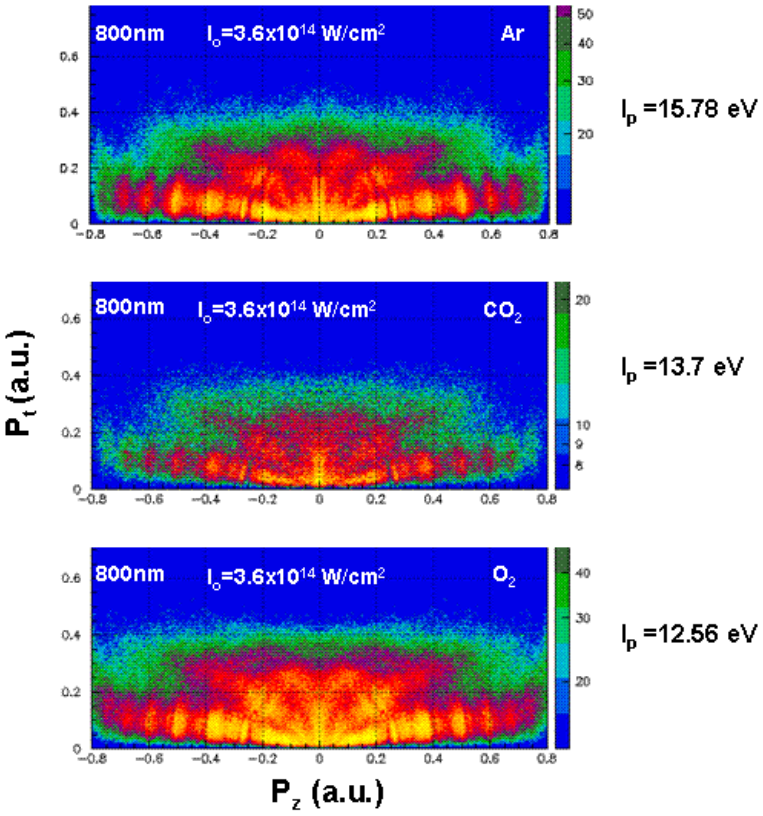

Figure 5.2: Comparing the spectral features of Ar, CO_2 and O_2 for pulses at 800nm observed at the same intensity ($3.6x10^{14}$ W/cm^2). The ionization potential of each target particle is given on the left side of the spectrum.

In Figure 5.2 we compare the momentum space images of electrons ionized from three different targets observed at the same intensity under the same experimental conditions. The

spectral feature observed in the three different cases are similar even though all the targets have entirely different internal structures. If we take a closer look at each spectrum in Figure 5.2, we observe that the fanning structure radially outwards from zero in each spectrum is almost the same irrespective of the nature of the three different target gases. If we look at the angular distribution of the first ATI of each spectrum, we see that each of them consists of an equal number of nodes (4) and anti-nodes (5). The number of angular nodes goes up if we observe higher ATI number. We explained the physics behind these structures in the previous chapter, where we dealt with only the ionization dynamics related to the relatively simpler atomic case.

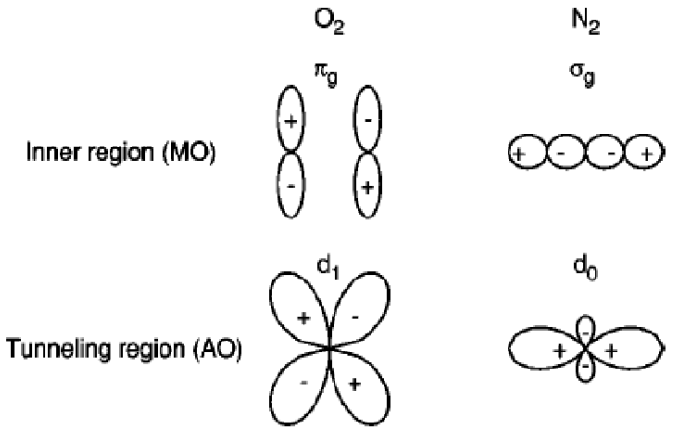

Figure 5.3: Two-centered symmetry (outermost) orbitals of the valence electrons of O_2 (π_g) and N_2 (σ_g) and their closest one-centered atomic orbitals (extracted from [65])

It is also noted that the initial state of the electron in the argon atom is in the p state, but the orbital states of O_2 and CO_2 are different from the p state. For two-center molecules such as O_2, CO_2 and N_2, the outermost orbital of the first two molecules are π_g and the last one is σ_g . But in order to consider the initial state of the electron in these orbits, we need to extract the dominant atomic orbital centered at the charge center of the molecules. Figure 5.3 shows the two-centered molecular orbitals and their closest atomic orbital centered at the mid-points of the

internuclear line. The O_2 valence orbital (π_g) wave function in the outer region is constructed mainly by the two $2p_1$ orbital located at the two nuclei. In terms of the atomic orbital centered at the midpoint of the molecules the wave function is best approximated by the d_1 partial wave or l = 2, m = 1. This is also true for CO_2 molecules. Similarly for the N_2 valence orbital (σ_g), it is defined by the d_o partial wave or l = 2 , m = 0 [65].

Now we estimate the minimum number of photons absorbed by an electron initially in the p state (Ar) and the d_1 state for both CO_2 and O_2 in Figure 5.2. The parities of these states are odd (p state) and even (d_1). The minimum number of photons absorbed in all three targets is found to be 23, 16, and 14 respectively as estimated by using the saturation intensity as the dominant intensity for generation of the lower energy ATIs as shown in the table 5.1. Therefore the parities of the electrons in the continuum would be even for all three cases. We emphasize that parity is the determining factor for the first ATI to have even and odd dominant angular momentum. In Figure 5.1 all three targets have 4 nodes (dominant angular momentum) in the first ATI of the spectra which is very good agreement with the parity rule to determine the dominant angular momentum. The number of nodes is increased by one if we go from the first ATI to the second because one more photon is absorbed and the parity of that ATI becomes odd. Experimentally it is hard to observe full rings (energy ring of constant radius) as the density is much lower in the transverse direction for higher ATI.

5.3 Comparing the spectral features of Ar, N_2, O_2 and CO_2 at 400nm pulses

It should be pointed out here that the spectral features remain the same for all the three different targets, or the pattern seemed insensitive to the core potential for the observation made at 800nm. But once we switch to radiation of double the frequency, the scenario is changed significantly on both the angular and energy pattern in the 2D spectra. Now the spectra of the three different targets show completely different behavior in the momentum image, and these seem to be determined by the core potential as well. Figure 5.4 shows the experimental observation for Ar, CO_2 and O_2 at the same intensity for 400nm as shown in each panel of the Figure. One possible explanation of the difference observed in two different wavelengths might be dominant processes of ionization (multi-photon and tunneling). It is noted that at 400nm wavelength, the intensity needed to attain the low values of the calculated Keldysh parameter (characteristic of tunneling ionization) exceeds the intensity required for complete suppression of

the potential barrier for all the targets. Therefore, multi-photon ionization remains dominant as the intensity increases up to the point of complete barrier suppression, and the tunneling region is never reached [66]. On the other hand, the parity rule to determine the dominant angular momentum of the ATI can still be applied. The first two targets of Figure 5.4 show clearly how the number of nodes observed for the first two ATI is related to the resultant parity of the electron at the continuum. The spectra have been observed at the same intensity, but the dominant intensity for all three different targets is different. Because of the difference in ionization potential of the targets, the minimum number of photons absorbed by electrons of the first ATI of all three cases shows strict differences. The minimum number of photons required for electrons to ionize from the p state of argon and d states of CO_2 and O_2 is shown in Table 5.2.

Table 5.2: Calculation of minimum number of photons absorbed for $\lambda = 400nm$

	Ar	O_2	CO_2
I_p (eV)	15.76	12.56	13.7
I_b (W/cm2)	4.9×10^{14}	1.49×10^{14}	2.8×10^{14}
I_s (W/cm2)	3.3×10^{14}	1.32×10^{14}	1.88×10^{14}
U_p (eV)	4.6	1.93	2.7
n	6	5	6
Final parity	odd	odd	Even

Let us first take argon to explain why it has an odd number of nodes at its first ATI. Initially the electron in the p-state has odd parity, but when it ionizess from there it absorbs at least 6 photons to be in continuum, which will eventually give even resultant parity. A closer look at the spectrum gives more evidence from the nodal structure that the parity of the successive ATI peaks change alternatively odd to even and vice versa. Similarly the initial state of an electron in the valence orbits for both O_2 and CO_2 are in the d_1 state (even parity). Absorbing 5 and 6 photons in each case will give the odd and even parities of the electron in the continuum.

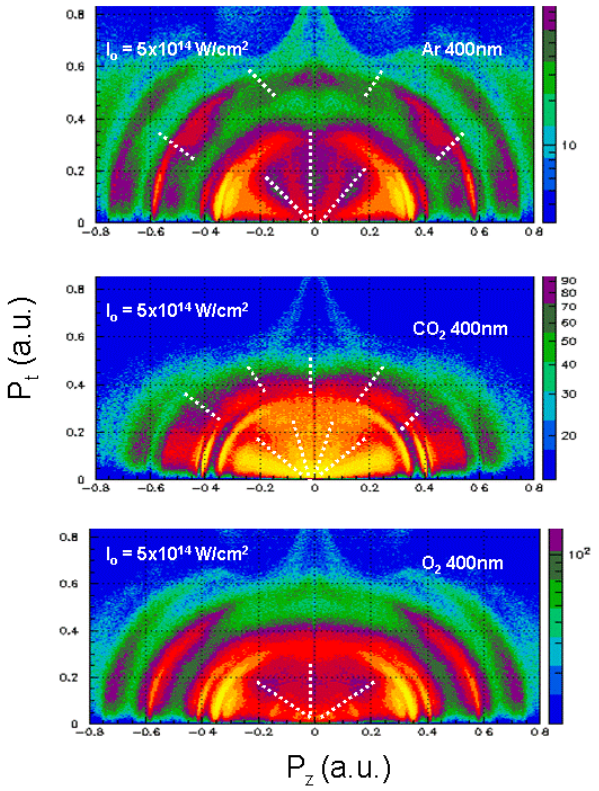

Figure 5.4: 2D plot of the momentum images for three different targets Ar, CO_2, and O_2 observed at the same intensity 5x10^{14} W/cm^2 with pulses of central wavelength of 400nm. The white lines in each spectrum indicate the number of nodes in each ATI peak.

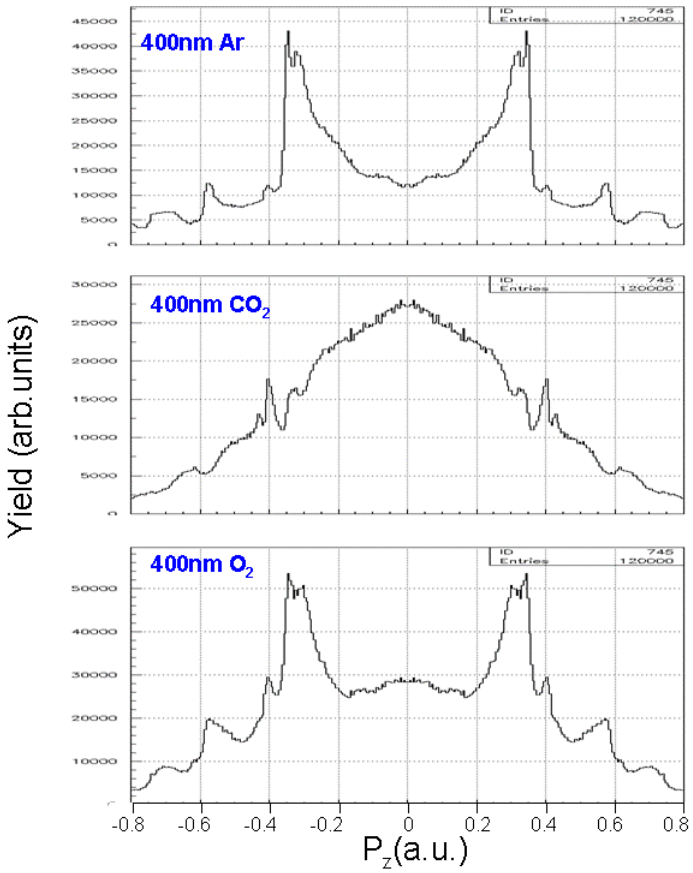

Figure 5.5: The projection of the momentum in Figure 5.4 onto the time direction. The peak in CO_2 and dip in Ar and O_2 are the result of the anti-node and node at $P_z = 0$. These can be alternative ways to check the final parity state of an electron in the continuum.

Figure 5.5 shows the projections of the 2D momentum of Figure 5.5 onto the laser polarization direction (z-direction). The dip at the zero momentum of Ar and O_2 is a consequence of the node at the first ATI in each case; but the anti-nodes in the 2D momentum result in the peak in P_z momentum of CO_2.

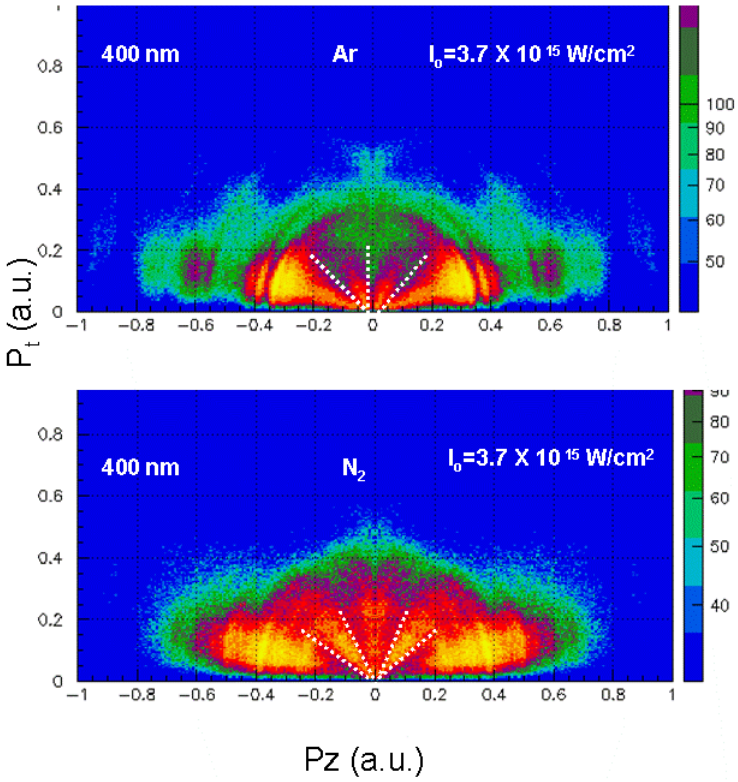

Figure 5.6: Comparing the nodal structure of the first ATI of argon and nitrogen. The difference in the number of nodes in the two cases is the result of different initial states of the electrons (p state for argon and d state for nitrogen).

In Figure 5.6 we have taken the case of two targets (argon and nitrogen) which have almost the same ionization potential. The dominant intensity for these two targets at the focal volume is also nearly equal. The difference in the number of nodes in the two cases is the result of the difference of the initial state of the ground state (p for argon and d_o for N_2) electron even when they absorbed an equal number of photons.

5.4 Conclusion

Thus the spectral features of electrons generated by both atoms and molecules can be understood on the basis of the resultant parity of the electron at the continuum. The minimum number of photons absorbed during the multi-photon process is determined by considering the dominant intensities at the focal volume which supposedly contributed most of the features in the spectra. The number of nodes observed in each spectrum for both atoms and molecules agreed well with the final parity of the electron.

CHAPTER 6 - One dimensional dynamical alignment of O_2 molecules

6.1 Introduction

The study of alignment of molecules has been a growing field of interest in strong field physics for the past several years, as it shows significant potential for technical use in such areas as surface scattering research [67], surface processing [68], and surface catalysis [67]. In addition to these, this phenomenon also suggests a new ability of intense ultrashort laser pulses to control molecular dynamics and its applications to high-order harmonic generation [70,71] and material processing [72].

The interaction of molecules with a laser field can be described completely only if we consider the coupling of the laser to the different degrees of freedom of the molecules: electronic motion, vibrational motion, and rotational motion. The time scales associated with each of these motions are quite different, roughly attoseconds for electronic motion, femtoseconds for vibrational motion, and picoseconds for rotational motion. Therefore, in general, these are weakly coupled. If we are focusing on the rotation of molecules in a weak field, we can almost neglect all the other degrees of freedom.

Unlike an atom, a molecule is not an isotropic system. The ionization of a molecule strongly depends upon the alignment angle between the molecular axis and the polarization direction. The molecular ADK predicts that the ionization rate of a molecule strongly depends upon the symmetry of its outermost molecular orbital [73]. The symmetry of the outermost orbital of nitrogen molecules is $3\sigma_g$, while those of oxygen and carbon dioxide molecules are π_g. Because of this symmetry of the molecular orbital, the ionization rate strongly depends upon the angle between the polarization vector and the molecular axis. For nitrogen this rate is highest when the polarization vector is parallel to the molecular axis. But this is no longer true for O_2 and CO_2 molecules, since they have their nodal plane lying along their molecular axis. For these molecules, the ionization rate is least if the direction of the polarization vector acts along the molecular axis, since the density of electrons in the field direction is small. Because of the butterfly shape of the valence orbit of both O_2 and CO_2, the ionization probability is highest at an angle of about 40^o to the molecular axis [74, 75].

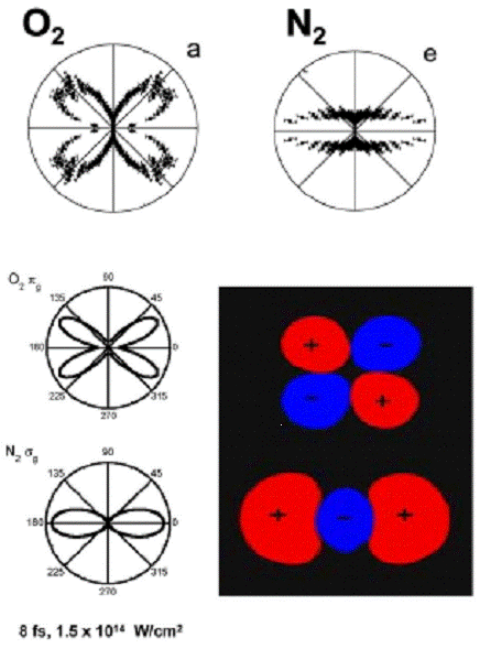

Figure 6.1: The first two figures are the polar plots of the angular distribution for O^+/O^+ and N^+/N^+ detected in coincidence. For O_2, the distribution peaks around 45° to the polarization vector (horizontal direction) and for N_2, it peaks along the polarization vector. The middle and bottom figures are the theoretical prediction (MO ADK). It is noticed that the angular distribution reflects the symmetry of the orbital of each molecules. Adapted from [75]

Figure 6.1 shows the polar plots of the angular distribution of coincident fragments O^+/O^+ and N^+/N^+ produced by double ionization of molecules in a rescattering process. It is seen that the distribution for O_2 peaks around 45° to the polarization vector, whereas it peaks along the polarization vector for N_2. The angular distributions for both molecules are observed to be in good agreement with the predictions of molecular ADK theory. They reflect clearly the outermost orbits of their molecules (structure of valence orbit of O_2 molecules and N_2 molecules). Obviously, this is a way to observe the valence orbit of simpler molecules without aligning them in the space using a short pulse.

It is now a well-established fact that molecules in the gas phase align rapidly with the laser polarization direction when they are subjected to strong laser pulses. In this chapter we present an alternative approach to map the molecular orbit by looking at the angular structure of

the electrons ionized from the aligned molecules. We first give the theoretical background of molecular alignment briefly. Particularly, we will emphasize the dynamical field-free alignment of linear molecules like O_2 (also see the alignment of CO_2 in Appendix C) induced by a short pulse which changes their J state population. In the second part of the chapter, we focus on how to generate the aligning and probing pulses experimentally. The third part explains the experimentally observed revival structure of the O_2 molecule. The fourth part of this chapter focuses on the angular distribution of electrons. Electrons ionized from the valence orbits of molecules exhibit information on their orbital structure. The underlying goal of this experiment is to see the imprint of the outermost orbit of a molecule on the angular distribution of electrons ionized from aligned molecules.

6.2 Brief theory

6.2.1 Adiabatic or non-adiabatic alignment

Molecules can be aligned adiabatically or non-adiabatically by laser pulses depending on the duration of the aligning pulse compared to the rotational period of the molecule. For the long pulse limit ($\tau_{pulse} >> \tau_{rot}$), the molecules are pushed to align adiabatically (i.e. molecules orient themselves in the direction of the field during the pulse) with their most polarizable axis along the laser polarization direction. They transiently populate the pendular states in the laser field during the pulse, and return to the original field-free state upon the adiabatic turn-off of the laser field, ending the alignment [76, 77]. On the other hand if the duration of the pulse is shorter compared to the rotational period of the molecules ($\tau_{pulse} << \tau_{rot}$) , the pulse imparts a "kick" to the molecules that rapidly transfers a large amount of angular momentum to the system and gives rise to an alignment that sets in only after the pulse is turned off [77]. Non-adiabatic alignment can be viewed as a sequence of rotational Raman transitions. Each Raman cycle is limited by the selection rules of a pure rotational Raman transition. To understand the kick model classically, let us consider a randomly aligned ensemble of molecules in space under the action of the electric field of the pulse. A molecule which has a large initial angle to the field experiences a large torque and will rotate with higher angular momentum than a molecule oriented at a smaller angle to the field. At an angle of zero faster molecules catch up with the slower molecules and

the maximum alignment is achieved. Afterwards, the molecules keep rotating with different velocities and the alignment is destroyed.

If we neglect the electronic excitation and rovibrionic couplings, the rotational motion of the molecules can be described by a rigid rotor model [78]. The total wave function Ψ can be expanded in terms of rotational eigenstates $|JM\rangle$ of the field-free Hamiltonian H_o, whose corresponding energy eigenvalues are given by

$$E_J = BJ(J+1) \tag{6.1}$$

where J is the angular momentum quantum number and M is the laboratory frame z-axis projection. The interaction between the linear polarized pump pulse and a linear molecule is through an induced electric dipole moment describable in terms of the effective angular potential energy

$$V = -\left[\frac{\varepsilon(t)^2}{2}\right]\left(\alpha_{\parallel}\cos^2\theta + \alpha_{\perp}\sin^2\theta\right). \tag{6.2}$$

Here ε(t) is the electric field of the laser pump pulse, θ is the angle between the electric field and the inter-nuclear axis, and $\alpha_{\parallel}, \alpha_{\perp}$ are the components of the anisotropic polarizability for fields respectively parallel and perpendicular to the axis. The anisotropic polarizability property of molecules makes it favorable to align them in the direction of the electric field under the action of the laser pulse.

6.3 Experimental method

A Mach-Zehnder interferometer was used to split an input pulse of 30fs into pump and probe pulses to introduce a relative delay; and the two beams were then recombined collinearly. Figure 6.2 shows a schematic of the interferometer for such a purpose. The input pulse was split by a beam splitter (R=50% and T=50% for S polarization) before passing through the pump and probe arms of the interferometer.

Before making the delay between the pump and probe pulse, it is important to make sure that these two beams are overlapped spatially and temporarily. We adjusted the beam size of the aligning beam with an iris, insuring that the volume occupied by the pump pulse was larger than that of the probe as shown in Figures 6.3 and 6.4, since we wanted most of the fragments after

ionization come from the targets within the focal volume. That is, we probe only those molecules which have been exposed to the alignment field.

Moreover, a larger focal spot size gives a lower intensity, and we adjust the iris size until the intensity of the pump is just enough to align the molecules of particular interest without ionizing them. The aligning pulse keeps the same polarization as the input polarization (vertical polarization) before splitting, but the polarization of the probe pulse can be controlled by the combination of achromatic half and quarter wave plates.

To observe and control the revival structure of the molecules, we used a circularly polarized

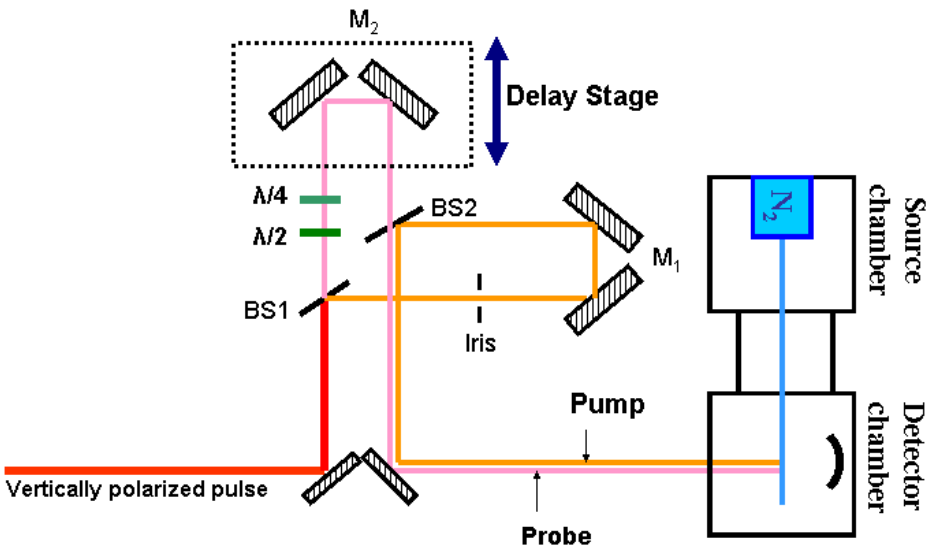

Figure 6.2: Schematic of the Mach-Zehnder interferometer. The first beam splitter (BS1) splits the input pulse into two parts: pump and probe pulses. The two beams meet at the second beam splitter (BS2) after traversing stages M1 and M2. The beam size of the pump can be controlled by adjusting the diameter of the iris on the path of the pump beam. The pump beam keeps the same polarization as the input, but the polarization of the probe beam can be controlled by the combination of half wave (λ/2) and quarter wave plates (λ/4). Once the temporal and spatial overlapping of two collinear beams is achieved, the delay between two beams can be set by adjusting the position of the delay state (M1).

probing pulse and a vertically polarized pump pulse. This polarization of the probe pulse was then switched to linear (horizontal) for the measurement of the electron distribution from the

aligned molecule. Typical beam sizes of both the probing and aligning beams were 6mm and 2.5 mm, which produced focal sizes 6.3 μm and 15 μm. Both pump and probe beams were focused collinearly into a gas jet by a parabolic mirror.

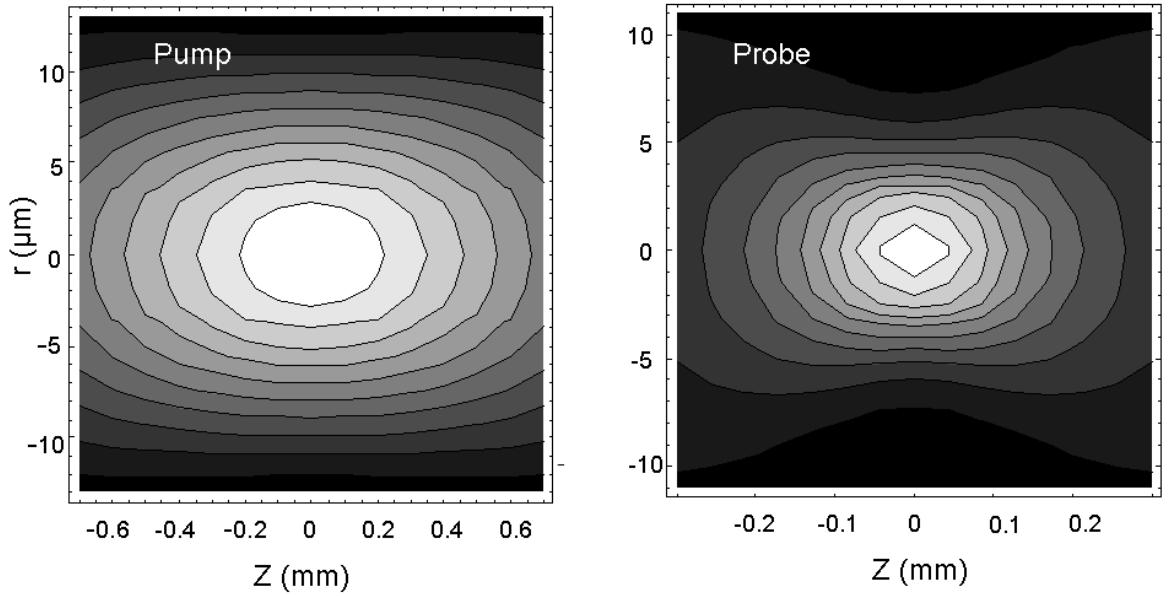

(a) (b)

Figure 6.3: The graphical plot of the focal area of the pump and probe beams. (a) Plot of the focal area calculated with the beam diameter in the far region 2.55 mm at the peak intensity of 8.8×10^{13} W/cm^2. (b) Focal area of the probe beam: beam diameter of 6 mm and 3.14×10^{14} W/cm^2. These typical spot sizes of the beam were actually used in the experiment of the effect of alignment of oxygen molecules on the angular distribution of electrons. It is noticed that the spot size in the far region is larger for smaller beam size and confines the probe focal volume within the pump volume to ensure that all molecules get ionized by the probe within the pump volume.

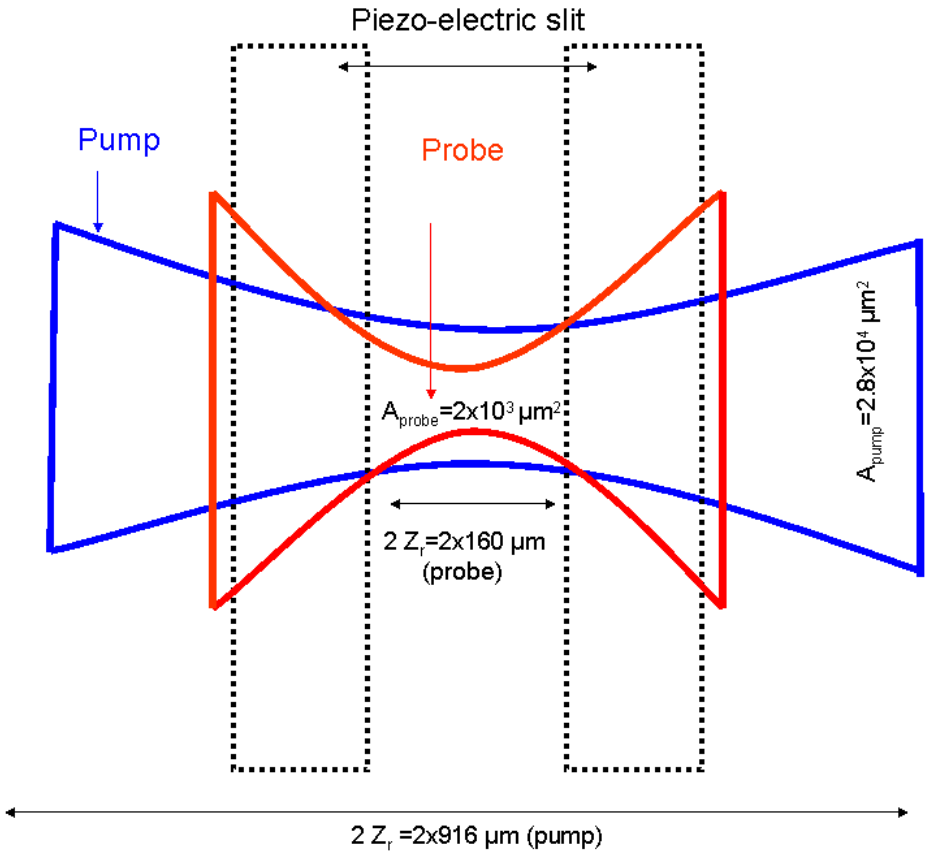

Figure 6.4: Sketch of focal area of the pump and probe beams with beam diameters of 2.55 mm and 6 mm respectively. The confocal parameters and area of the pump and probe focus were calculated using their beam size. The figure also shows how the slit width can be adjusted so that the molecules get ionized at the center part of the focal area of the probe. The slit can control the size of the jet only in the z-direction, not in the transverse direction.

Both pump and probe beams were focused on the target jet by the parabolic mirror inside the chamber. We employed a high value of the spectrometer field (55 V/cm) for determining the revival structure, making the field strength enough to collect the exploding doubly charged fragments. The field was reduced to 2 V/cm for the electron experiment which was just enough to collect electrons having energy up to 10eV, initially directed away from the detector. All the electrons directed to the detector were well collected. A magnetic field of strength of about 8 G was superimposed on the electric field to collect the electrons with energy up to ~22.5eV directed transverse to the spectrometer axis.

6.4 Observing and controlling rotational revival structure of linear molecules

In order to control the alignment of the molecules, we first have to be able to observe the rotational revival structure. In this experiment, a weak vertically polarized (aligning pulse) pulse of 30fs created a wave packet that showed macroscopic field-free (non-adiabatic) molecular alignment at well-defined time delays. The subsequent time evolution of the wave packet was observed using the strong circularly polarized exploding pulse. At each particular time delay, the molecules are ionized to multiple charge states by the exploding pulse and undergo rapid dissociation. For the linear molecules under consideration, the initial velocities of the fragments become parallel to the molecular axis if the dissociation process is very rapid. Measuring the dissociating products from higher charge states (double or triple charge states) through Coulomb explosion will thus provide direct snapshots of the orientation of the molecules at a particular delay.

If the pulse is much shorter than the rotational period of the molecule, the interaction between the short pulse and the molecule can be thought of as an impulse and described by the kick model. Assuming the molecular axis is frozen during the interaction (within the duration of the pulse as the rotational period is much less than the pulse duration), the wave function at time zero can be expressed as

$$\psi(t=0) = \sum_J a_J \left| JM \right\rangle . \tag{6.3}$$

The wave function is expressed as a superposition of field-free states with well-defined angular momentum and projection. After the pulse is turned off, the molecular wave function continues to propagate in free space. The time dependent wave packet is given by

$$\Psi_g(t) = \sum_J a_J e^{-i\left(\frac{E_J}{\hbar}\right)t} \left| JM \right\rangle . \tag{6.4}$$

From the uncertainty principle, a narrow angular distribution requires broader distribution of angular momenta. However, it requires the condition that all of them should interfere constructively. After the kick, the wave packet evolves freely. The phases of the different rotational states are proportional to the rotational energy and time. As we show below, because the phases of different rotational states are quantized, they sum up coherently at the rotational time period T of the molecule. The alignment of molecules at this time is said to undergo full

rotational revival. The angular distribution at this time again peaks preferentially parallel to the laser polarization direction.

Around revival times, the phase factors of all component wave functions in the wave packet have advanced by the same amount modulo 2π, and therefore the wave function near the end of the aligning pulse interaction is restored. This occurs as follows: The phase difference between two component wave functions in the wave packet that differ by N rotational quanta is equal to

$$\begin{aligned}\Delta\varphi(J+N,J) &= (2\pi Bct)\left[(J+N)(J+N+1)-J(J+1)\right] \\ &= (2\pi Bct)\left[2NJ+N+N^2\right]\end{aligned} \tag{6.5}$$

For diatomic molecules, ΔJ =0, 2, the dominant phase can be expressed as

$$\Delta\varphi(J+2,J) = 2\pi Bct\left[4J+6\right] \tag{6.6}$$

Since the expression in brackets is even for any value of J, it follows that a full revival of the wave packet takes places whenever

$$2\pi BcT_{rev} = \pi \ . \tag{6.7}$$

which leads to

$$T_{rev} = \frac{1}{2Bc}, \tag{6.8}$$

where $B = \dfrac{\hbar^2}{2\mu R_o^2} = \dfrac{\hbar^2}{2I_o}$.

The full revival period of N_2, O_2 and CO_2 molecules are estimated as about 8ps, 12ps and 42.7 ps respectively.

Halfway towards the revival, at

$$\frac{T_{rev}}{2} = \frac{1}{4Bc}, \tag{6.9}$$

the phase difference between two component wave functions in the wave packet is given by

$$\Delta\varphi(J+2,J) = \frac{\pi}{2}\left[4J+6\right]. \tag{6.10}$$

Similarly, a quarter revival occurs at

$$\frac{T_{rev}}{4} = \frac{1}{8Bc}, \tag{6.11}$$

and the phase difference between two component wave functions in the wave packet is given by

$$\Delta\varphi(J+2,J)=\frac{\pi}{4}\left[4J+6\right] \tag{6.12}$$

$$\Delta\varphi(J+2,J)=\frac{\pi}{2}\left[2J+3\right]. \tag{6.13}$$

6.4.1 Alignment factor for measuring the degree of alignment

Experimentally we observed the field free evolution of the rotational wave packet created by the aligning pulse by Coulomb explosion of O_2 at successive time delays after the aligning pulse. For each target we measured the complete time-dependent $\left\langle \cos^2\theta \right\rangle$ distribution in a plane defined by the circularly polarizing probing pulse, where θ is the angle between the direction of the polarization and molecular axis as shown in Figure 6.5. We used a vertically polarized pulse for aligning the molecules

Let p_{xr}, p_{yr}, and p_{zr} be the three components of momentum gained by a doubly charged fragment during the explosion. Then the cosine for θ in the Y-Z plane is given by

$$\cos\theta=\frac{P_{yr}}{\sqrt{p_{yr}^2+p_{zr}^2}}\ , \tag{6.14}$$

where θ is the angle made by the molecular axis to the direction of the aligning pulse (Y direction). The average of $\cos^2\theta$ measures the degree of alignment of the molecules.

For an isotropic distribution in a plane of circular polarization, we can set $p_{yr} = p_{zr}$; then

$$\left\langle \cos^2\theta \right\rangle = 0.5 \tag{6.15}$$

Thus for an isotropic distribution of molecules, one expects to see the baseline of the $\left\langle \cos^2\theta \right\rangle$ distribution at 0.5, but we found the baseline of the experimental data to be slightly higher than the expected value. This shifting of the baseline $\left(\left\langle \cos^2\theta \right\rangle > 0.5\right)$ can be understood as a result of incoherent alignment [81]. It should be pointed out that the average value $\left\langle \cos^2\theta \right\rangle$ goes to 1/3 if we take the three dimensional distribution of molecules in space.

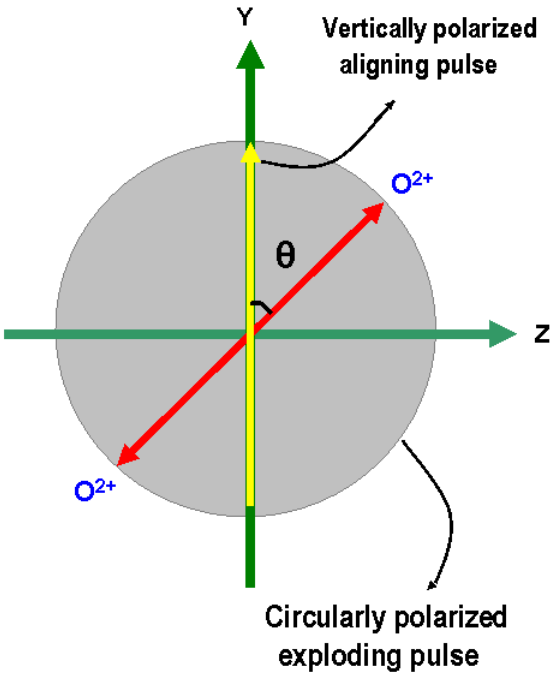

Figure 6.5: Schematic of the polarization of aligning and probing pulses. The aligning pulse is directed along the y axis and the circularly polarized probing pulse is lying in the y-z plane.

For perfect alignment of molecules, $P_{zr}= 0$, then

$$\left\langle \cos^2 \theta \right\rangle = 1 \tag{6.16}$$

Similarly for the ideal anti-alignment case $P_{yr}=0$

$$\left\langle \cos^2 \theta \right\rangle = 0 \tag{6.17}$$

Therefore the larger the value of $\left\langle \cos^2 \theta \right\rangle$ of the distribution indicates the higher degree of alignment of molecules and vice versa.

6.4.2 Revival Structure of O_2

The main objective for reproducing the fractional rotational revival structure of O_2 is to have direct information on alignment before doing any electron experiment, since there is no direct way to observe *in situ* the alignment of molecules with the electron signal alone. Although we can activate both electron and recoil detectors at the same time, it is hard to produce any Coulomb explosion yield in the range of intensities of the electron experiment of particular interest.

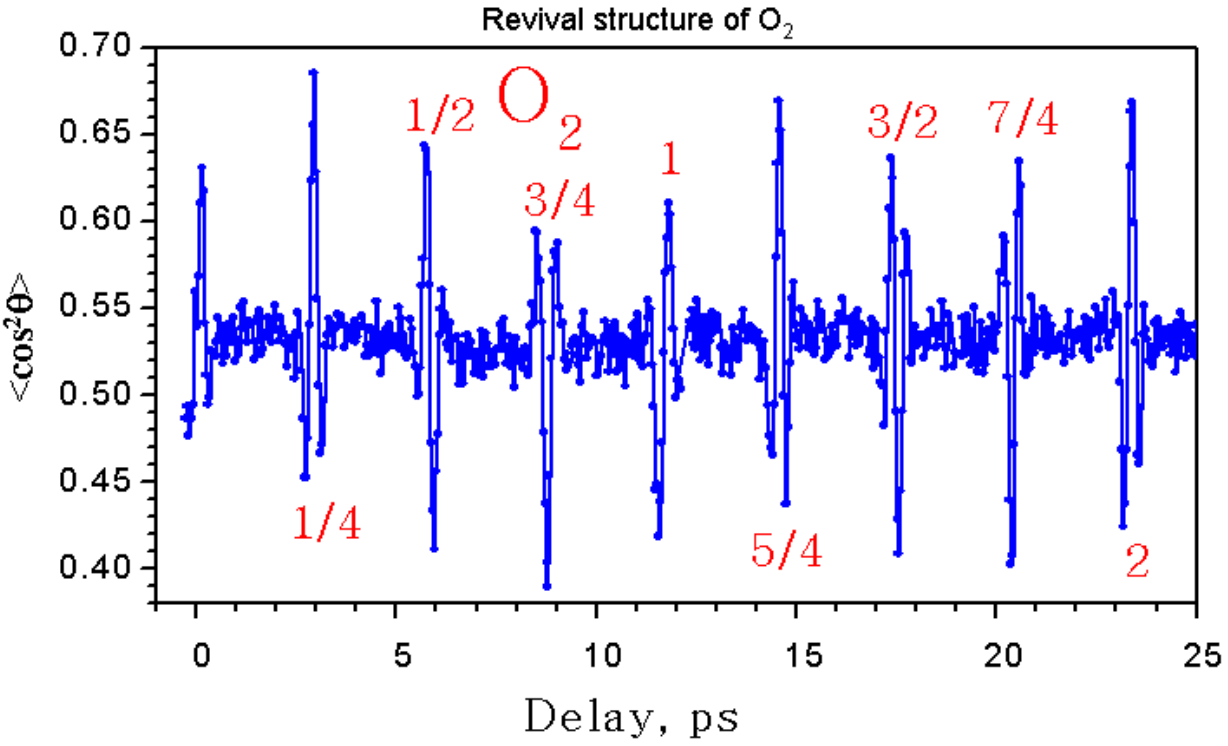

Figure 6.6 : Rotational revival of O_2 measured over a long time range by I. Litvinyuk *et al.* The revival structures such as half, quarter and full revivals can be seen repeatedly. Adapted from [82]

In Figure 6.6 we show a long-time scan of $\langle \cos^2 \theta \rangle$ measured by Litvinyuk *et al.* [82] using the O^{2+}/O^{2+} Coulomb explosion. Our measurement of the same quantity near the quarter

revival and half time is shown in Figures 6.7 and 6.8. It is noticed that the amplitudes of alignment and anti-alignment are significantly higher (0.77) and lower (0.43) than those observed by I. Litvinyuk *et al*. The reason for the improved contrast is that we used more collimated and cooled jets than that used in reference [82]. The contrast between alignment and anti-alignment is also dependent on the intensity of the aligning pulse. Finally, the apparent

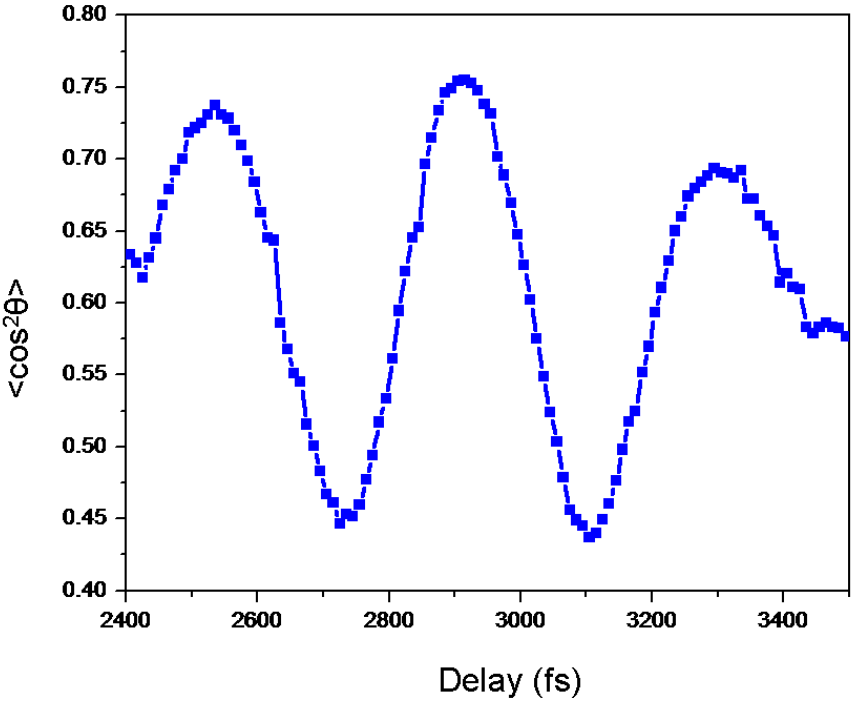

Figure 6.7: Rotational quarter-revival structure of O_2 observed in this experiment using O^{2+}/O^{2+} channel. Pump intensity (I_o) = 1.x 10^{14} W/cm^2, probe intensity (I_o) = 5.7 x 10^{15} W/cm^2. The oscillation is likely due to the fact that the pump laser forces the molecules into alignment so strongly that the molecules start to oscillate with respect to the laser polarization [80].

degree of alignment depends upon the choice of the Coulomb explosion channel used to calculate θ (angle between the polarization vector and molecular axis). The experimental observations presented above are correlated with the number of rotational levels in the molecules that are coupled by Raman transitions during the pump pulse. For low pump intensity only a limited number of rotational states are coupled and therefore weak alignment is observed. For higher intensities, the number of rotational levels that are coupled increases and therefore the alignment becomes stronger.

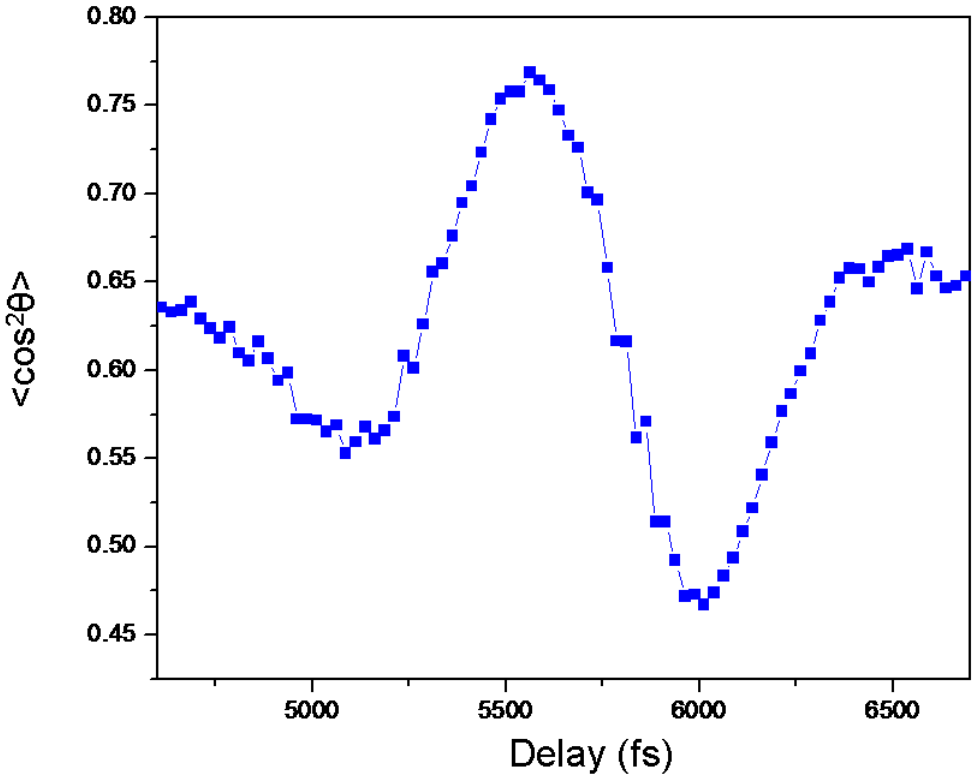

Figure 6.8: Half-revival structure of O_2. Pump intensity (I_o) = 1. $\times 10^{14}$ W/cm^2, probe intensity (I_o) = 5.7$\times 10^{15}$ W/cm^2.

6.4.3 Comparing the quarter revival structure of O_2 with warm and cold jet

We have studied the rotational revival structure at two different temperatures in order to find the dependence of alignment on the temperature of molecules. For this particular measurement, the intensity of the aligning pulse was reduced significantly lower than those measured in the previous two cases (Figure 6.7 and Figure 6.8). In this topic, the gas jet which expands from room temperature (293K) through the nozzle before the skimmer is referred to as a warm gas. At first, the revival structure was measured with a warm jet under specific experimental conditions. Then the jet was cooled down to a temperature just above the condensation point of oxygen (90.20K) before expansion through the gas nozzle, by bathing a delivery tube in liquid nitrogen. The temperature during cooling was monitored by a

thermocouple connected to the line. Figure 6.9 shows the quarter revival structure of O_2 measured at two different temperatures. The calculation of θ was done by taking the O_2^+/ O_2^+

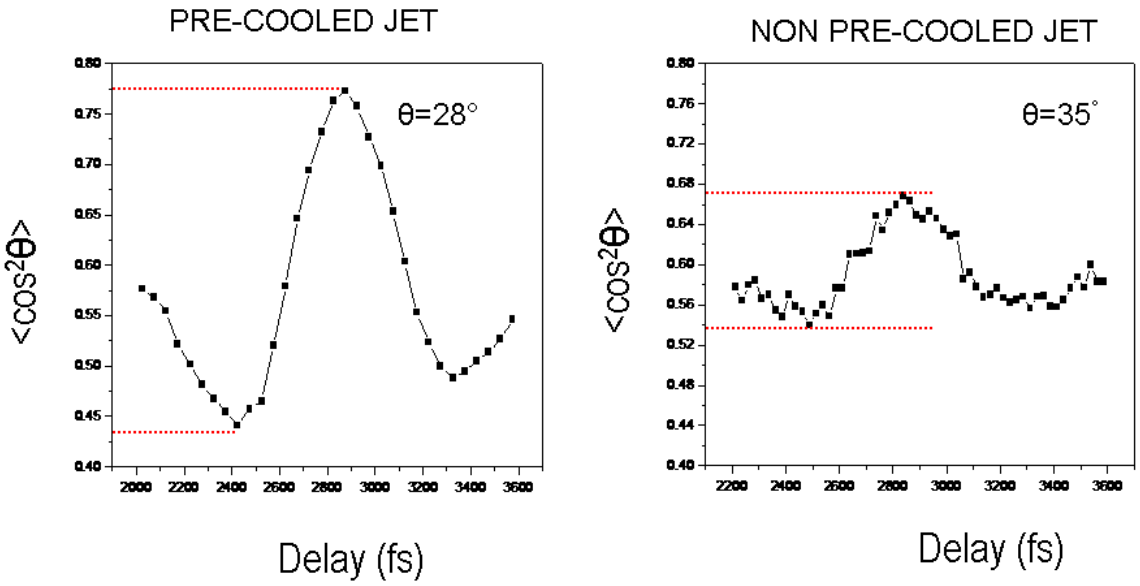

Figure 6.9: Comparing the quarter revival structure of oxygen at room temperature (left) and temperature close to the liquid boiling point of oxygen (right). Pump intensity (I_o) =8×10^{13} W/cm^2, probe intensity (I_o) = 2×10^{15} W/cm^2

fragmentation channel with a window over the TOF of O^{2+}. The width of alignment and anti-alignment peaks in both cases remains almost the same irrespective of the temperatures but a noticeable difference of amplitude as well as baseline can be observed for these temperatures. If we compared the quarter revival structure of the O_2 for the cold and warm jets, it is clearly noticed that the amplitudes (0.775 for alignment, 0.43 for anti-alignment) of the revival structure obtained from the cold jet are found to be elevated to higher values compared to those obtained from the warm jet (0.67 for alignment, ~0.54 for anti-alignment and ~0.59 isotropic). At low

temperature the molecules are distributed more sharply along the field direction. At low temperatures, we expect a lower population of thermally excited initial J states, as compared to the population of those excited by the aligning pulse. The best aligned states are the ones with the lowest J values, and it is crucial for the achievement of alignment that the temperature is as low as possible.

6.4.4 Comparing the quarter revival structure of O_2 for different fragmentation channels

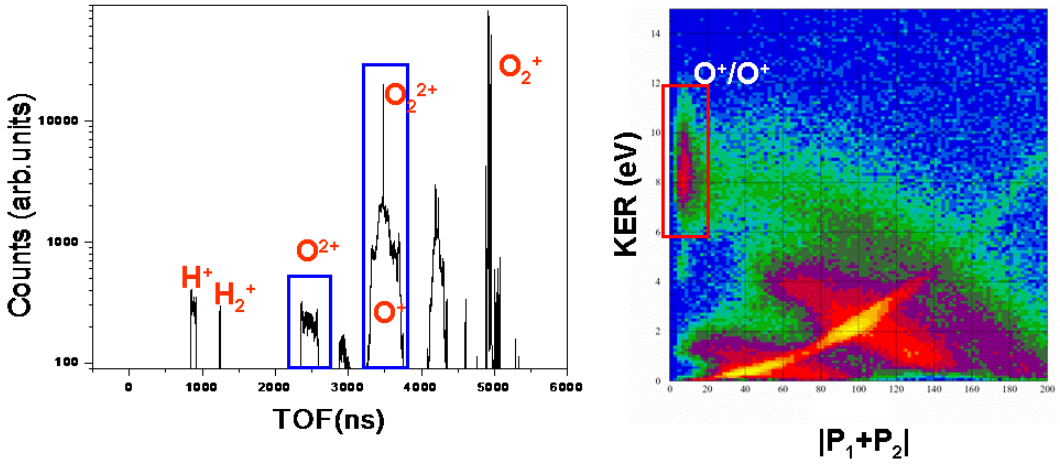

Figure 6.10: The TOF of O_2 (left) and the KER vs. sum of vector momenta of O^+ and O^+ (right). The windows over TOF of O^{2+}, O^+ and coincidence spectra were used to select the two channels of fragmentations to calculate the revival structure. Experimental parameters: Electric field = 55.1 V/cm, flight distance = 24cm, pump intensity (I_o) $=8\times10^{13}$ W/cm^2, probe intensity (I_o) = 2×10^{15} W/cm^2

As we have mentioned already, the degree of alignment strongly depends upon the intensity of the aligning pulse as well as the temperature of the jet (rotational temperature of molecules). The windows over two different channels for calculating θ are as shown in Figure 6.10. In Figure 6.11 we show the three revival curves calculated using different Coulomb

explosion channels. Obviously, the higher charge channel gives a better contrast than the lower one. The probable reason for this is that higher charge states are produced at the peak of the probe pulse, which is also spatially overlapped with the most intense part of the pump beam. Thus the aligning pulse is stronger here. Moreover, the higher charge state fragment dissociates more rapidly so there will be less chance to disturb the alignment by rotations of the molecule during the dissociation.

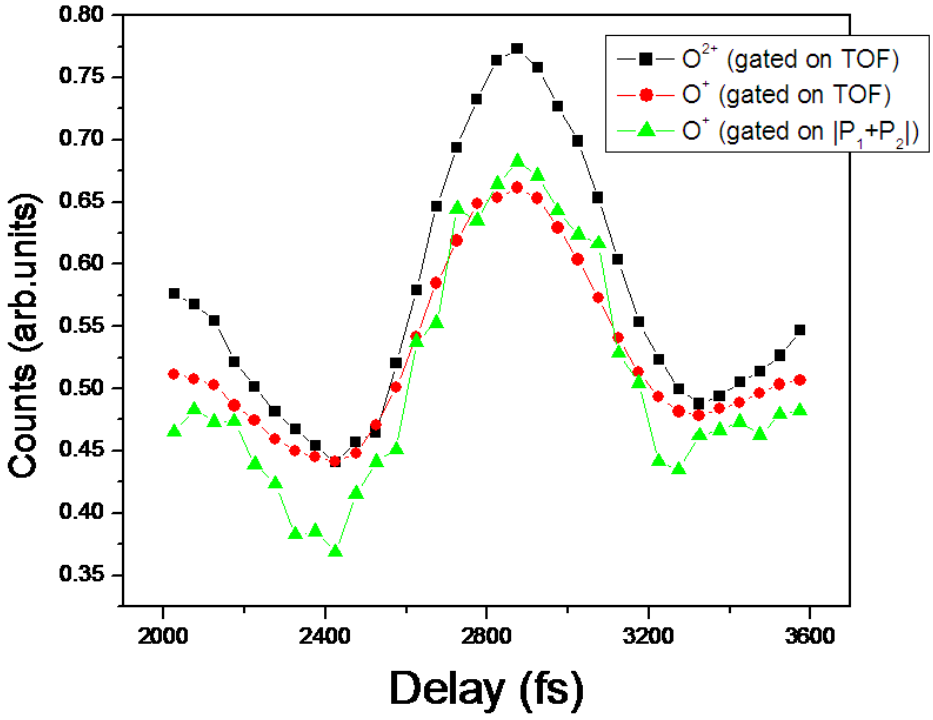

Figure 6.11: Quarter revival cycle of O_2. The black curve was estimated with O^{2+}/O^{2+} channel whereas the red and green curves were measured with O^{+}/O^{+} with windows over TOF of O^{+} and coincidence spectrum ($|p_1+p_2|$) as shown in Figure 6.12 . Measuring the revival structure with two charge states is an indirect way of presenting them at two different intensities of the aligning pulse. Pump intensity (I_o) = $8x10^{13}$ W/cm^2 and probe intensity (I_o) = $2x10^{15}$ W/cm^2.

The degree of alignment could be improved by increasing the intensity of the aligning pulse but the maximum alignment thus obtained is limited by the onset of ionization of

molecules in the strong laser field. To produce a higher degree of alignment without ionization of molecules, it has been proposed to use the multi-pulse method in which the alignment is created with the initial pulses, and then distribution is brought to a higher degree of alignment by subsequent pulses [83, 84]

For the non-coincident channels we cannot rule out the possibility of contribution of O^{2+} and O^{+} from background (H_2O) to the time-of-flight spectrum. Therefore we can expect that the true alignment is higher than what we deduce from these channels. It is always good to estimate the revival structure with a condition over the coincident spectrum. However, the coincident spectrum suffers from having fewer counts and thus a larger statistical scatter in the data.

6.5 The angular structure in momentum space images of electrons ionized from aligned O_2 molecules

6.5.1Basic idea

Is it possible to observe the molecular orbit from the angular distribution of electrons ionized from aligned molecules in the momentum image? The basic idea behind the experiment is to map the orbital structure of the molecule using the molecules own electrons. Therefore, the molecules are aligned into a space by a weak pulse, and then subsequently ionized by another pulse polarized transverse to the molecular axis. The two pulses are separated by a well-specified delay. The momentum image of the electronic wave packet tunneled from the aligned molecule is measured in the continuum. We seek evidence of the angular structure of the initial orbital in the momentum space image of the emitted electrons.

It is obvious from the partial rotational revival structure that the exact position (i.e. delays between pump and probe) of alignment and anti-alignment of the molecules can be easily known. Experimentally we used the recoil distributions to measure the degree of alignment as a function of the pump/probe delay, and then switched to the electron experiment without changing any characteristics of the aligning pulse. For the recoils, we used a vertically polarized aligning pulse of intensity 8×10^{13} W/cm^2 and a circularly polarized exploding pulse of intensity

2×10^{15} W/cm^2 to generate the rotational revival structure of O_2 molecules. When we switched to the electron experiment, the polarization of the probe pulse was changed to linear horizontal, and also its intensity was lowered until it produced single ionization only. We scanned the same time range (2020 to 3620fs) during the electron experiment as we did while generating the quarter revival structure, but we took larger steps of 100fs.

6.5.2 Experimental result

Figures 6.12 and 6.13 show the momentum space image of electrons ionized from the aligned oxygen molecules in the x-y plane. These images were generated by choosing particular delays in the revival structure corresponding to the alignment and anti-alignment of O_2 molecules. Since alignment of the molecules produces a very small effect on the momentum distribution of electrons ionized from both the aligned and anti-aligned case, it is very hard to see any noticeable difference between the spectral features of these two direct spectra. However, by taking the ratio of momentum images obtained for these two molecular alignments, we are able to isolate modulation due to alignment. In Figure 6.14 (an expanded version is shown in Figure 6.15), it is noticed that there is a strong effect observed for electrons having energy between 0 and U_p (the corresponding values of momentum are about 0 and 1 a.u.). A clover-like structure is observed in the momentum range between 0 and 1 a.u in the ratio spectrum.

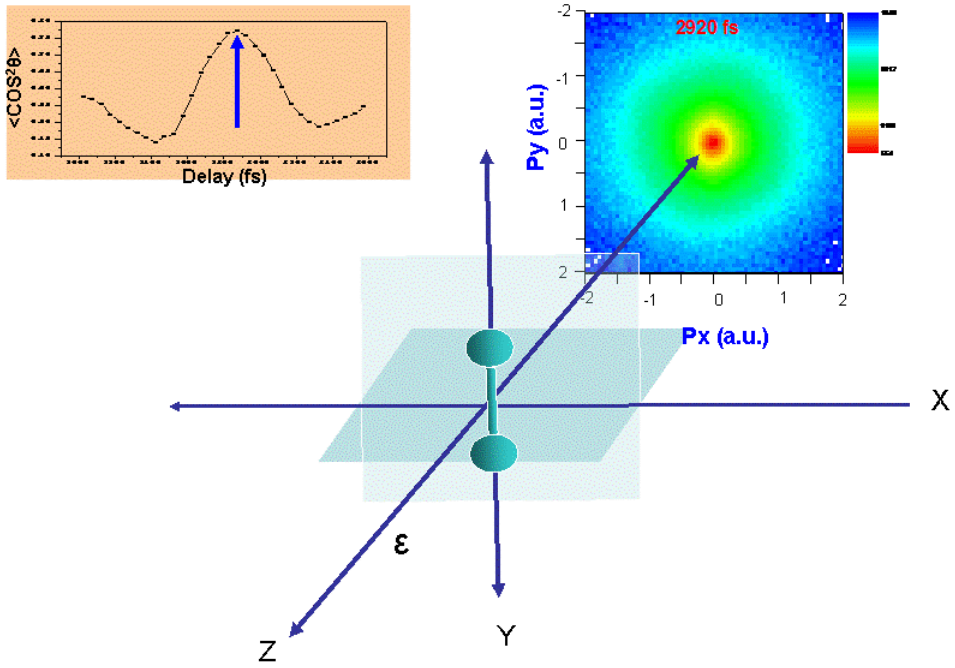

Figure 6.12: The momentum space image of electrons ionized from the aligned molecules in the x-y plane perpendicular to the polarization vector. The inset on the left hand side is the quarter revival structure of the O_2 molecules and the arrow indicates the particular delay between pump and probe pulse for observing the momentum image as shown in the figure. The molecule was aligned along the y-direction and the ionizing beam was polarized along the z-direction. Pump intensity (I_o) = 8×10^{13} W/cm2, probe intensity (I_o) = 2.7×10^{14} W/cm^2

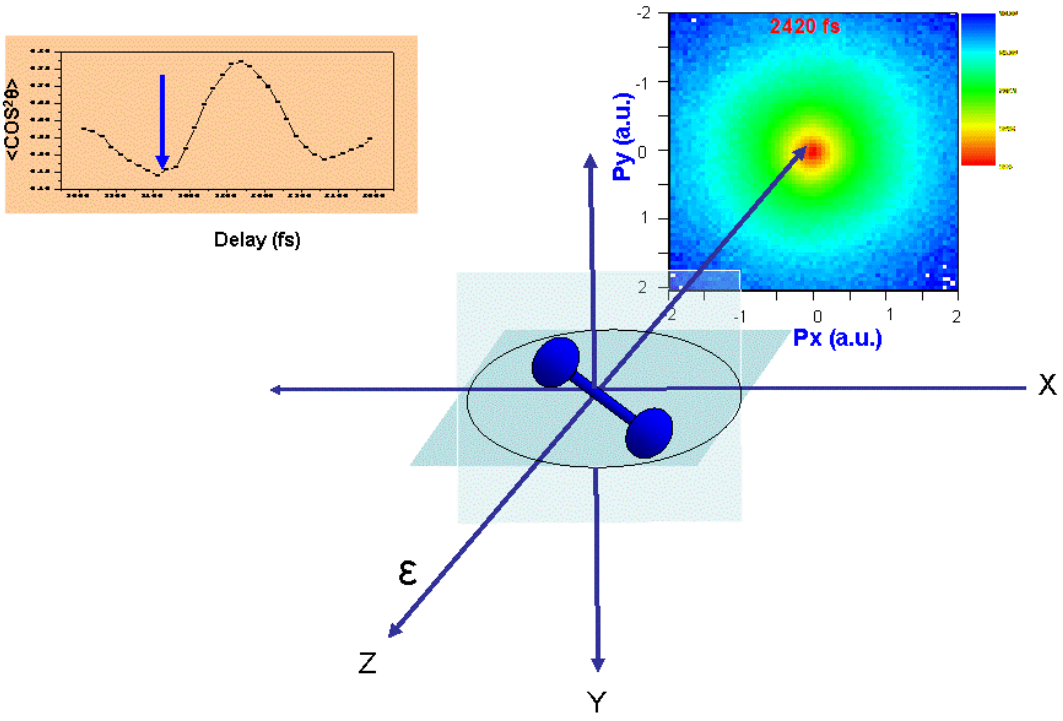

Figure 6.13: Similar to Figure 6.12, but the molecules were anti-aligned (molecules were oriented in the plane perpendicular to the alignment direction). The arrow in the revival structure indicates the position of delay for anti-aligning the molecules. Pump intensity (I_o) = 8×10^{13} W/cm2, probe intensity (I_o) = 2.7×10^{14} W/cm^2

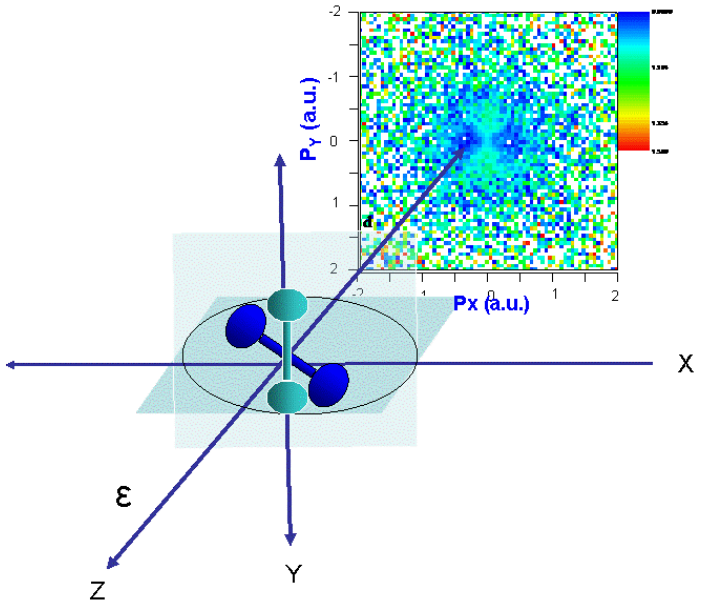

Figure 6.14: The momentum space image of electrons obtained by taking the ratio of images of Figure 6.12 and 6.13. The low energy structure in the spectrum is the filtered image of the transverse momentum in the initial orbital. Pump intensity (I_o) = 8×10^{13} W/cm2, probe intensity (I_o) = 2.7×10^{14} W/cm^2

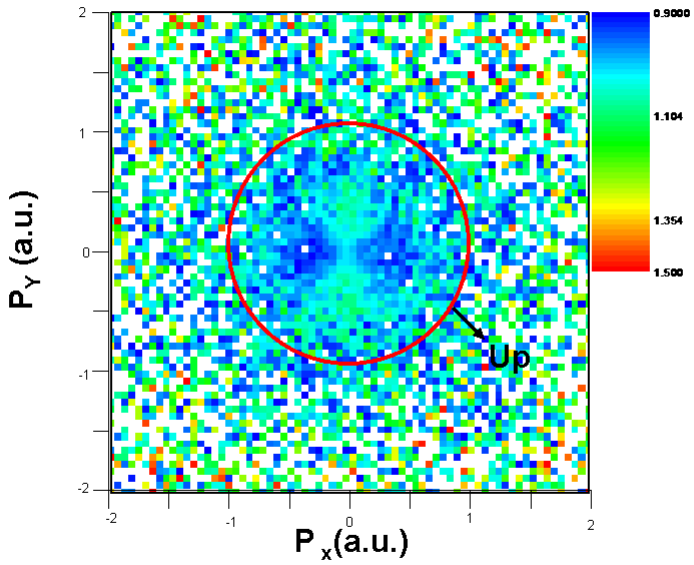

Figure 6.15 : The momentum image of the electron ionized from an aligned O_2 molecule. The low energy structure in the image is within the range of 0 and U_p i.e. the structure is due to the population of direct electrons. Pump intensity (I_o) = 8×10^{13} W/cm2, probe intensity (I_o) = 2.7×10^{14} W/cm^2

A qualitative interpretation of this clover-like structure is the following. Since the molecules are aligned along the y-direction, and the ionized beam polarized in the z-direction perpendicular to the plane of the molecular axis, then a very narrow saddle point region is expected to form in the probe direction through which the electrons of valence orbit tunnel out. An electron wave packet coming out of the valence orbit normal to the molecular axis sees a very narrow opening before spreading in the lateral direction. For each moment of tunneling ionization t_o, the newly created electronic wave packet in the continuum $\Delta\Psi(p_\perp, t_o)$ depends on the transverse momentum $p_\perp$ as [85]

$$\Delta\Psi(p_\perp, t_o) \propto \langle p_\perp \mid \Psi_i \rangle \exp\left(-\frac{p_\perp^2}{2}\tau_T(t_o)\right) \tag{6.20}$$

Here t_T is the tunneling time and can be related to the γ parameter by

$$\omega\, t_T(t_o)\cos\omega t_o = \gamma \tag{6.21}$$

The Gaussian shape due to tunneling filters the Fourier transform $\langle p_\perp | \Psi_i \rangle$ of the initial orbital Ψ_i which already carries the imprint of the orbital's π_g structure. As shown schematically in Figure 6.16, this structure gives rise to the clover-like structure in the observed continuum wavepacket. Because the experiment aligns the orbital only in the y-axis, not in the x-y plane as shown in the figure, the momentum space image has to be averaged over all azimuthal angles of the orbital with respect to the y-axis, which weakens the contrast of the image. Furthermore, the molecular alignment is not complete, and averaging over the cone angle of the molecule with respect to the y-axis also occurs. Nevertheless, the general characteristics of the initial orbital can be observed in the data.

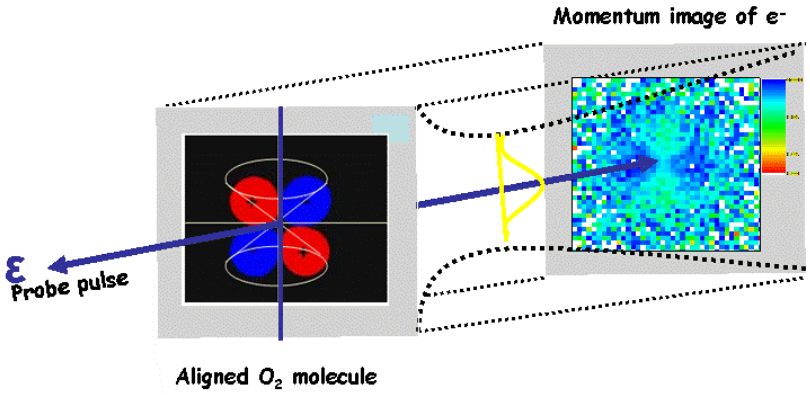

Figure 6.16: Showing how the angular structure of the momentum space image of the electron ionized from the aligned O_2 molecules carries information about the original orbital structure of the O_2 molecules. The low energy structure in the spectrum is the filtered image of the transverse momentum in the initial orbital. Pump intensity (I_o) = 8×10^{13} W/cm2, probe intensity (I_o) = 2.7×10^{14} W/cm^2

In Figures 6.17 and 6.18, we look on the low energy structure with windows over different ranges of electron energy. The value of pondermotive energy (U_p) is 17eV for probe intensity 2.7×10^{14} W/cm^2, which is about 1 a.u. of momentum. The low energy structure appears very pronounced if we set a window over the electron energy between 0 to U_p (p_z =0 -1 a.u). We expect the structure due to the population of direct electrons without subsequent rescattering to the ion core. However, the structure gets degraded in the region between U_p and $2U_p$ (p_z= (1-1.5) a.u). This is the mixed region where both direct and re-scattered electrons contribute to the population of the momentum distribution.

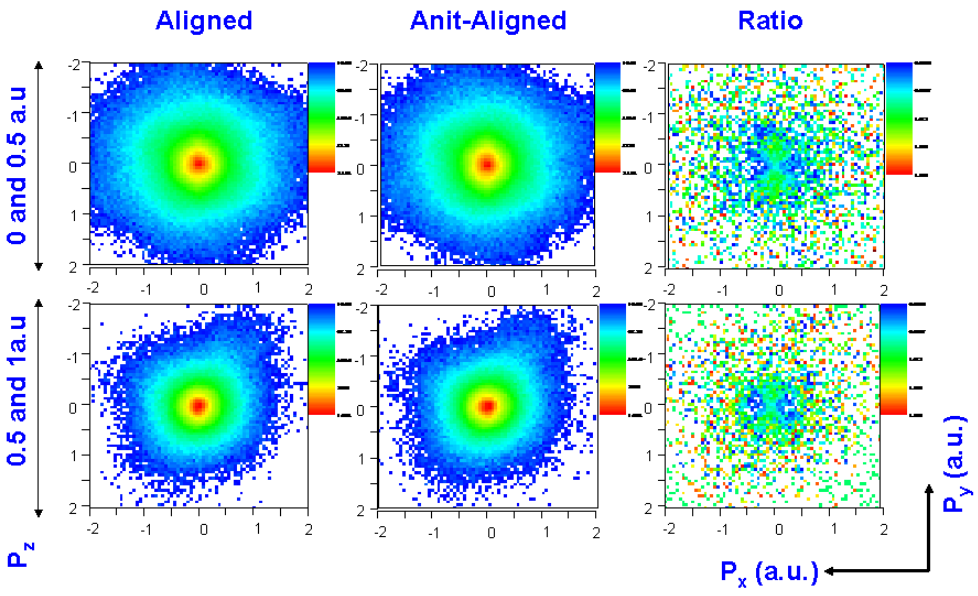

Figure 6.17: The momentum image of an electron on the azimuthal plane with the windows over the P_z. The range of windows are between 0 and 0.5U_p, and 0.5 and U_p of the electron energy, which clearly indicates that the lower energy structure is due to the population of direct electrons without rescattering to parent molecules. Pump intensity (I_o) = 8×10^{13} W/cm^2, probe intensity (I_o) = 2.7×10^{14} W/cm^2

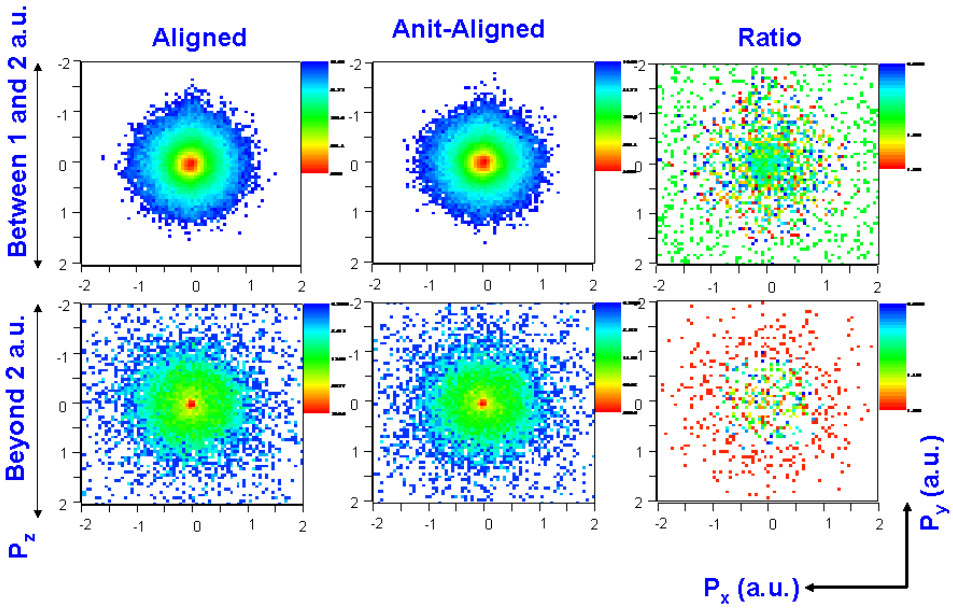

Figure 6.18: The first row is spectra observed with windows of p_z for mixed energies (direct and re-scattered), whereas the second row is observed only with the range of re-scattered energies. Pump intensity (I_o) = 8×10^{13} W/cm^2, probe intensity (I_o) = 2.7×10^{14} W/cm^2

Beyond 2U (p_z > 1.5 a.u.) the population in the momentum distribution is contributed mainly by re-scattered electrons, and the structure due to direct electrons completely disappears.

We produced a number of spectra (Figures 6.19 to 6.24) selecting different delays between pump and probe pulses from the quarter revival structure. Each spectrum was generated by taking the ratio of the spectrum at a particular delay (for example at 2820fs) to the spectrum in the isotropic region (2020 fs). The main purpose for producing these spectra is to see how the different orientations of the molecules affect the lateral spreading of momentum of the tunneling wave packet. In addition to this, we can also observe the effect of alignment as well as anti-alignment of molecules. If we fix the probe polarization vector, and watch the momentum space image of the electrons ionized from different orientations of molecules, it keeps changing the distribution alternatively according to the aligned, isotropic, and anti-aligned orientations. The amount of spreading of the electron wave packet in lateral directions depends on how narrow the

saddle point region is, and it is determined by the orientation of the molecule. As a result we observe a distinct low energy structure when the molecules are oriented normal to the polarization vector, but this structure disappears at the other orientations. The clover structure is more pronounced at a delay (2920 fs) corresponding to the highest observed degree of alignment, and later the structure is found to be rotated by 90^{o} for a delay (3420fs) corresponding to anti-alignment.

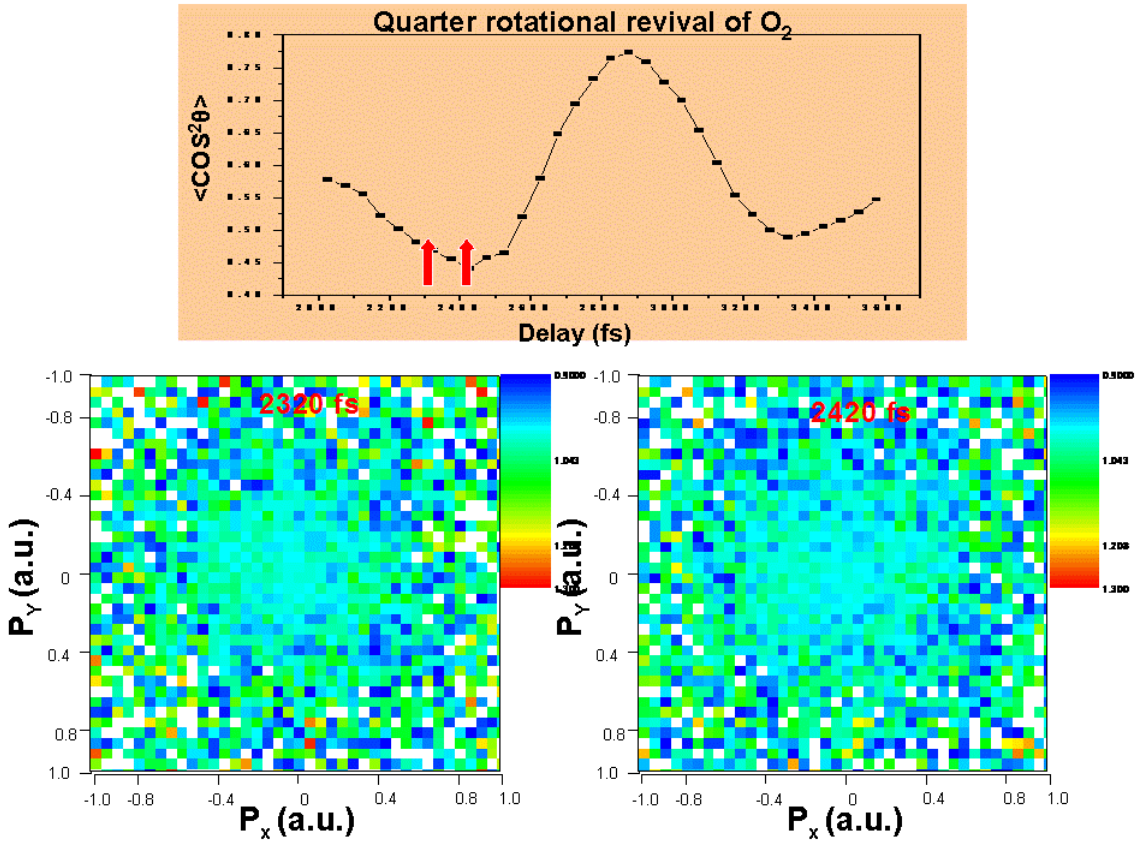

Figure 6.19: The momentum space images of electrons observed at delays (2320 fs and 2420 fs) close to the anti-alignment peak of rotational revival as shown by arrows.

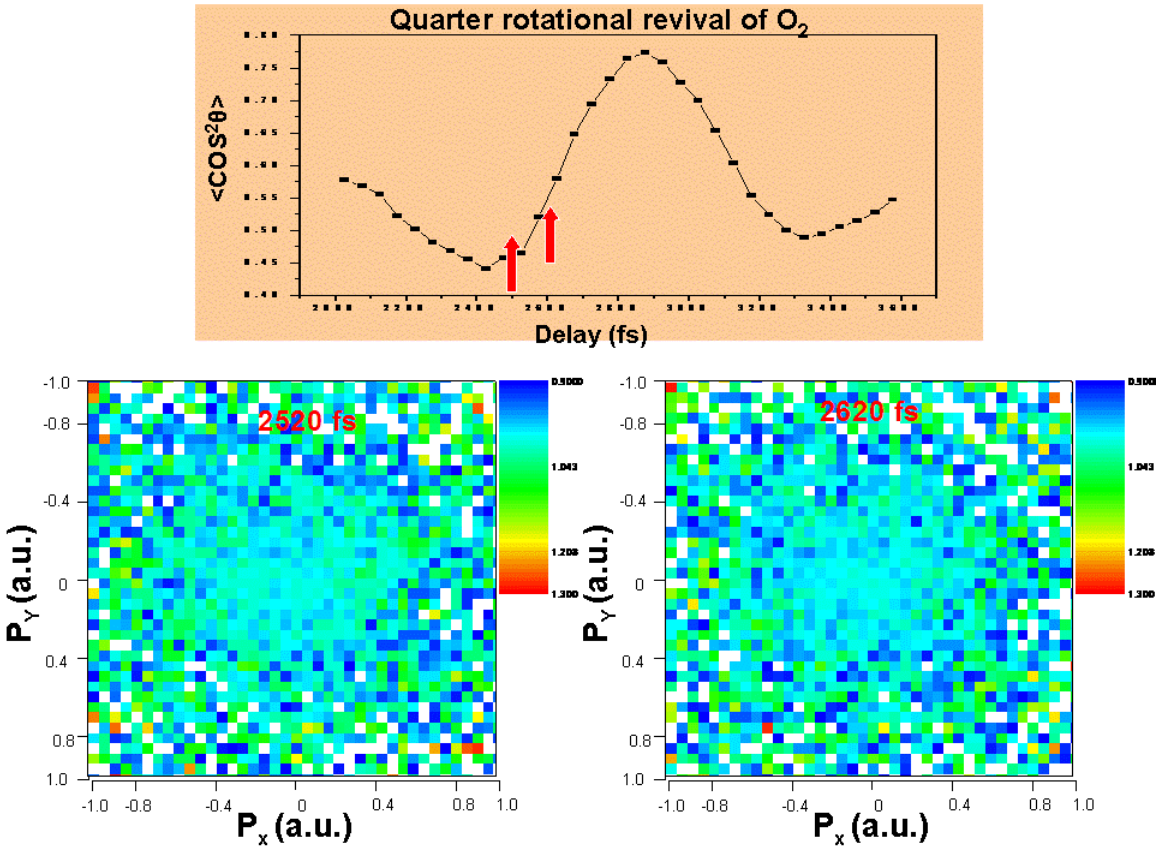

Figure 6.20: Momentum images of electrons generated at delays 2520 fs (close to anti-aligned peak) and 2620 fs (close to the isotropic).

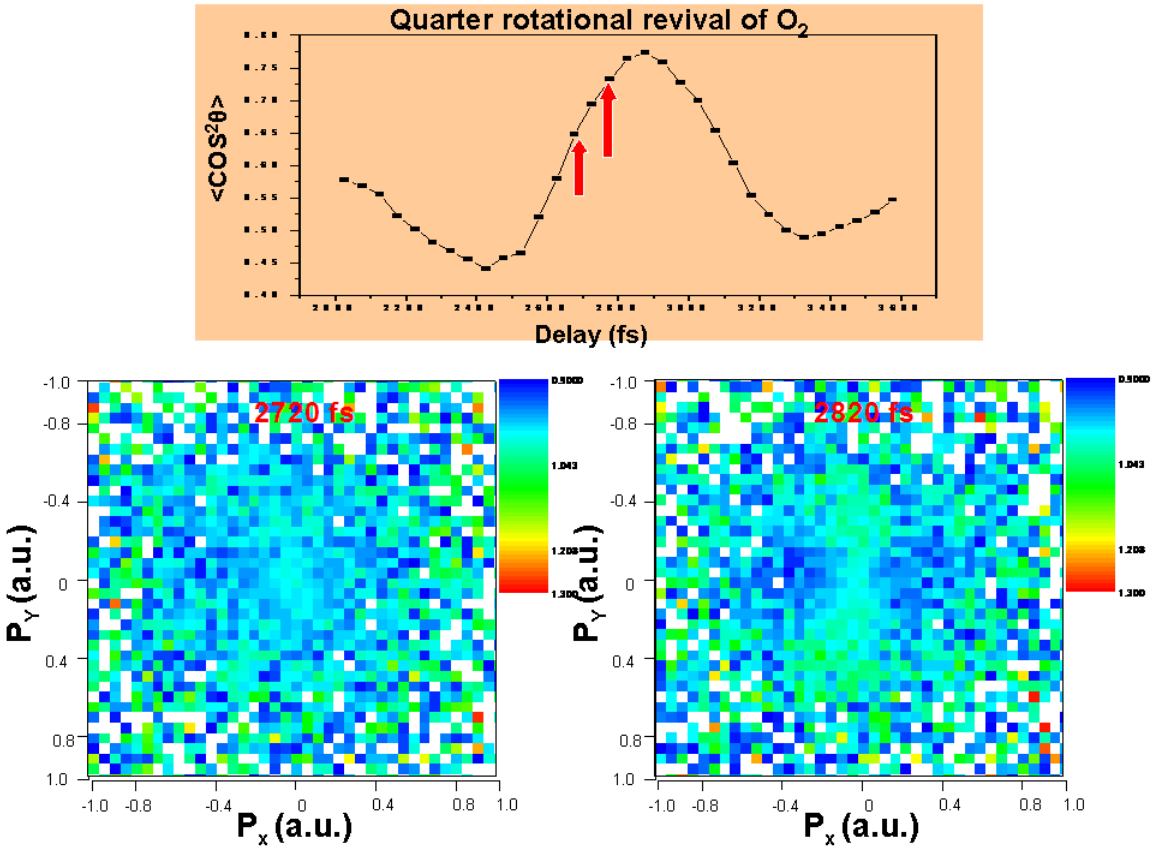

Figure 6.21: Momentum images observed at delays (2720 fs and 2820 fs) closer to the aligned peak.

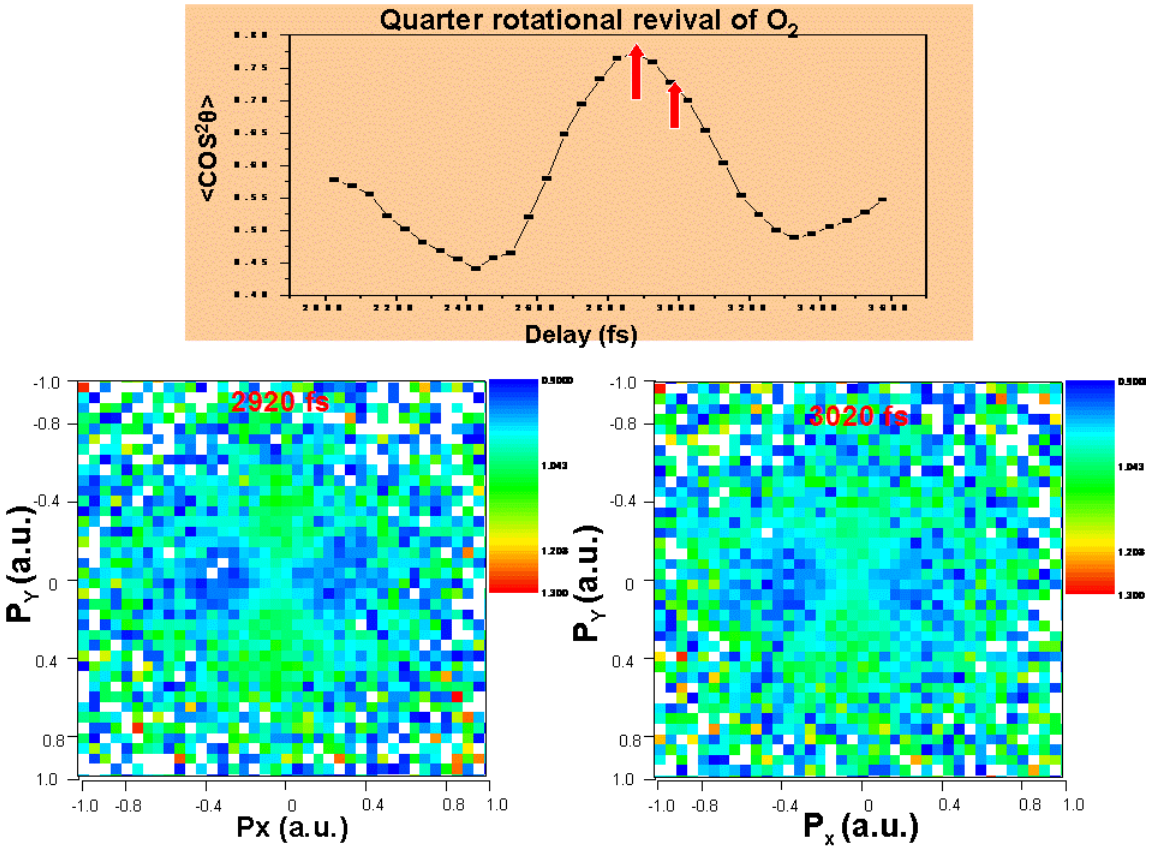

Figure 6.22: Momentum space images of electrons generated at the position of delays for aligned (2920fs) and close to aligned peaks (3020 fs)

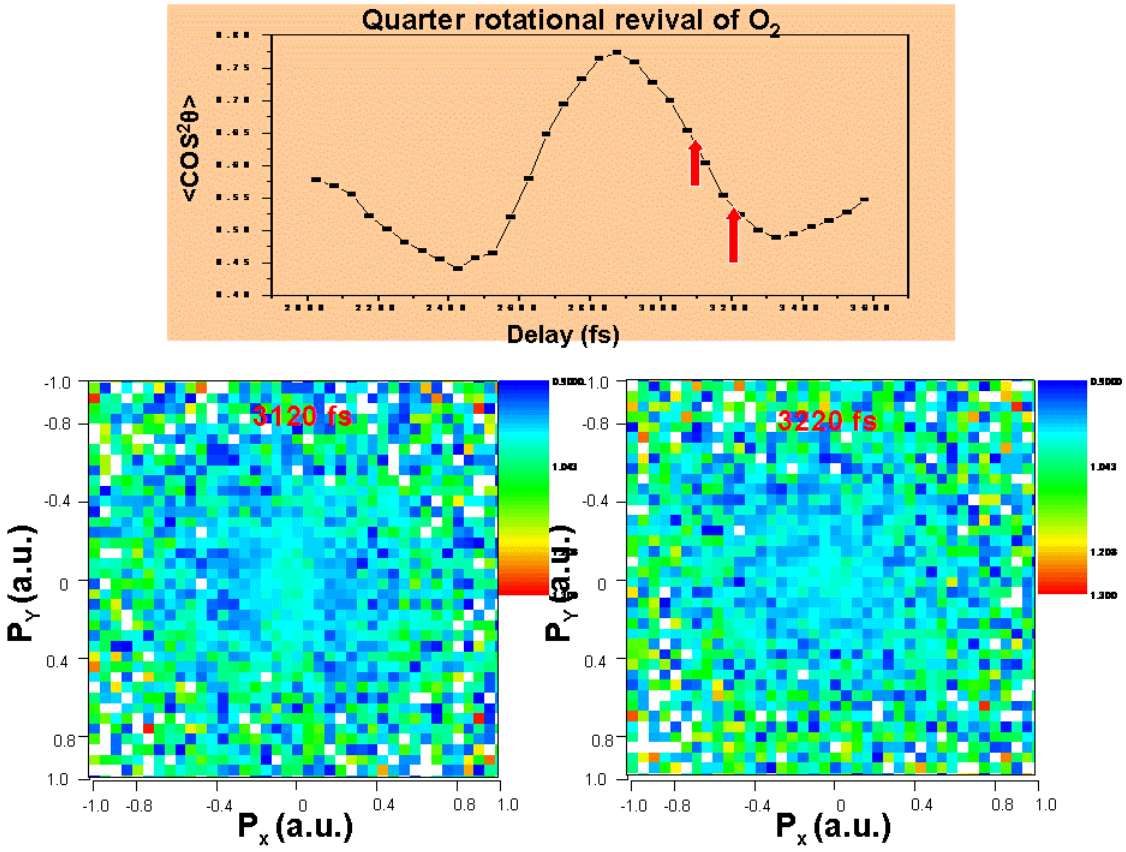

Figure 6.23: The momentum space images of electrons generated at delays (3120 fs and 3220 fs) closer to the isotropic orientation of molecules

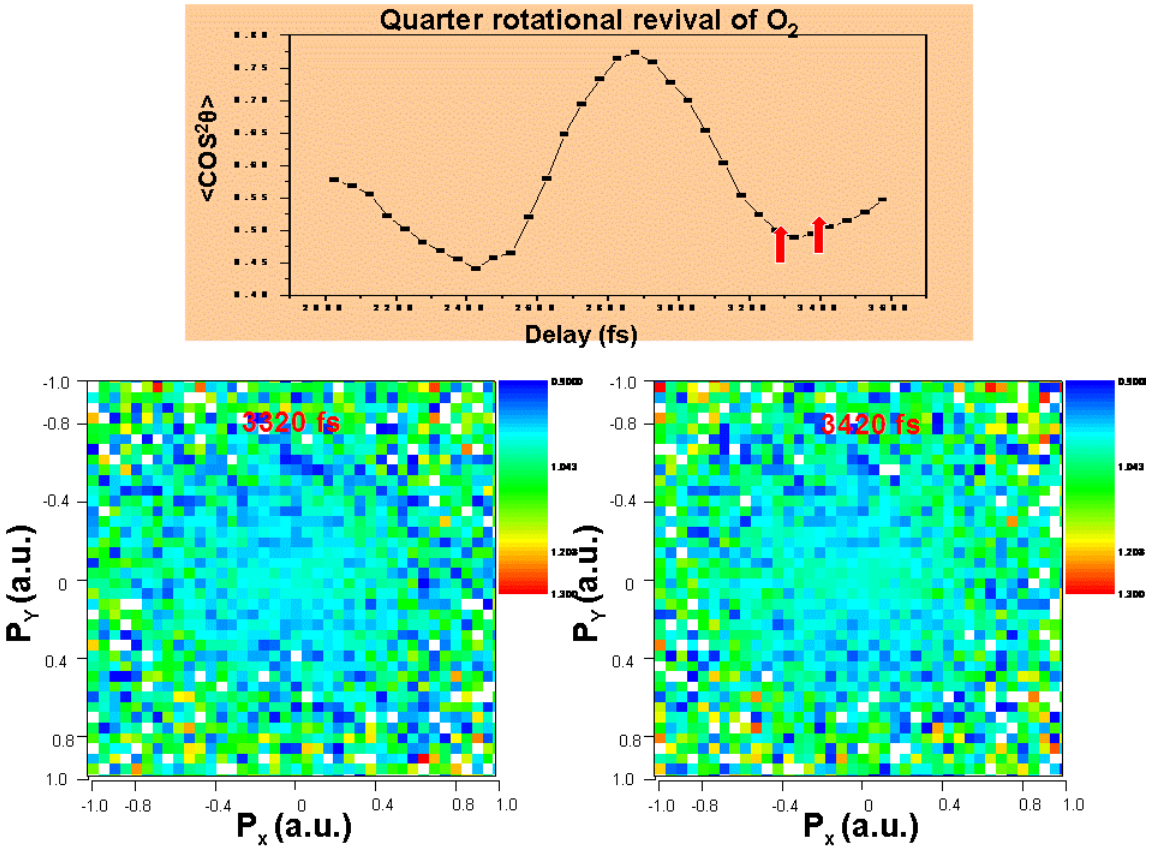

Figure 6.24: The momentum space images of electrons generated at delays (3320 fs and 3420 fs) closer to the isotropic orientation of molecules

6.5.3 Conclusion

We studied the partial revival structure of O_2 as well as the angular distribution of electrons in momentum space ionized from the aligned molecules. It is noted that the observed degree of alignment in each case was strongly determined by a number of factors such as intensity of the aligning pulse and rotational temperature of molecules. The reason for good alignment at high intensity of the aligning pulse is due to the higher J state population. The effect of the intensity of the aligning pulse on the alignment was observed implicitly on the θ distribution of two different channels of fragmentations. We also compared the rotational revival structure of O_2 at two different temperatures, and it is observed that the pre-cooling of the jet exhibited a higher degree of alignment, because at low temperature the J state population excited by the aligning pulse dominates the initial J state population due to thermal excitation. It allows a greater coherency among the different rotational states in a wave packet. Therefore the observed degree of alignment is dependent on the rotational temperature and the intensity of the aligning pulse, as well as on additional parameters such as anisotropy of molecular polarizability, and the shape and duration of the aligning pulse. We observed strong modulation of the angular structure of electrons in the low energy region of momentum space as a result of the alignment of the O_2 molecules. The resulting angular structure in the momentum image of the continuum electrons is the filtered image of the transverse momentum in the initial orbital. This approach of observing the molecular orbit in the angular distribution of electrons can be extended to other linear molecules.

CHAPTER 7 - Momentum imaging of doubly charged ions of Ne and Ar in the sequential ionization region - Quest for a clock

7.1 Introduction

In the sequential double ionization process, the second emission of an electron follows the first with a time delay that depends upon how fast the electric field rises in the pulse, i.e. the pulse length. If a pulse is very short, the rise time of the pulse becomes so fast that double ionization can occur within a single pulse through over-barrier ionization. Thus the emission process and the pulse rise time are closely connected. This is unlike the case for nonsequential double ionization, where the first emission is triggered by the field but the second emission is the result of impact ionization by the rescattering of the first electron. Nonsequential double ionization has received extensive attention in the last several years [87, 88]. In this chapter we read the sequential release of two electrons in real time using a pulse as a clock [30].

7.2 Sequential ionization in a circularly polarized pulse and the clock

Depending on the shortness of a circularly polarized pulse, the sequential ionization of two electrons due to this pulse can be thought of as made up of two clocks: a 'second hand clock' based on the optical cycle (2.7 fs scale for 800nm radiation) and a minute hand clock based on the envelope (8fs FWHM for the pulse discussed here). To address this clock more explicitly, we first explain qualitatively in terms of over-barrier electron release (for simplicity), and then compare the experimental observations to a calculation based on full consideration of rates for the entire tunneling process.

In circular polarization, the electric field vector rotates in such a way that at first the magnitude rises gradually to a maximum and then it starts descending again. The first electron goes over-barrier at an electric field value given by

$$E_1 = \frac{I_{1P}^2}{4Z_1} \tag{7.1}$$

where I_{1P} is the ionization potential for single ionization of an atom with final charge state Z_1. Similarly the over-barrier field for the second emission is expressed as

$$E_2 = \frac{I_{2P}^2}{4Z_2} \tag{7.2}$$

where I_{2P} the ionization potential for double ionization with final charge state Z_2.

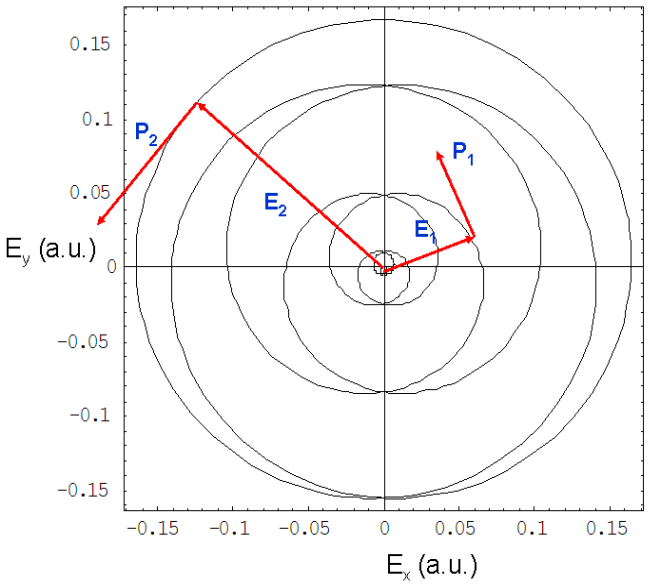

Figure 7.1: Illustration of the sequential emission of two electrons in a circularly polarized pulse. Unlike the linear pulse, the electric field vector of a circularly polarized pulse rotates with respect to time. The first emission of an electron occurs as soon as it is acted on by the electric field (E_1) enough for over-barrier. Similarly the second electron releases at the higher threshold (E_2) .The final direction of momentum in each case is normal to the electric field at the time of emission.

When electrons release at the respective electric fields E_1 and E_2 by over-barrier, the initial momenta of both electrons are zero. Subsequently both of them are acted on by the electric field of the pulse and they attain the final momenta p_1 and p_2 respectively. In circular polarization, the magnitudes of momenta p_1 and p_2 are given by

$$p_1 = \frac{E_1}{\omega} \tag{7.3}$$

and

$$p_2 = \frac{E_2}{\omega} \tag{7.4}$$

The final directions of the vector momenta p_1 and p_2 are normal to the respective over-barrier fields E_1 and E_2. The measurement of p_1 and p_2 can be read back on the minute hand of the clock as provided by the pulse envelope to observe the times at which the electrons are emitted. Such a clock would read as a second hand in the ideal case if the angle between p_1 and p_2 has been measured. For an extremely short pulse (containing only one optical cycle = 2.7 fs for 800nm) with proper intensity, the time interval between two emissions could be less than an optical cycle and this angle would just be $\omega\Delta t$, where Δt is the time delay between two releases.

$$\omega\Delta t = \cos^{-1}\left(\frac{p_1 \cdot p_2}{|p_1||p_2|}\right) \tag{7.5}$$

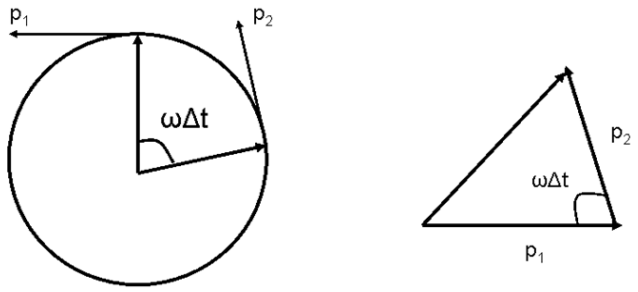

Figure 7.2: (a) Illustration of the sequential release of two electrons in a circularly polarized pulse containing one optical cycle (2.7 fs for 800nm radiation). Such an extremely short pulse can be used find the sub-fs time interval between two emissions. (b) Angle between the directions of two emissions can be determined by measuring the vector momenta p_1 and p_2; eventually it would give the sub-fs time interval between these two emissions.

Eventually the time interval between two emissions would be

$$\Delta t = \frac{1}{\omega}\cos^{-1}\left(\frac{p_1 \cdot p_2}{|p_1||p_2|}\right) \tag{7.6}$$

Therefore, if we have extremely short pulses, the time gap between two emissions could be read in the sub-fs scale with a one optical cycle (2.7fs) clock, but vector momenta of both electrons have to be measured separately in order to make this clock work.

7.2.1 Can we get the information on vector momenta of two electrons by measuring the momentum of a doubly charged atom?

In our real situation, the pulse length is longer than the expected ideal case, and consists of more than one optical cycle. The time delay between two emissions could exceed 2.7 fs. In such a case, the magnitude of the vector sum of p_1 and p_2 averages over this angle. However, the vector sum of the spectrum is capable of giving the information on the individual magnitudes p_1 and p_2. These values can in turn be interpreted in terms of the time difference between the releases of the two electrons. Measuring the vector momentum of the doubly charged ion will give the vector sum of p_1 and p_2 for two electrons.

7.3 Method

The 30fs pulse was spectrally broadened in a hollow-core fiber and compressed to 8fs by means of a number of bounces on chirped mirrors after the hollow fiber as described in Chapter 2. We used an achromatic quarter wave plate after the fiber to switch the linearly polarized pulse to the circularly polarized. The laser beam (propagating in the x-direction) was focused by a parabolic mirror of focal length 7.5 cm at the well collimated jet (y-direction). The ions were guided to the detector by an extraction field of 2 V/cm in the z-direction (along the spectrometer axis). More details about the experimental setup are explained in Chapter 2.

7.4 Single ionization of argon at intensities in the over-barrier region

As we described in the previous chapter (experimental part), the momentum resolution is best in the time direction (along the axis of the spectrometer) compared to the gas jet and the laser propagation directions. On the basis of the resolution achieved in our setup, we expect to see a highly resolved physical picture in the spectrum in that direction. In Figure 7.3 we present the schematic of momentum spectrum of a singly ionized argon atom at high intensity. The double-peak structure with a minimum at zero is the projection of the expected donut structure in the polarizing plane onto the time direction.

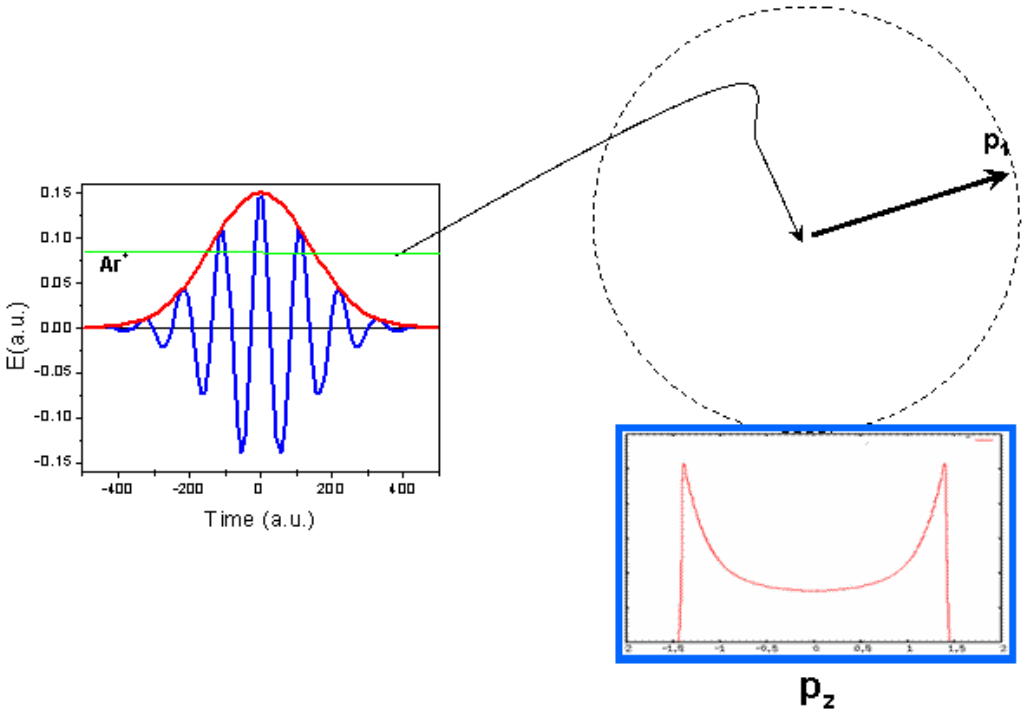

Figure 7.3: Schematic of single ionization of argon in a circularly polarized pulse (envelope of the pulse). The expected (simulated) donut structure of the momentum distribution of the singly ionized argon in the plane of polarization is shown in the 2D picture. The double peak structure is the projection of the donut structure onto the z-direction. (1a.u. (time) = 241fs, 1 a.u. (E) = 5.14 x 10^{11} V/m)

In Figure 7.5 we show (black curves) our experimental projected momentum spectra from single ionization of argon at two intensities. At lower intensities before reaching the saturation of single ionization, the shapes as well as the total yield of the momentum spectra are intensity dependent. However, at higher intensities the spectra were found to be nearly independent of the laser peak intensity [49]. This occurs because the ionization in these cases is best described by the over-barrier model which fixed the value of the field at which the electron is emitted. If one considers the emission of the electron at the field when it reaches the over–barrier value (7.1), then the radius of the donut should be given by

$$p_1 = \frac{I_{1p}^2}{4Z\omega} \tag{7.7}$$

For argon, I_{1p} =15.76 eV, and Z=1

$$p_1 = \frac{(15.76/27.2)^2}{4\times 1\times 0.057} a.u. = 1.48 a.u.$$

This expression yields the width of the double peak structure as

$$2p_1 = 2.96 a.u.$$

which is only slightly smaller than the observed FWHM diameter (~3.8 a.u.) of projected single ionization spectra for the higher intensity in Figure 7.5. This result does not depend on the actual peak intensity used, as is approximately borne out by the experimental data. Note that the observed FWHM diameter is larger than $2p_1$. This is expected since a more quantitative examination of over-barrier ionization has shown that the ionization rate continues to rise slightly as the field proceeds beyond the static barrier suppression value [21].

7.5 Double ionization of argon: complex structure

Unlike the much simpler structure of the momentum spectrum of the singly charged ion, the momentum spectrum of a doubly charged ion shows a more complex nature. Figure 7.4 shows a schematic of the over-barrier picture of the double ionization of argon, and explains how the momentum of doubly ionized argon is determined by the angular correlation between the vector momenta of the two electrons more explicitly. Two green lines over the pulse show the threshold for single and double ionization of argon.

In Figure 7.5 (red curves) the double ionization of argon shows a maximum at zero and a symmetric shoulder on each side of zero. In the over-barrier picture, the origin of this can be attributed to the emission of the electrons at different values of the electric field.

We shall explain this structure in the frame of the barrier suppression model. First consider single and double ionization potential of argon such as

$$I_{1p} = 15.76eV = 0.58a.u.$$

$$I_{2p} = 27.63eV = 1.01a.u.$$

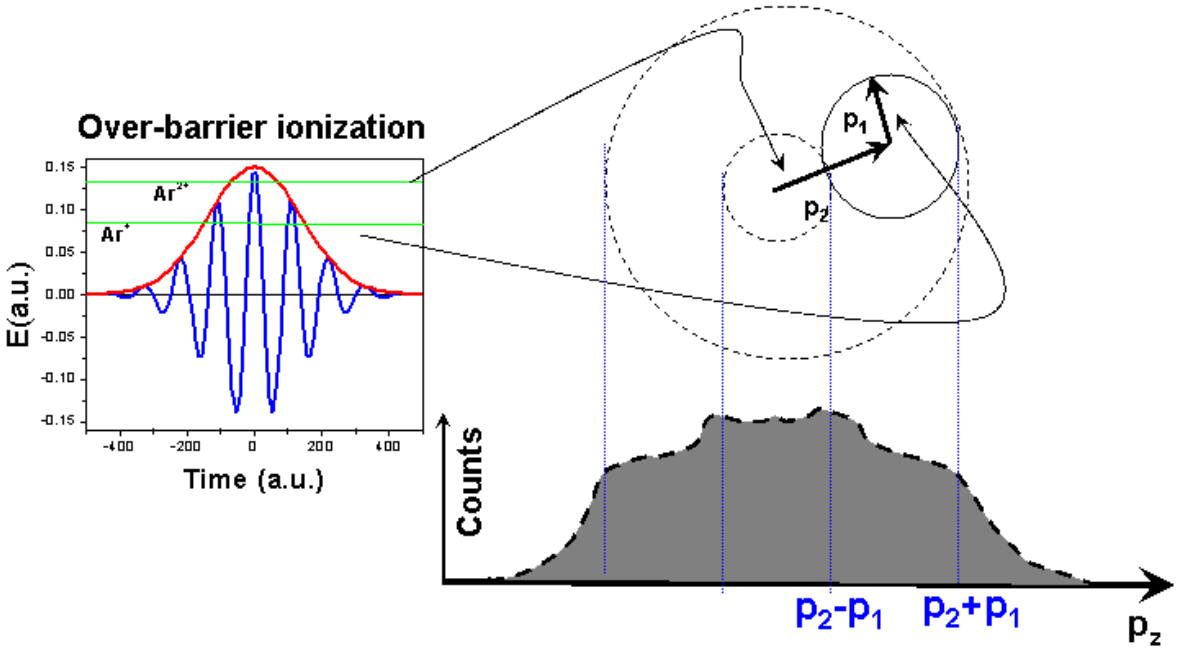

Figure 7.4: Illustration of the double ionization of an argon atom in a circularly polarized pulse (envelope of the pulse) through the over-barrier process. The two green lines in the pulse indicate the critical values of the electric field for the first and second electrons to be released by over-barrier. The right part of the figure shows how the two vector momenta of electrons give the complex structure in the momentum distribution of the doubly ionized argon in the time direction.

The corresponding values of the over-barrier fields are given by using equations (2.19)

$$E_1 = \frac{I_{1P}^2}{4Z_1} = \frac{(0.58)^2}{4} = 0.084 a.u. \tag{7.8}$$

and

$$E_2 = \frac{I_{2P}^2}{4Z_2} = \frac{(1.01)^2}{4 \times 2} = 0.129 a.u. \tag{7.9}$$

The intensities required to have the respective fields for over-barrier are 5×10^{14} and 1.16×10^{15} W/cm^2 respectively.

The drift momenta gained by the electrons emitted at the over-barrier electric fields are

$$p_1 = \frac{E_1}{\omega} = \frac{0.084}{0.057} a.u. = 1.47 a.u. \tag{7.10}$$

for the first electron and, for the second,

$$p_2 = \frac{E_2}{\omega} = \frac{0.129}{0.057} a.u. = 2.26 a.u. \tag{7.11}$$

It would be possible to determine the magnitudes of the p_1 and p_2 and also the angle between them uniquely only if both the electrons were emitted at the instant when the field reached over-barrier heights (E_1 and E_2). However, it is much more likely that each electron is released over the range of times when the field is near E_1 and E_2. If this range of times is larger than the optical cycle, the corresponding range of angles will be more than 2π. In this case one obtains recoil momenta in a range between (p_1+p_2) and (p_1-p_2), where these two cases correspond to the sum of the momenta of two electrons moving in the same and in opposite directions. In this scheme, we can use simple algebra to find the resultant momentum as

$$|p_1 + p_2| = \sqrt{p_1^2 + p_2^2 + 2 p_1 p_2 \cos\theta} \tag{7.12}$$

where θ is the angle between the two momentum vectors p_1 and p_2. Consider the two extreme cases, (i) $\theta = 0$,

$$|p_1 + p_2| = p_1 + p_2 = 3.73 a.u. \tag{7.13}$$

and (ii) $\theta = 180$

$$|p_1 + p_2| = p_1 - p_2 = 0.79 a.u. \tag{7.14}$$

The spectra shown in Figure 7.5 (red curves) are averaged over all possible angles between p_1 and p_2. The sum p_1+p_2 and difference p_1-p_2 calculated by the simple over-barrier picture are located at the two positions of a shoulder of the momentum spectrum as shown in Figure 7.5. The qualitative agreement of the calculated values with the data is good.

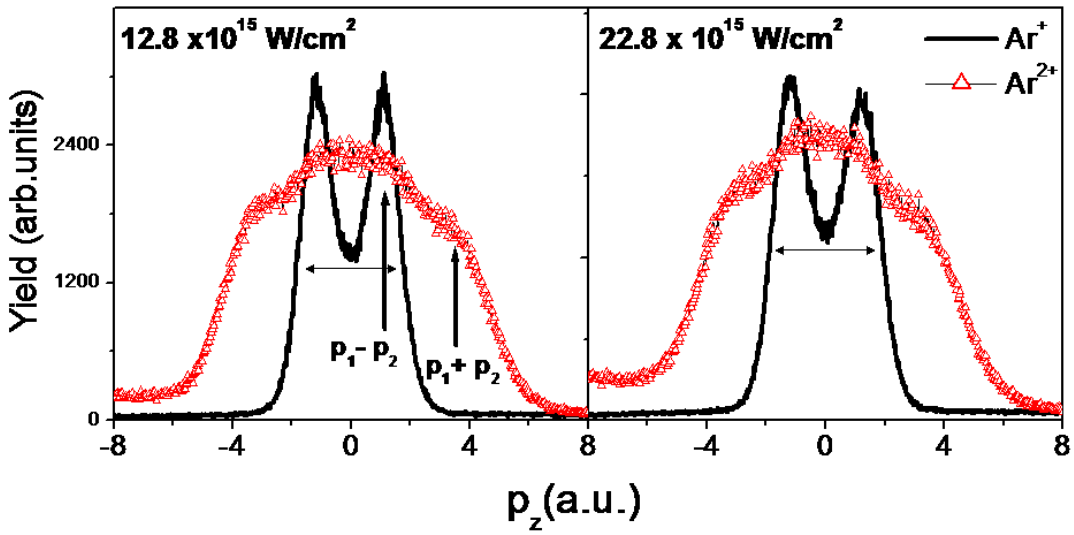

Figure 7.5: Spectra of the momenta of singly and doubly ionized Ar ions projected onto the z-axis (along the collection field of the spectrometer) for circularly polarized radiation at two different peak laser intensities. The horizontal arrow indicates the expected width of the single ionization peak in the over-barrier limit. The vertical arrows indicate the locations of the expected two sequential over-barrier ionizations, as discussed in the text.

7.6 Double ionization of neon

It seems obvious that neon could be the ultimate target atom to explain the complex structure of the momentum of a doubly charged ion, since the difference between the single and double ionization potentials is large as compared to argon.

Figure 7.6 shows data for neon. Compared to doubly ionized argon, the spectrum of Ne^{2+} shows more sharp features with a dip at zero momentum, and two other pronounced peaks on either side of zero. The difference can be explained qualitatively because the first and second ionization potentials (20 and 45eV) of neon differ much more than those of argon. As a result, very different values of the electric fields (0.13 and 0.34 a.u.) are required for the electrons to go over-barrier, leading to a greater difference between the relative values of p_1 (2.28a.u.) and p_2 (6.0a.u.). The corresponding values for the sum (p_1+p_2 = 8.28 a.u.) and difference (p_1-p_2 = 3.72 a.u.) of p_1 and p_2 are indicated by the arrows in Figure 7.6, where again qualitative agreement is obtained.

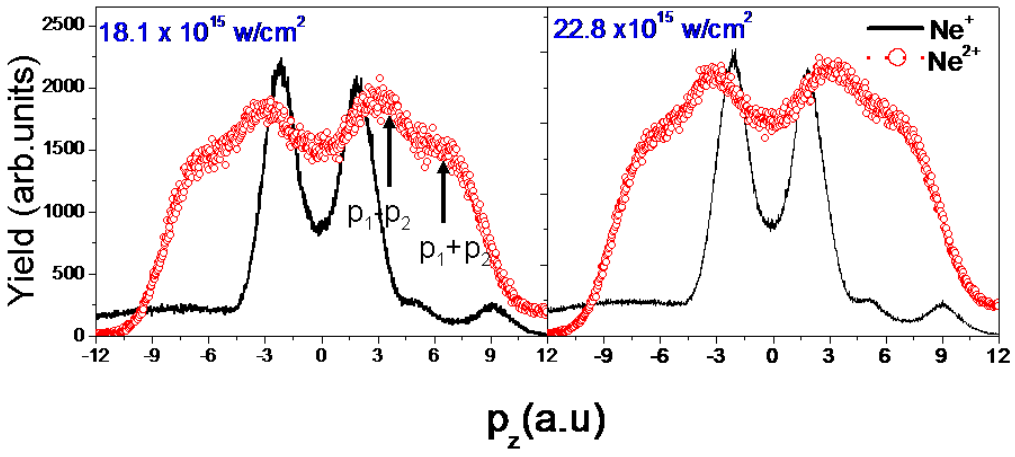

Figure 7.6: The momentum distributions of Ne^+ and Ne^{2+} similar to Figure 7.5. The most striking features of both spectra of Ne^{2+} are the pronounced peaks at the shoulder, which reflect the large difference in the critical values of the fields for neon to set electrons free through over-barrier compared to argon.

7.7 Two-dimensional spectra of Ar^{2+} and Ne^{2+}

It is noted that the positions of the sum and difference peaks in the shoulder in the momentum distribution of Ar^{2+} are close to each other and also located near the zero in the p_z spectra, but the corresponding peaks in the case of Ne^{2+} are well separated and located away from the zero. As we discussed earlier, this difference is attributed to the difference in the first two ionization potentials of argon and neon. Also it is seen clearly that there is a dip at zero at the center of the spectrum. To address this issue more clearly, two- dimensional momentum distributions of Ar^{2+} and Ne^{2+} in the plane of polarization are presented in Figure 7.7. For argon there is no dip at the center of the spectrum, while for neon the dip is quite clear. Because of the ellipticity in our radiation, the spectra show some asymmetry with respect to the y- and z-directions. Fortunately for this study, in the over-barrier region the ionization rate is not critically dependent on the intensity which makes this problem less severe than it would be if we were dealing with lower intensities.

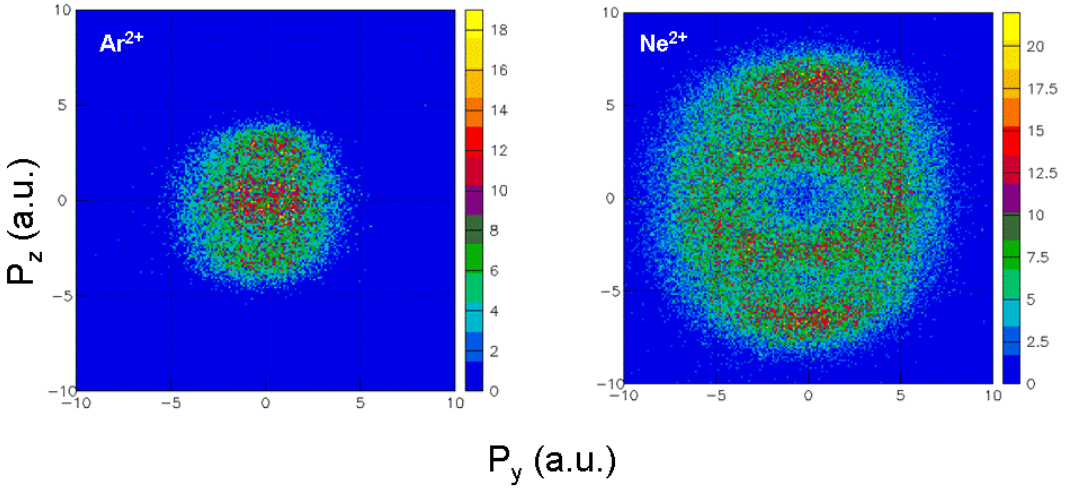

Figure 7.7: Two-dimensional momentum images of the doubly charged argon and neon ions produced by nearly circularly polarized 8fs pulses in the y-z plane at the peak intensity of 22.8x10 ^{15} W/cm^2.

7.8 How does theory predict experimental results?

Could the classical over-barrier picture also be reproduced by quantum calculation? In order to interpret the above experimental result more conceptually on the basis of the time dependent Schrödinger equation, I would like to present the theoretical simulation done by X. M. Tong with similar conditions of the experimental data. The model was formulated with the ionization rate with full consideration of both ADK and over-barrier for a range of intensities [89, 90]. It also accounted for the laser pulse spatial distribution. Therefore the model yields the momentum distribution of Ar^{2+} and Ne^{2+} irrespective of the processes responsible for generating these ions.

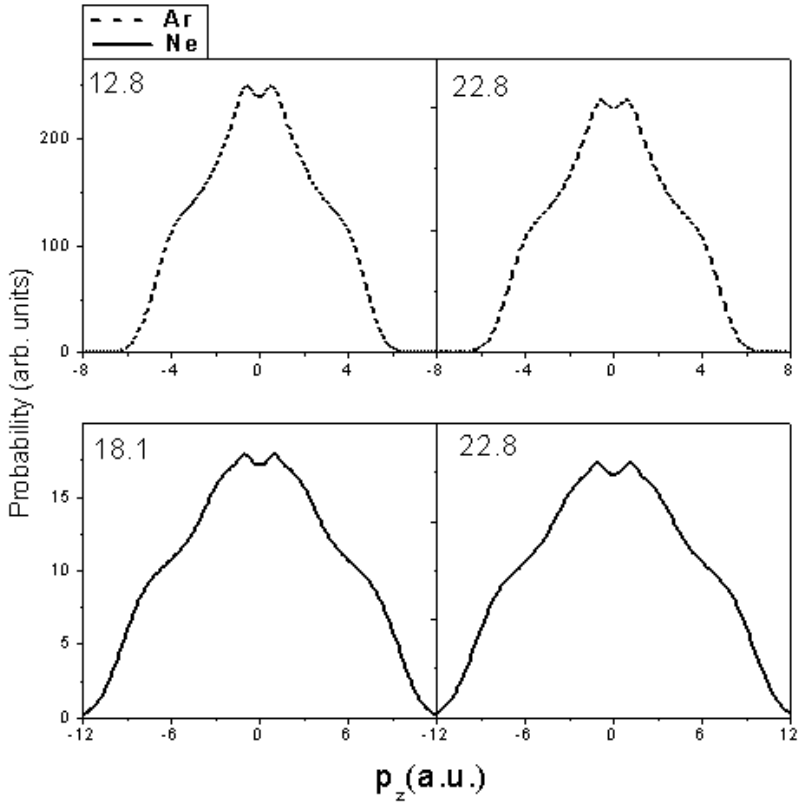

Figure 7.8: Theoretical calculation of the p_z distributions, corresponding to Ar^{2+} and Ne^{2+} of data of Figure 7.4 and 7.6. The peak intensities are given in units of 10^{15} W/cm^2 [90].

Figure 7.8 depicts the theoretical simulation of the momentum distribution of Ar^{2+} and Ne^{2+} for predicting the experimental results shown in Figures 7.5 and 7.6. Both the peaks correspond to p_1-p_2 and p_1+ p_2 , and the complicated shapes of all the simulated spectra are found to be well consistent with the experimental data. The dip in the theoretical calculation of Ne^{2+} is not as pronounced as that observed in the experimental data. The difference might be due to the effect of ellipticity of light used in the experimental data as well as uncertainty in the pulse shape and duration.

7.9 Time difference between two sequential emissions as estimated by over-barrier picture

The momenta p_1 and p_2 could be interpreted as the second-hand clock if we could perform independent measurements. We can use the present data to examine this issue by extracting the expected time difference between emission times of the two electrons from the present model. Consider the Gaussian shaped pulse with FWHM τ.

If the first sequential ionization occurs at time t_1 in the electric field strength E_1 during rising of the pulse,

$$E_1 = E_0 \exp(-\frac{2\ln 2 t_1^{\,2}}{\tau^2}), \tag{7.15}$$

where E_o is the peak electric field , then time t_1 can be expressed as

$$t_1 = \sqrt{\frac{1}{2\ln 2}\ln\left(\frac{E_o}{E_1}\right)}. \tag{7.16}$$

Similarly the time t_2 for the second sequential ionization can be expressed as

$$t_2 = \sqrt{\frac{1}{2\ln 2}\ln\left(\frac{E_o}{E_2}\right)}. \tag{7.17}$$

Then the time separation between two sequential emissions becomes

$$\Delta t = \sqrt{\frac{1}{2\ln 2}\left(\ln\left(\frac{E_o}{E_1}\right) - \ln\left(\frac{E_0}{E_2}\right)\right)}. \tag{7.18}$$

The resulting value for Δt is only rather weakly dependent on E_o. For the peak intensity of 22.8 x10 ^{15} W/cm^2, the resulting time difference for argon is 1.1 fs; and for neon is 2fs.

7.10 What is the value of Δt predicted by the model?

Now let us see how the theoretical model predicts the time gap of two emissions. The model gives the better calculation of the time dependence of the ionization rate during the pulse.

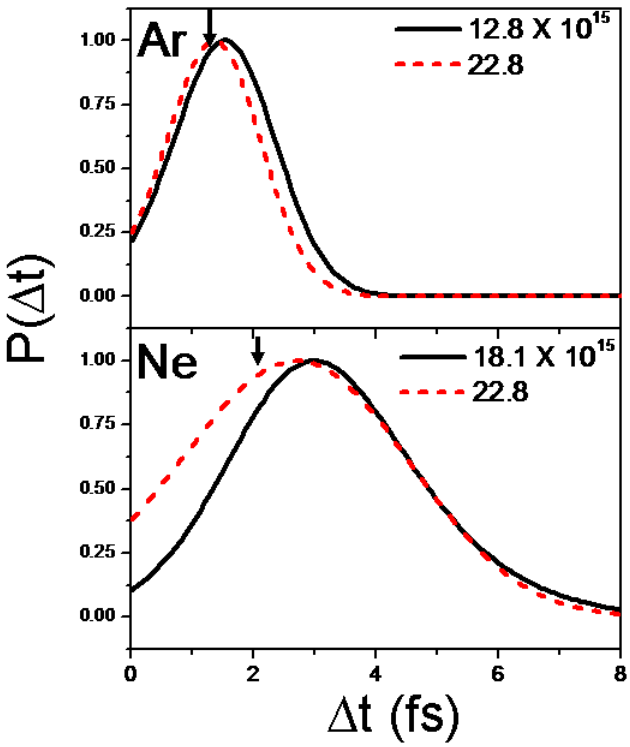

Figure 7.9: Comparing the model (envelope) and classical over-barrier (arrow) for the time gap between two sequential emissions of electrons [90].

Figure 7.9 depicts the probability distribution for generating Ar^{2+} and Ne^{2+} ions as a function of the time of separation between first and second ionizations. The peaks of calculated curves are remarkably close to the over-barrier values as shown by an arrowhead in each spectrum. Therefore the prediction made by over-barrier for the time gap between two emissions agrees well with the time dependent calculation. This agreement is much better for argon as compared to neon, and it is also noted that the time of separation of two emissions is even less than half the

optical cycle. Moreover the agreement between the over-barrier model and the calculation is better at higher intensities for both argon and neon. However the time gap is close to the optical cycle for neon. Therefore argon could be a good choice for this kind of time resolving experiment.

7.11 Why have we measured the momentum of ions instead of measuring the vector momenta of electrons separately?

The initial purpose of the experiment was to measure the vector momenta of two electrons separately and read the first and second over-barrier by a "second-hand" clock using the electric field vector of a pulse. We attempted to achieve success in the experiment with different experimental conditions for several shots, and later we recognized a series of drawbacks in our present system. In order to find the time separation between two electrons, the vector momentum of both electrons should be measured separately. Measuring two electrons from the same atom is another difficult task. The only alternative approach is to carry out a coincidence experiment on both electrons and their parent atom (doubly charged atom). To get any meaningful data without any large statistical fluctuation, we need a fairly large volume of data. But the repetition rate (1KHz) of the present laser system is so low that it takes several days to run the experiment without altering any experimental conditions for a useful amount of data. The temperature of the jet along the jet direction is another serious problem for achieving coincidence of three particles in all directions. The momentum resolution of the present setup is excellent in the direction of the spectrometer axis but is not good enough in the other two directions, which is another serious drawback for coincidence experiments. Moreover, we found that the pulse duration (~8 fs) is not short enough to define the second-hand clocks. Furthermore, the pulse pair resolution (~ 15 ns) current which the electronic module used in our system creates the problem of resolving the positions of two electrons if they subsequently impinge on the detector in less than 15ns.

7.12 Conclusion

We have studied the momentum distribution of doubly charged argon and neon produced by very short pulses (8fs FWHM) of nearly circularly polarized radiation at relatively high intensities. The singly ionized atom shows much simpler structure which is the projection of the donut structure along the time direction. The complex structure of the momentum of doubly ionized argon and neon is due to the averaging of the vector momentum of two electrons directed in different directions over time, and is interpreted by both the over-barrier model and the full time-dependent calculation. The agreement between the two interpretations is striking. By inspecting the time difference between two subsequent emissions of electrons from argon and neon atoms from the calculation, it is noticed that the time difference is even less than an optical cycle for the case of argon. This conclusion is based on reading the "minute-hand" clock provided by the known time dependence of the pulse envelope. The most important conclusion of this experiment is that it could be a reference for another experiment in which the emission of electrons take place in such a short time gap that the electric field vector can be used as a "second-hand" clock to read the instant of ionization with precision less than the optical cycle. The best way of reading the "second-hand" clock is to measure the momentum vector of the two electrons independently and deduce the angle between them. Obviously this experiment will be more important if the time gap is a fraction of an optical cycle, which seems likely to occur for argon (1.1fs) but not for neon (2fs). There is no doubt that this will be even more interesting if we can use this approach to the fragmentation via ionization of light molecules.

CHAPTER 8 - Summary and conclusions

The low energy structure of an electron ionized from an atom (argon) by short laser pulses was studied at different wavelengths at intensities in the tunneling regime. The energy and angular structure in the momentum image reveal the different kinds of ionization dynamics in a laser field, and some of them are well consistent with the known multi-photon processes such as above-threshold ionization and Freeman resonances. Above all our study reveals a more pronounced angular pattern consisting of a fan-like structure radiating outwards from the origin. These structures are not associated with the angular momentum of any the particular resonant states. Instead, the structure is found to be related to diffraction phenomena as proposed by D. Arbó *et al*.[5] Moreover the nodal structure of first few ATI is consistent with the final parity state of an electron in the continuum as proposed by M. Wickenhauser *et al*. [6] Furthermore, we studied the low energy structure of electrons ionized from simple linear molecules O_2, CO_2 and N_2. The observation of the angular structure of electrons generated from these molecules still gives the same basic structure irrespective of their complicated structure as compared to the atom. The nodal structure of each ATI peak is found to be well agreed with the final parity state of electrons in the continuum. These studies give new hope for further observation of the multi-photon process of even more complex molecules in the future.

From our previous study [74, 75], the molecular orbit of simple molecules can be observed in the angular distribution of the ion pairs in coincidence produced by double ionization by a rescattering event. The present study successfully demonstrated an alternative approach in which the molecular orbit of O_2 could be mapped in the angular distribution of electrons ionized from aligned O_2 molecules. The low energy structure of electrons observed in the momentum image is actually the filtered image of the Fourier transform of the initial orbital of O_2. This simple and direct way of observation of a molecular orbit can, in fact, be extended at least to several other linear molecules.

Furthermore we also studied the sequential double ionization of argon and neon using short pulses (8fs) at high intensities. We explored that the momentum vector of the doubly ionized ion could be used for inferring the time and angular correlation of two electrons released sequentially. We deduced that the time difference between the two emissions is even less than an optical cycle for argon, and this conclusion is based on the minute-hand clock provided by the

known time dependence of the pulse envelope. This experiment could be a reference for another experiment in which the electric field vector can be used to read the time difference with an accuracy of a fraction of an optical cycle. It is possible to read this clock only if we measure the momentum vectors of two electrons independently and find the angle between vectors. Such an experiment could be more significant if the time difference is even less than an optical cycle. The rapid progress in the compression of pulses to a few optical cycles and stabilized absolute phases of pulses, definitely gives new hope to do this experiment.

Bibliography

[1] G. N. Gibson *et al*. Phys. Rev. Lett. 68, 1904 (1992)

[2] H. G. Muller, Phys. Rev. A 60, 1341 (1999), J. Wasaf *et al*. Phys. Rev. A 67, 053405 (2003), H. G . Muller, Phys. Rev. Lett 83, 3158 (1999)

[3] M. P. Hertlein *et al*., J. Phya. B: At. Mol.Opt.Phys. 30, L197 (1997), H. G. Muller, Phys. Rev. Lett. 83, 3158 (1999)

[4] C.M. Maharjan, A. S. Alnaser, I. Litvinyuk, P. Ranitovic and C. L. Cocke, J. Phys. B 39, 1955 (2006)

[5] D.G. Arbó, S. Yoshida, E. Persson, K. I. Dimitriou, and J. Burgdorfer, Phys. Rev. Lett. 96, 143003 (2006*)*

[6] M. Wickenhauser, X. M. Tong, D. G. Arbó, J. Burgdorfer, and C. D. Lin , Phys. Rev. A 74, 041402(R) (2006)

[7] M. Wickenhauser, X. M. Tong, and C. D. Lin, Phys. Rev. A 73 , 011401(R) (2006)

[8] Chen Zhangjin , Toru Morishita, Anh-Thu Le, M. Wickenhauser, X. M. Tong, and C. D. Lin , Phys. Rev. A 74, 053405 (2006)

[9] Toru Morishita, Z. Chen, S. Watanabe, and C. D. Lin, Phys. Rev. A 75, 023407 (2007)

[10] A. M. Perelomov, V. S. Popov, and M. V. Terent'ev, Sov. Phys. JEPT, 23-924 (1966)

[11] M. V. Amosov, N. B. Delone, and V. P. Krainov, Sov. Phys. JETP 64, 1191 (1986)

[12] F. Fabre, G. Petite, P. Agostini , and M..Clement, J. Phys. B: At. Mol. Phys 15, 1353 (1982)

[13] G. Petite, F. Fabre, P. Agostini, M. Crance and M. Aymar, Phys. Rev. A 29, 2677

[14] P. Lombropoulos, Adv. At. Mol. Phys. 12, 87 (1984)

[15] P. Agostini, F. Fabre, G. Mainfray, G. Petite and N. Rahman, Phys. Rev. Lett 42, 1127 (1979)

[16] G.G. Paulus *et al*., J. Phys. B 27 L703 (1994)

[17] R. R. Freeman, P. H. Bucksbaum, H. Milchberg, S. Darack, D. Schumacher, and M.E. Geusic, Phys. Rev. Lett. 59, 1092 (1987)

[18] Patrick J Randerson, PhD thesis, Ohio State University (2005)

[19] V. Keldysh, Sov. Phys. JETP 20, 1307 (1965); F. H. M. Faisal, J. Phys. B 6, L89 (1973); H. R. Ress, Phys. Rev. A 22, 1786 (1980)

[20] S. August, D. D. Meyerhofer, D. Stricklnad, and S. L. Chin, J. Opt. Soc. Am. B, 8,858 (1991)

[21] Armini Scrinzi, Michel Geissler and Thomas Barbec, Phys. Rev. Lett, 83,706, (1999)

[22] B. Walker *et al*., Phys. Rev. Lett. 73, 1227 (1994)

[23] P. B. Corkum, Phys. Rev. Lett. 71, 1994 (1993)

[24] K. J. Schafer, B. Yang, L. F. DiMauro and K. C. Kulander , Phys. Rev. Lett. 70, 1599 (1993)

[25] M. Lewentein *et al*., Phys. Rev. A 49, 2117, (1994))

[26] B. Fuerstein *et al*., Phys. Rev. Lett. 87, 043003 (2001)

[27] A. S. Alnaser *et al*., Phys. Rev. Lett 91, 163002 (2003)

[28] R.Dorner *et al*., Adv. in Atom. Mol., and Opt. Physics 48, 1 (2002)

[29] H. B. van Linden van den Heuvell and H. G. Muller, in 'Studies in Modern Optics No.8: Multiphoton Processes', edited by S. J. Smith and P. L. Knight (Cambridge University Press, Cambridge England, 1988).

[30] P. Dietrich, F. Krausz, P. B. Corkum, Opt. Lett.25, 8 (2000)

[31] P. B. Corkum, N. H. Burnett, and F. Brunel, Phys. Rev. Lett 62, 1259 (1989)

[32] T. Barbec and F. Krausz, Rev. Mod. Phys, 72, 545 (2000)

[33] R. L. Fork, O. E. Martinez, and J. P. Gordon, Opt. Lett. 9 150 (1984)

[34] D. Strickland and G. Mourou , Opt. Commun. 56, 219 (1985)

[35] S. Ghimire, B, Shan. C. Wang, and Z. Chang, Laser Physics, 15 838 (2005)

[36] A. Stingl, C. Spielmann, F. Krausz and R. Szipocs, Opt. Lett. 19, 204 (1994)

[37] L. Gallmann, G. Steinmeyer, D. H. Shuutter, T. Rupp, C. Iaconis, I. A. Walmsley and U. Keller, Opt. Lett. 26, 96 (2001)

[38] R.Trebino, "Frequency-Resolved Optical Gating: The Measurement of Ultrashort Laser Pulses," Kluwer Academic Publishers, Boston, MA (2000).

[39] Quantonix : http://www.quantron.com

[40] J. Ullrich, R. Moshammer, A. Dorn, R. Dörner, L. Ph. H. Schmidt and H. Schmidt-Böcking, Rep. Prog. Phys. 66 , 1463 (2003), R. Dörner, V. Mergel, O. Jagutzki, L. Spielberger, J. Ullrich, R. Moshammer, H. Schmidt-Böcking, Physics Reports 330, 95 (2000)

[41] D. R. Miller, Atomic and molecular beam methods, Vol.1 ch. Free Jet Sources, p. 14ff, Oxford University Press, Oxford/New York, 1988

[42] Ekaterina Eremina, PhD Thesis. Max-Born-Institute for Nonlinear Optics and Short Pulse Spectroscopy in Berlin

[43] Joseph Ladislas wiza,, Nuclear Instrumentation and Methods, 162, 587, 162

[44] www.roentdek.com

[45] T. Osipov, PhD Thesis, Kansas State University (2003)

[46] A. S. Alnaser *et al*., Phys. Rev. Lett. 93, 183202 (2004)

[47] X. M. Tong, Z. X. Zhao, and C. D. Lin, Phys. Rev. A.66 033402 (2003)

[48] P. B. Corkum, N. H. Burnett, and F. Brunel, Phys. Rev. Lett. 62, 1259 (1989)

[49] A. S. Alnaser, X. M. Tong, T. Osipov, S. Voss, C. M. Maharjan, B. Shan, Z. Chang, and C.L. Cocke , Phys. Rev. A 70, 023413 (2004)

[50] G. G. Paulus, W. Nicklich, H. Xu, P. Lambropoulos, and H. Walther, Phys. Rev. Lett. 72, 2851 (1994)

[51] G.G. Paulus, F. Grabson, and H. Walther, R. Kopold and W. Becker, Phys. Rev. A 64, 021401 (R) (2001)

[52] R. Wiehle, B. Witzel, H. Helm and E Cormier, Phys. Rev. A 67, 063405 (2003)

[53] A. Rudenko *et al*., J. Phys. B: At. Mol. Opt. Phys. 37, L407-13 (2004)

[54] P. Hänsch, M. A. Walker, L. D. Van Woerkom , Phys. Rev. A 55, R2535 (1979)

[55] J. Wasaf, V. Veniard, R. Tajeb and A. Maquet, Phys. Rev. Lett 90, 013003 (2003)

[56] R. Moshammer , J. Ullrich, B. Feuerstein, D. Fischer, A. Dorn, C.D. Schröter, J. R. Crespo, Lopez- Urrutia, C. Hoehr, H. Rottke, C. Trump, M. Wittman, G. Korn, and W. Sander, Phys. Rev. Lett. 91, 113002 (2003)

[57] J. Chen and C. H. Nam, Phys. Rev. Lett 91, 113002 (2002)

[58] K. I. Dimitrou, D. G. Arbó, S. Yoshida, E. Pearson and J. Burgdörfer, Phys. Rev. A 70, 061401 (2004)

[59] F. H. M. Faisal and G. Schlegel, J. Phys. B: At. Mol. Opt. Phys. 38, L223-31 (2005)

[60] M. J. Nandor, M. A. Walker and L. D. Van Woerkom , J. Phys: At. Mol. Opt. Phys 31, 4617 (1998)

[61] P. Hänsch, M. A. Walker and L. D. Van Woerkom, Phys. Rev. A 57, R709 (1998)

[62] P. Hänsch, M. A. Walker and L. D. Van Woerkom, Phys. Rev. A 57, R2559 (1996)

[63] M. J. Nandor, M. A. Walker, L. D. Van Woerkom and H.G. Muller, Phys. Rev. A 60, 1771 (1999)
[64] H.G. Muller and F.C. Kooiman, Phys. Rev. Lett. 81, 1207 (1989)
[65] B. Shan, X.M. Tong, Z. Zhao. Z. Chang and C. D. Lin Phys. Rev. A 66, R061401 (2002)
[66] A. S. Alnaser, C. M. Maharjan, P. Wang and I. V. Litvinyuk, J. Phys. B 39, L323-L328 (2006)
[67] B. Fredrich, D. P. Pullman, and D.R. Herschbacb, J. Phys. chem. 95, 8118 (1991)
[68] T. Seidemann, Phys. Rev. A 56, R17 (1997)
[69] V.A Cho and R.B. Berstein, J. Phys. Chem.95, 8129 (1991)
[70] J. Itantani, D. Zeidler, J. Levesque, Michael Spanner, D. M. Villenueve, and P. B. Corkum , Phys. Rev. Lett. 94, 123902 (2005)
[71] Tsuneto Kanai, Shinichirou Minemoto, and Hirofumi Sakai, Nature 435, 470 (2005)
[72] N. Yasumaru, K. Miyazaki, and J. Kuchhi , Appl. Phys. A 76, 983 (2003).
[73] X. M. Tong, Z. X. Zhao, C. D. Lin, Phys. Rev. A, 66, 033402 (2002)
[74] A. S. Alnaser, C. M. Maharjan, X. M. Tong, B. Ulrich, P. Ranitovic, B. Shan, Z. Chang, C. D. Lin, C.L.Cocke and I. V. Litvinyuk , Phys. Rev. A 71, 031403 (R) (2005)
[75] A. S. Alnaser, S. Voss, X. M. Tong, C. M. Maharjan, P. Ranitovic, B. Ulrich, T. Osipov, B. Shan, Z. Chang, and C.L. Cocke, Phys. Rev. Lett 93, 113003 (2004)
[76] B. Freidrich and D. Herschbach, Phys. Rev. Lett. 74, 4623 (1995)
[77] H. Sakai, C. P. Safvan, J. J. Larsen, K. M . Hilligsøe, K. Hald, and H. Stapelfeldt, J. Chem. Phys. 110, 10235 (1999)
[78] J. J. Larsen, K. Hald, N. Bjerre, H. Stapelfeldt, and T. Seideman, Phys. Rev. Lett. 85, 2470 (2000)
[79] T. Siedemann, Phys. Rev. Lett. 87, 153902 (1999)
[80] F. Rosca-Puruna and M. J. J. Vrakking, Phys. Rev. Lett 87, 153902 (2001)
[81] P.W. Dooley, I. V. Litvinyuk, Kevin F. Lee, D. M. Rayner, M. Spanner, D. M. Villeneuve, and P. B. Corkum, Phys. Rev. A 68, 023406 (2003)
[82] Igor Litvinyuk, Private communication
[83] K. F, Lee, I. V. Litvinyuk, P. W. Dooley, M. Spanner, D. M. Villeneuve, and P. B. Corkum, J. Phys. B 37, L43-48, (2004)
[84] M. Leibscher, I. Sh. Averbukh and H. Rabitz, Phys. Rev. Lett. 90, 213001 (2003)

[85] Michel Spanner, Olga Smirnova, Paul B Corkum, and Misha Yu Ivanov, J. Phys. B: At. Mol. Opt. 37, L243-L250 (2004)

[86] T. Weber et al., Phys. Rev. Lett. 84, 443 (2000), R. Moshammer et al, Phys. Rev. Lett. 91, 113002 (2003)

[87] A. Rudenko et al, Phys. Rev. Lett. 93, 213002 (2004)

[88] M. Weckenbrock *et al*., Phys. Rev. Lett. 92, 213002 (2004)

[89] X. M. Tong and C.D. Lin, J. Phys. B 38, 2593 (2005)]

[90] C. M. Maharjan, A. S. Alnaser, X. M. Tong, B. Ulrich, P. Ranitovic, S. Ghimire, Z. Chang, I. V. Litivinyuk and C. L. Cocke, Phys. Rev. A 72 ,041403(R) (2005)

Appendix A - Temperature of O_2 Jet (without pre-cooled)

Experimentally, it is relatively much easier to find the temperature of a jet using the images of the target jet and background gas (H_2O) in the detector plane. The typical experiment is carried out at low extraction field and at lower laser intensity to ensure that the momentum distribution of each case is well separated and resolved. The velocity of the target gas is determined by the

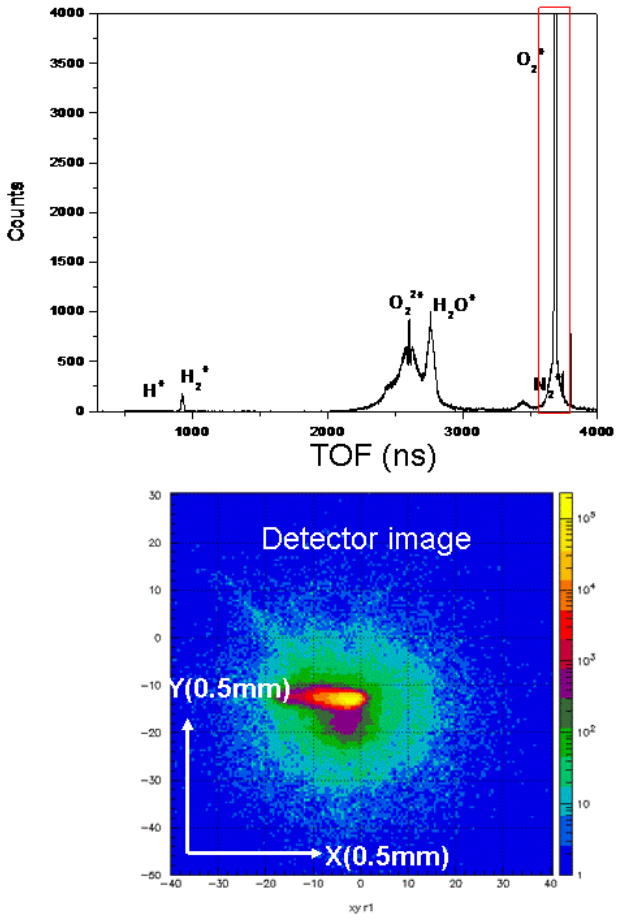

Figure 8.1A: Time of flight and detector image of the O_2 jet and background (H_20)

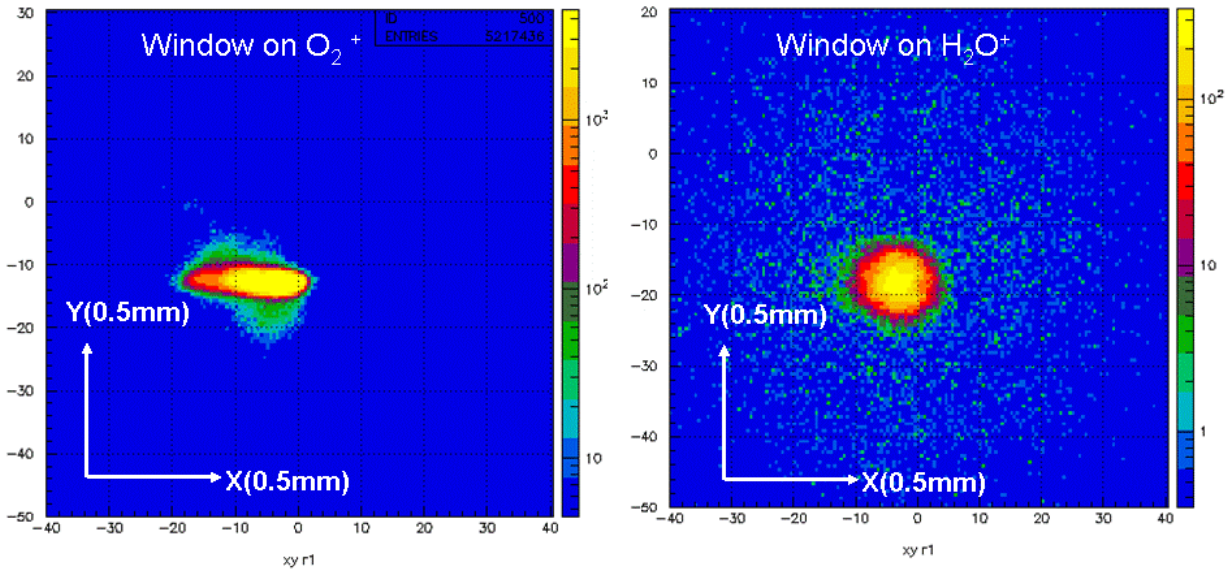

Figure 8.2A: Detector image of O^{2+} and H_2O^+ obtained by putting the windows over their time of flight.

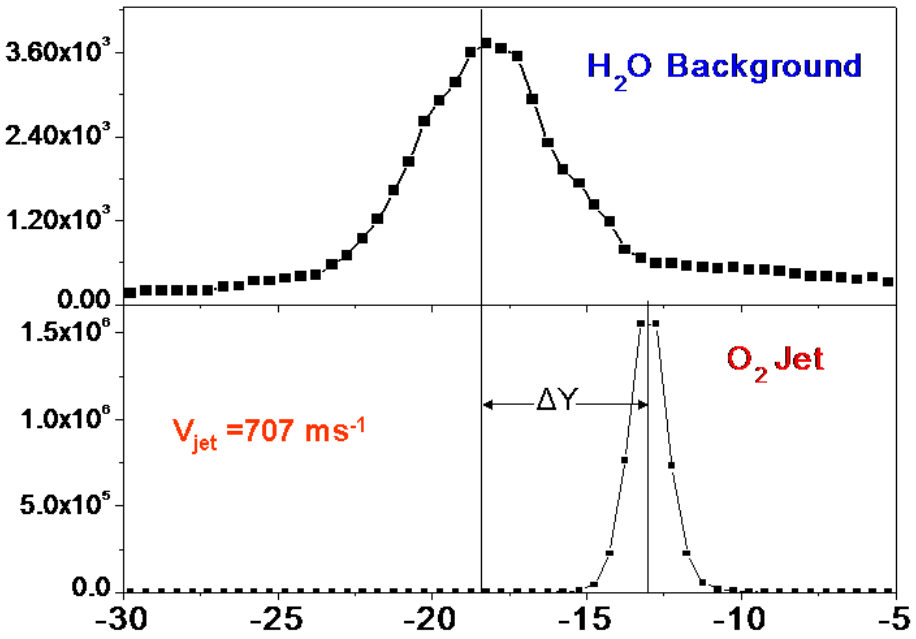

Figure 8.3 A: The projections of the detector images into the jet direction (y-direction).The jet velocity is determined by taking the ratio of the relative shift (ΔY=2.61mm) and time of flight of O_2^+ (3687.82ns). The velocity of the O_2 jet is estimated to be 707 m/s.

ratio of the total shift between the jet and background distribution to the time of flight of the jet as expressed by

$$V_{jet} = \frac{\Delta Y(mm)}{TOF(ns)} = \frac{2.61(mm)}{3687.82(ns)} = 707 ms^{-1} \qquad \text{(B.1)}$$

Fitting the Maxwell velocity distribution to the experimental distribution, the temperature of the jet can be determined as shown in Figure 8.4A. The jet temperature of jet was obtained as 26 K. The experiment was carried out without pre-cooling the jet.

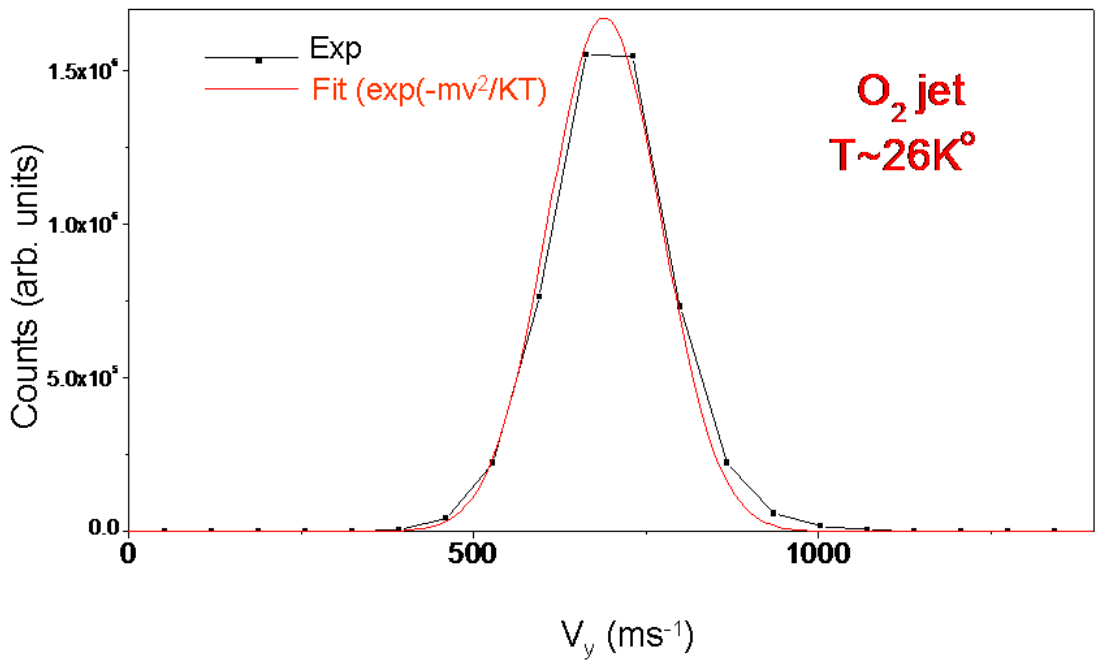

Figure 8.4 A: Determination of the temperature of the O_2 jet by fitting the Maxwell velocity distribution (exp ($-mv^2/2KT$)) to its observed velocity distribution.

Appendix B - Electronic boxes used for transferring the signal from detector to data acquisition system

Figures 8.5B and 8.6B show the circuit diagrams to design the filter box and the coupling box used for transferring the signal from the MCP and PSD of the detector to the pre-amplifier and differential amplifier.

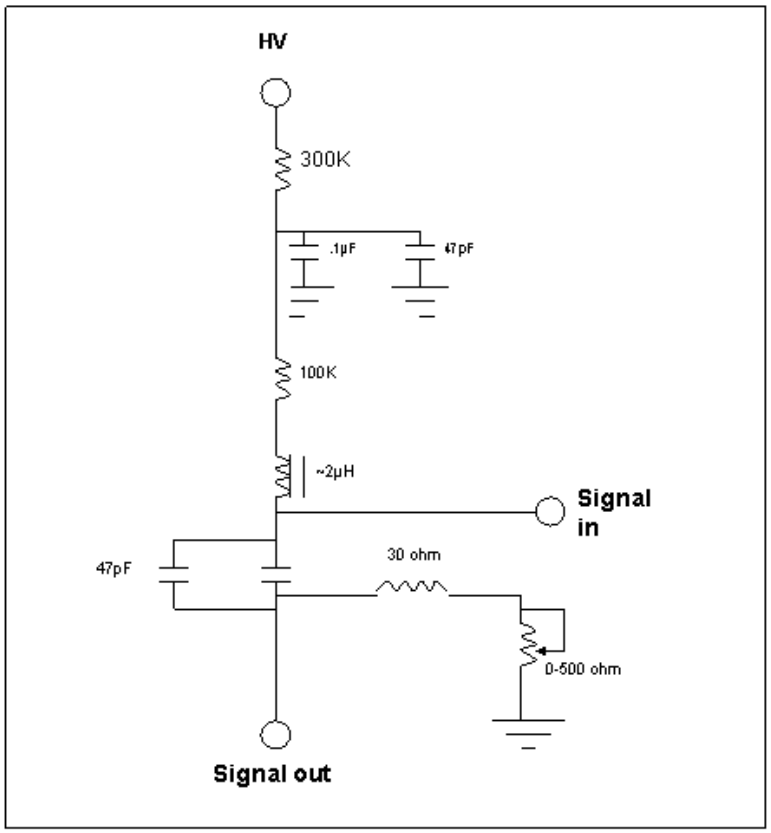

Figure 8.5B.: Filter box used to pick up the timing signal from the MCP. The potentiometer of this device can be used to adjust the impedance, which helps to minimize reflections of the fast timing signal due to impedance mismatch.

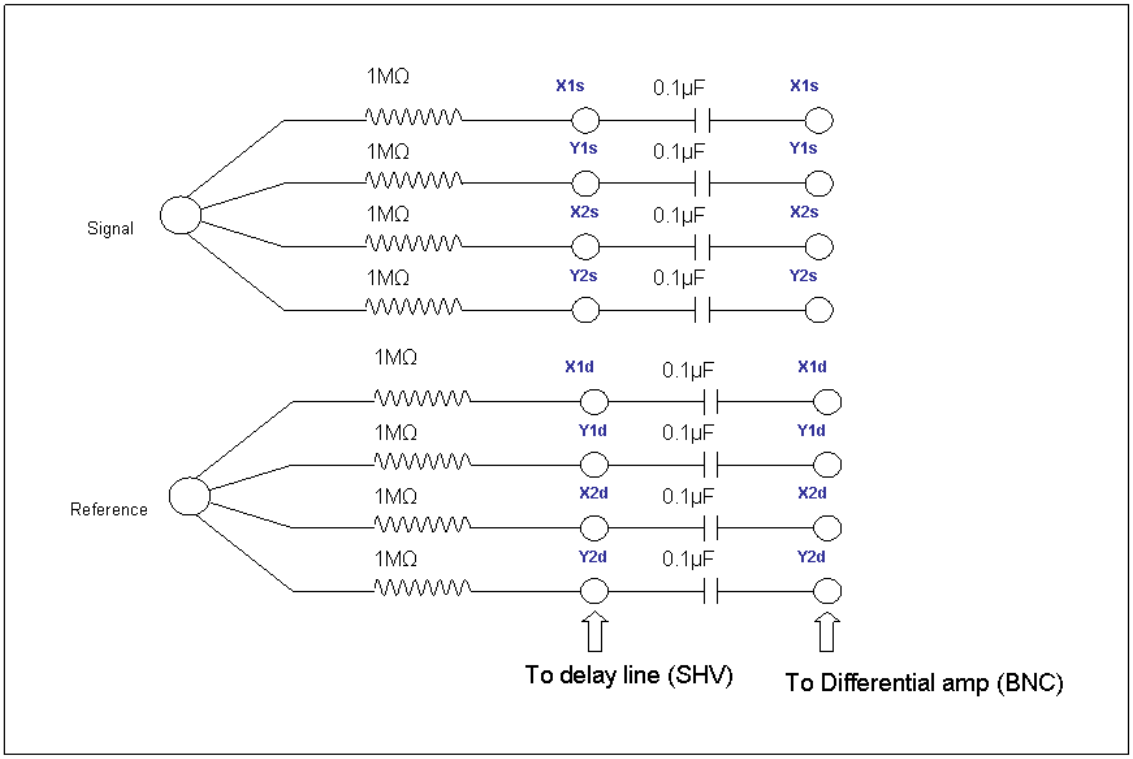

Figure 8.6B: The coupling box for transferring a signal from the anode to the differential amplifier. Eight inputs are provided for the signal and difference wire outputs from the four corners of the delay-line anode.

Appendix C - Partial revival structure of CO_2

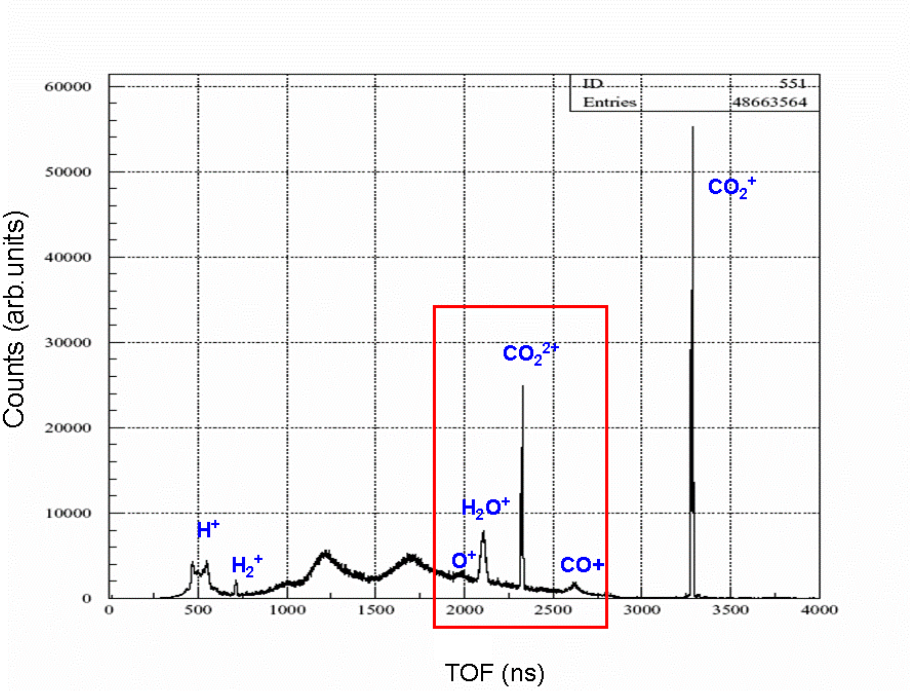

Figure 8.7C: Time-of-flight spectrum: Flight distance=5.3cm, electric field =55.1 volt/cm, pump I_o=1x10^{14} W/cm^2 and probe I_o=3.2x10 ^{15} W/cm^2. Since CO^{2+}/ O^{2+} is not well resolved, the CO^+ /O^+ channel as shown in the window was chosen for calculation of the alignment factor $\langle \cos^2 \theta \rangle$.

Figure 8.7C shows the TOF of different ionization channels of carbon dioxide observed on the shorter side of the detector (S =5cm) with a spectrometer field of 55.1 V/cm. The window shown in the time of flight spectra is for selecting the channel O^+/ CO^+ for reconstruction of the revival structure (Figure 8.8C). We do not have any other alternatives than to choose single ionization fragmentation since the channel CO^{2+}/ O^{2+} was not well resolved, and also the statistics were very poor. The intensity of the probe pulse for this particular experiment was not enough to produce doubly ionized fragments of CO_2.

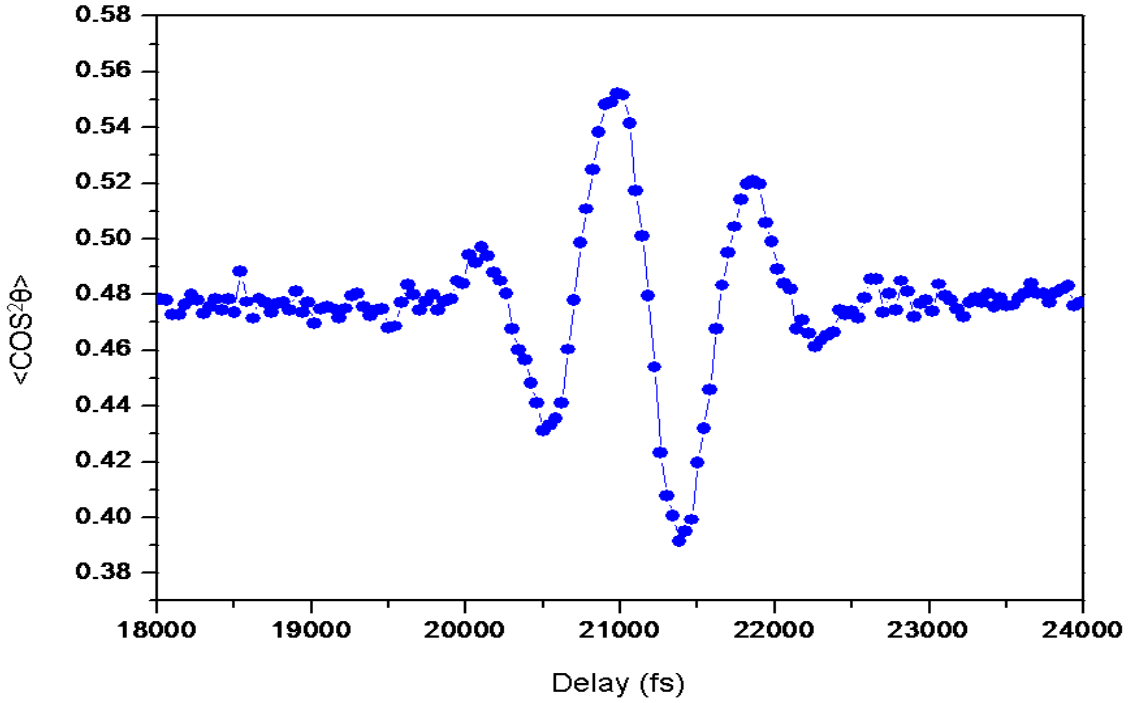

Figure 8.8C: Half revival structure of CO_2 molecules, pump I_o=1x10^{14} W/cm^2 and probe I_o=3.2x10 ^{15} W/cm^2

The degrees of alignment as well as the value of the base line of the structure in Figure 8.8C are poorer than those observed for oxygen. As we have pointed out already in Chapter 6, our window for reconstruction includes the CO^+ and O^+, and some of them originate from randomly oriented molecules at the low intensity region of the probe volume outside the focal volume of the pump beam. In addition, the contamination of O^+ from background sources like O_2 and H_2O to the window is also highly probable. These factors certainly degrade the situation. Another possibility for observing the poor degree of alignment might also be due to the pulse length of the aligning pulse. We used a pulse of duration 30 fs for both pump and probe beams. Since the value of the rotational constant turned out to be less for CO_2, the aligning pulse of 30 fs could be not long enough to align these molecules. In the present study we will not go qualitatively into this issue.

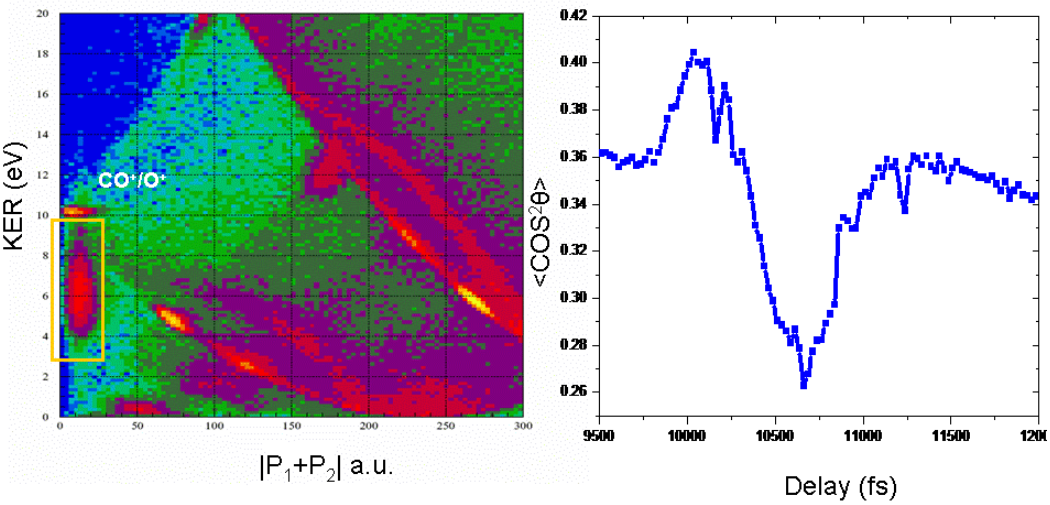

Figure 8.9C: Sum of momenta of CO^+ and O^+ plotted against their kinetic energy release (KER) (left). The quarter revival structure of the CO_2 is found with the condition that the two fragments O^+/O^+ are from the same atom (within the window shown) (right). Pump intensity (I_o) = $8x10^{13}$ W/cm^2 and probe intentsity (I_o)=$2x10^{15}$ W/cm^2

Figure 8.10C shows the polar plots of the angular distribution of O^+ in the plane of polarization for alignment and anti-alignment. Furthermore, these plots were made under the condition that all the fragments were taken from the window of the coincidence spectrum, i.e. both fragments O^+ and CO^+ were produced from the same molecules as shown in Figure 8.9C. The red arrow indicates the direction of polarization of the aligning pulse (molecular alignment axis). It is clearly observed that the angular distribution peaks along the polarization vector for the aligned molecules, but it peaks perpendicular for the anti-aligned.

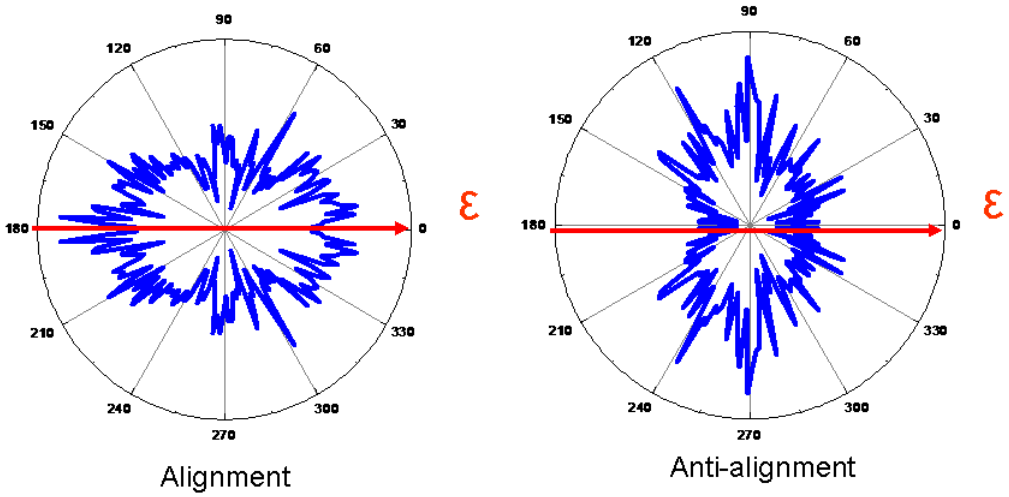

Figure 8.10C: Polar plots of the angular distribution of CO^+ / O^+ channel for alignment and anti-alignment cases.